

# Development of a 3-D Defocusing Liquid Crystal Particle Thermometry and Velocimetry (3DDLCPTV) System

David Robert Schmitt

A thesis  
submitted in partial fulfillment of the  
requirements for the degree of

Master of Science in Aeronautics and Astronautics

University of Washington

2007

Program Authorized to Offer Degree:  
Department of Aeronautics and Astronautics

Report Documentation Page				Form Approved OMB No. 0704-0188	
Public reporting burden for the collection of information is estimated to average 1 hour per response, including the time for reviewing instructions, searching existing data sources, gathering and maintaining the data needed, and completing and reviewing the collection of information. Send comments regarding this burden estimate or any other aspect of this collection of information, including suggestions for reducing this burden, to Washington Headquarters Services, Directorate for Information Operations and Reports, 1215 Jefferson Davis Highway, Suite 1204, Arlington VA 22202-4302. Respondents should be aware that notwithstanding any other provision of law, no person shall be subject to a penalty for failing to comply with a collection of information if it does not display a currently valid OMB control number.					
1. REPORT DATE <b>01 MAY 2007</b>		2. REPORT TYPE <b>N/A</b>		3. DATES COVERED <b>-</b>	
4. TITLE AND SUBTITLE <b>Development of a 3-D Defocusing Liquid Crystal Particle Thermometry and Velocimetry (3DDLCPTV) System</b>				5a. CONTRACT NUMBER	
				5b. GRANT NUMBER	
				5c. PROGRAM ELEMENT NUMBER	
6. AUTHOR(S)				5d. PROJECT NUMBER	
				5e. TASK NUMBER	
				5f. WORK UNIT NUMBER	
7. PERFORMING ORGANIZATION NAME(S) AND ADDRESS(ES) <b>University of Washington</b>				8. PERFORMING ORGANIZATION REPORT NUMBER	
9. SPONSORING/MONITORING AGENCY NAME(S) AND ADDRESS(ES) <b>The Department of the Air Force AFIT/ENEL WPAFB, OH 45433</b>				10. SPONSOR/MONITOR'S ACRONYM(S)	
				11. SPONSOR/MONITOR'S REPORT NUMBER(S) <b>CI07-0047</b>	
12. DISTRIBUTION/AVAILABILITY STATEMENT <b>Approved for public release, distribution unlimited</b>					
13. SUPPLEMENTARY NOTES <b>The original document contains color images.</b>					
14. ABSTRACT					
15. SUBJECT TERMS					
16. SECURITY CLASSIFICATION OF:			17. LIMITATION OF ABSTRACT <b>UU</b>	18. NUMBER OF PAGES <b>143</b>	19a. NAME OF RESPONSIBLE PERSON
a. REPORT <b>unclassified</b>	b. ABSTRACT <b>unclassified</b>	c. THIS PAGE <b>unclassified</b>			

"The views expressed in this article are those of the author and do not reflect the official policy or position of the United States Air Force, Department of Defense, or the U.S. Government."

University of Washington  
Graduate School

This is to certify that I have examined this copy of a master's thesis by

David Robert Schmitt

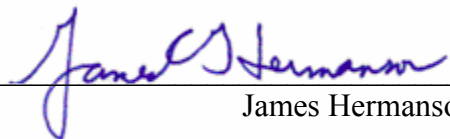
and have found that it is complete and satisfactory in all respects,  
and that any and all revisions required by the final  
examining committee have been made.

Committee Members:



\_\_\_\_\_

Dana Dabiri



\_\_\_\_\_

James Hermanson

Date: 12 Mar 07

In presenting this thesis in partial fulfillment of the requirements for a master's degree at the University of Washington, I agree that the Library shall make its copies freely available for inspection. I further agree that extensive copying of this thesis is allowable only for scholarly purposes, consistent with the "fair use" as prescribed in the U.S. Copyright Law. Any other reproduction for any purposes or by any means shall not be allowed without my written permission.

Signature 

Date 14 Mar 07

## TABLE OF CONTENTS

	Page
List of Figures .....	iii
List of Symbols .....	v
List of Tables .....	vii
1.0 Introduction .....	1
2.0 Background and Previous Work .....	3
2.1 Velocimetry .....	3
2.1.1 Defocusing DPIV .....	5
2.1.2 Initial Geometric Analysis .....	8
2.1.3 3-D DDPIV System Design .....	11
2.1.4 Three Dimensional DDPIV Geometric Analysis .....	17
2.1.5 Velocimetry Error Analysis .....	25
2.2 Thermometry .....	27
2.2.1 Liquid Crystal Categorization .....	28
2.2.2 Optical Properties of Liquid Crystals .....	33
2.2.3 Liquid Crystal Hysteresis .....	34
2.2.4 Liquid Crystal Calibration .....	35
2.2.5 Illumination Source .....	40
2.2.6 Temperature Calibration .....	41
2.3 3-D DLCTV .....	49
3.0 Results – Design and Calibration .....	50
3.1 Camera Design .....	50
3.1.1 Translation Stage Selection .....	55
3.1.2 CCD Selection .....	56
3.1.3 Lens Selection .....	57
3.1.4 Pinhole Design and Testing .....	60
3.1.5 Color Camera Design .....	63
3.1.6 Optical Isolation Tube Design .....	71
3.2 Water Filled Prism Design .....	72
3.3 Camera Redesign .....	77
3.4 Flashlamp Selection .....	79
3.4.1 Linear In-House Lamp – Design and Testing .....	79
3.4.2 Perkin Elmer Parabolic Lamp - Testing .....	81
3.4.3 Cooke Lamp – Testing and Reflector Design .....	85
3.5 Vortex Generator .....	93
3.6 Image Processing .....	94
3.7 Optical Calibration .....	95
3.7.1 Laser Calibration Attempt .....	95
3.7.2 Target Calibration Method .....	101
3.8 Experimental Arrangement .....	111
4.0 Conclusion .....	113
Works Cited .....	115
References .....	118

Appendix A: Camera Spreadsheets .....	122
Appendix B: Water-Filled Prism Optical Derivation .....	127

## LIST OF FIGURES

Figure Number	Page
1. Defocusing concept for a large aperture .....	5
2. Defocusing concept with decreased aperture size .....	6
3. Off-axis aperture setup for defocused imaging.....	7
4. Two-aperture defocused imaging .....	7
5. 2-D defocusing geometric model.....	8
6. 3-Pinhole DDPIV mask arrangement .....	12
7. Schematic of 3-CCD, 3-dimensional DDPIV camera system .....	14
8. Application of 2-D equations to a full 3-D imaging system.....	15
9. Comparison of on-axis and off-axis pinhole placement .....	16
10. Field of view and domain of interest of 3-CCD DDPIV .....	18
11. Volume of interest as viewed from CCD plane for full 3-D system .....	18
12. X-Z projection of the full 3-D DDPIV system .....	19
13. Y-Z projection of the full 3-D DDPIV system .....	19
14. Projection of a particle at $Z_{min}$ without shift term.....	23
15. Projection of a particle at $Z_{min}$ including shift term.....	24
16. Arrangement of liquid crystal molecules in the smectic phase.....	29
17. Arrangement of liquid crystal molecules in the nematic phase .....	30
18. Helix formation in cholesteric liquid crystals.....	31
19. Helical long axis rotation of chiral nematic liquid crystals .....	32
20. Sample hue-temperature calibration curve .....	37
21. Color diagrams for different hue.....	39
22. Hue fields of two constant temperature images using different lighting angles.....	42
23. Calculated temperature fields of constant temperature surfaces.....	43
24. Pixel arrangement used for conditional averaging.....	45
25. Hue-temperature calibration curves for 2-D slices at 3 separate z locations .....	47
26. Design of 3-D DDLCTV Camera System .....	54
27. Partial camera assembly displaying Illunis XMV-11000 CCDs .....	57
28. Lens Characteristics .....	59
29. Rear view of lens holder assembly .....	60
30. Cross-Sectional drawing of spacer with aperture and aperture seat .....	61
31. Pinhole testing images .....	63
32. Transmittance properties of color camera filters .....	64
33. Color camera assembly design.....	66
34. Overlay of the three "color" CCDs prior to image correction .....	68
35. Overlay of the three "color" CCDs after image correction.....	70
36. Particles images showing the effect of a large viewing angle .....	73
37. Water-filled prism design for 3DDLCTV camera.....	74
38. Application and ray tracing for a single off-axis CCD using a water-filled prism.....	75
39. Target images from the bottom CCD with and without a water-filled-prism.....	77
40. Custom elliptical reflector.....	81
41. Perkin Elmer FX-4400 Parabolic lamp.....	82



42. Images of the LC's full color range .....	84
43. SensiFLASH 250 lamp with initial optical setup .....	86
44. 2-D Ray tracing analysis using a) the initial optical setup b) the spherical reflector .	88
45. SensiFLASH 250 with new optical configuration .....	89
46. Elliptical reflector .....	92
47. Vortex generator .....	94
48. Initial laser alignment setup .....	96
49. 4 x 4 square laser grid .....	98
50. Image of laser grid as seen on CCD.....	99
51. Laser grid showing defocused dot splitting .....	100
52. Distortion target grid pattern.....	102
53. Distortion target mounting method .....	103
54. Lens holder focus calibration curve.....	105
55. Overlay of center, top left, and bottom CCDs after individual calibration.....	109
56. Overlay of center, top left, and bottom CCDs after final alignment check .....	110
57. Overlay of defocused images showing image triplets .....	111
58. Experimental setup for 3DDLCPTV camera system.....	112

## LIST OF SYMBOLS

$\phi_l$	Illumination incidence angle of liquid crystal particles
$\phi_s$	Illumination scatter angle of liquid crystal particles
$\gamma$	Radial distance from the optical axis to each lens
$\gamma'$	Radial distance from the optical axis to each of the black and white CCDs
$\lambda$	Reflected wavelength of liquid crystal particles
$\tau_g$	Index of refraction of glass
$\tau_w$	Index of refraction of water
$\zeta$	Distance from an image equilateral triangle's center to any vertex
$a_{pb}$	Side-length of the back of the volume of interest
$a_{pf}$	Side-length of the front of the volume of interest
$a_z$	Depth of the volume of interest
$b$	Particle image separation
$c$	Side-length of cubic domain in 2-D derivation
$d$	Distance between each lens
$d'$	Distance between each black and white CCD
$d_{cw}$	Distance from the lens plane to the front of the test tank wall
$d_{wd}$	Distance from the back face of the test tank wall to the front of the volume of interest
$F$	F-number of the lenses
$f$	Focal length of the lenses
$h$	CCD width
$h_1$	1 <sup>st</sup> Hue definition
$h_2$	2 <sup>nd</sup> Hue definition
$h_3$	3 <sup>rd</sup> Hue definition
$h_v$	CCD Height
$K$	Camera gain
$l$	Distance from the lens plane to the sensor plane
$L$	Apparent distance from the lens plane to the focal plane
$L_t$	True distance from the lens plane to the focal plane (accounts for the index of refraction of the experimental setup)
$M$	Camera magnification
$\bar{n}$	Average index of refraction of liquid crystal particles
$p$	Liquid crystal pitch
$t_w$	Thickness of test section wall
$X$	X-coordinate of a particle in space
$x_0$	X-coordinate of the center of an image equilateral triangle in the CCD coordinate system
$x_b$	X-coordinate of the bottom vertex of an image equilateral triangle in the CCD coordinate system
$x_{TL}$	X-coordinate of the top left vertex of an image equilateral triangle in the CCD coordinate system

$x_{TR}$	X-coordinate of the top right vertex of an image equilateral triangle in the CCD coordinate system
$Y$	Y-coordinate of a particle in space
$y_0$	Y-coordinate of the center of an image equilateral triangle in the CCD coordinate system
$y_B$	Y-coordinate of the bottom vertex of an image equilateral triangle in the CCD coordinate system
$y_{TL}$	Y-coordinate of the top left vertex of an image equilateral triangle in the CCD coordinate system
$y_{TR}$	Y-coordinate of the top right vertex of an image equilateral triangle in the CCD coordinate system
$Z$	Z-coordinate of a particle in space
$Z_a$	Apparent distance from the lens plane to the front of the volume of interest
$Z_{min}$	Apparent distance from the lens plane to the start of the observable domain
$Z_t$	True distance from the lens plane to the front of the volume of interest (accounts for the index of refraction of the experimental setup)
$Z_{tmin}$	True distance from the lens plane to the start of the observable domain (accounts for the index of refraction of the experimental setup)

## LIST OF TABLES

Table Number	Page
1. 3-D DLCTV Camera system geometric properties .....	52
2. Overlay deviations and error for red and blue images .....	71
3. Re-designed 3-D DLCTV camera system geometric properties .....	78

## **ACKNOWLEDGEMENTS**

I would like to express my sincere thanks to the members of the Department of Aeronautics and Astronautics and everyone who has aided me in this project. First and foremost among them are my advisor Dr. Dana Dabiri and project partner Greg Rixon for their tireless support, guidance, and knowledge. To Dan Lotz, Dennis Peterson, Robert Gordon, Dzung Tran, Ted Ellis, Peter Hirtle, and Bob Mathews; this effort could never have happened without your generous help and assistance. Finally, to my friends and family, your love and support have meant the world to me and have made this thesis possible.

## 1.0 Introduction

One of the most intriguing and perplexing problems in fluid mechanics today, as it was 50 years ago, is that of turbulence. The behavior of a fluid in turbulent regions around an object consists of chaotic flow phenomena made of unsteady vortices on many scales that can critically affect the ability of that object to pass through the fluid. Indeed, turbulent convective heat and mass transfer is one of the frequently encountered problems at all levels of applied engineering. While countless research efforts are devoted to understanding turbulent phenomena, this chaotic motion which also consists of random fluctuations in temperature, velocity, pressure, and fluid properties as well as advanced mixing (among other things), has yet to be solved analytically. As a result, understanding this flow requires the use of numerical methods. While turbulent behavior can be resolved through Direct Numerical Simulation (DNS) of the Navier-Stokes Equations, this method is extremely computationally intensive and cannot be practically implemented with today's computing power in flows with Reynolds numbers above approximately  $10^4$  or  $10^5$ . As a result, other methods must be used that can approximate turbulent behavior with flow modeling.

Large Eddy Simulation (LES) is one of these methods. LES utilizes the different scales of turbulent behavior by dividing the large and small eddies of the flow field. Large eddies are then solved directly, while the more complex behavior at smaller scales is modeled using a sub-grid scale (SGS) model. This hybrid method, while less accurate than DNS, provides a higher level of accuracy than pure simulation or the solving of the

Reynolds Averaged Navier-Stokes equations (RANS), and is thus preferable for experiments that contain a higher sensitivity to turbulent effects.

However, as with any modeling method, the performance of LES is only as good as the SGS model that is used to resolve small-scale motion. As a result, validation of the SGS model is required using either DNS or experimental data. The computational difficulty in obtaining DNS data for complex geometries pushes validation towards the experimental side. However, experimental validation has been limited for the most part to partial data sets, as most experimental methods, such as the use of hot-wires and PIV (described below), provide single point or planar data (Meneveau and Katz 2000). Thus, the goal of this research is the creation of an experimental flow measurement system that is capable of providing both temperature and true three-dimensional velocity data in a three-dimensional region of the flow. This system will utilize a combination of Defocusing Digital Particle Image Velocimetry (DDPIV) and liquid crystal thermometry to find the velocity and temperature fields, respectively. As such, this effort will describe the theory behind and previous work accomplished in these two areas, followed by the design and development of the 3DDLCPTV camera system itself.

## 2.0 Background and Previous Work

### 2.1 Velocimetry

Particle Image Velocimetry (PIV) has been a widely accepted flow visualization technique for many years due in part to its ability to collect accurate, quantitative flow data using non-intrusive methods. PIV is in essence a very simple idea. First, a flow is seeded with small, reflective tracer particles. These particles must be chosen in size and type based on the flow and medium into which they are placed such that they can accurately resolve as small a flow phenomena as desired for the particular experiment. Two pictures of the seeded flow are then taken with a known time separation,  $\Delta t$ . By comparing the two pictures using a cross-correlation analysis, the movements of individual particles over that known time interval can be ascertained and velocity calculated (Adrian 1996).

Initial efforts at PIV were accomplished using photographs. However, recent advances in digital imaging have given rise to Digital PIV (DPIV). These methods use charge coupled device (CCD) cameras along with digital data acquisition and processing systems to create digital images that can be manipulated and analyzed to an extent previously impossible with analog methods (Willert and Gharib 1991, Westerweel 1993)

While digital processing has advanced the accuracy and ease with which PIV can be used, most DPIV experiments only produce results in two dimensions. These methods typically use a laser sheet to illuminate a plane of the flow normal to the camera, thus capturing a 2-D slice of potentially 3-D phenomena. The clear limitations of using 2-D PIV have given rise to the recent development of 3-D methods. Murai et. al. (1980) and



Virant and Dracos (1997) used 3-D digital particle tracking velocimetry (3DDPTV) to observe flows in 3-D. This technique uses at least three CCD cameras to track individual particles through a flow field, thereby obtaining velocity data. However, this method requires arduous calibration of the cameras, and is sensitive to particle identification problems.

Another true three-dimensional method, used by Zhang et. al. (1997) is holographic PIV (HPIV) where holographic pictures are taken and then digitally analyzed. Three planar velocity fields are then used to reconstruct the full 3-D velocity field. While this technique does provide significant resolution of the flow being studied, like 3DDPTV it also requires a very sensitive optical calibration in order to produce accurate results. In addition, image processing for this technique can require an extremely large amount of computing power, sometimes taking days to process a single hologram.

In contrast to the previous two methods, defocusing digital PIV (DDPIV) has the capability of creating 3-D velocity fields without the limitations described above. This method uses defocused blurring of particles to ascertain their distance from the camera plane, and standard DPIV methods to solve for in-plane particle positions. This method, which was first used by Willert and Gharib (1992), shows the most promise out of the 3-D PIV techniques and is the method of choice for this study. As a result, it will be described in greater detail in the following section.

### 2.1.1 Defocusing DPIV

The blurring concept discussed above that gives DDPIV its ability to gather depth information is simple in basic theory, but becomes more complicated in execution. The simple two-dimensional example shown in Figure 1 below is perhaps the best way to explain this method.

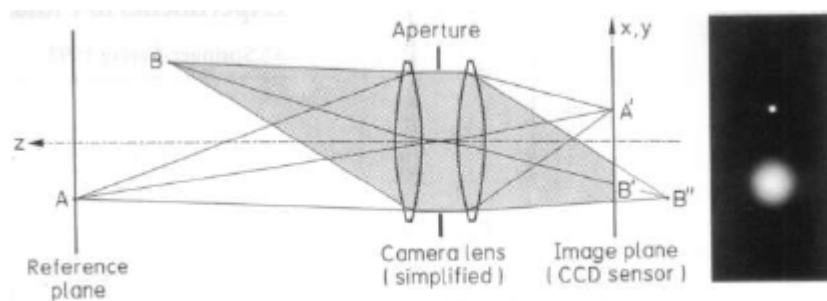


**Figure 1. Defocusing concept for a large aperture (Willert and Gharib 1992)**

Particle A is positioned on the reference plane of the system, which is defined such that a particle placed on this plane will be perfectly focused by the lens onto the CCD at point A'. In contrast, particle B is placed in front of the reference plane of the system which results in it being focused through the lens onto point B'', which sits behind the CCD. The result of this is that the CCD at B' sees a large, blurred particle. This particle's increased size is related to both the size of the aperture and its distance from the reference plane. However, particles that are viewed with large apertures like that shown above, are extremely sensitive to their distance from the reference plane. If a particle is placed only a very small distance away, blurring can occur to such an extent that the image is

unusable. In other words the system has a small depth of field. One way to counter this effect is to decrease the size of the aperture.

Decreasing aperture size has the effect of decreasing the solid angle of the light emitted from a particle at point B that will pass through the lens. As a result, the solid angle of light seen by the CCD is likewise decreased and thus the image of the particle is less blurred and more usable. This is also known as increasing the depth of field, and is illustrated below in Figure 2.

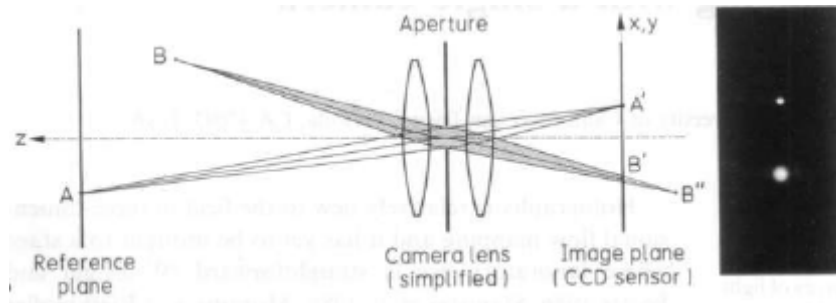


**Figure 2. Defocusing concept with decreased aperture size (Willert and Gharib 1992)**

Movement of the aperture away from the optical axis along the lens plane leads to a proportional shift in the image location on the CCD. This effect is seen in Figure 3 where the projection of a particle at B shifts upward on the CCD by a distance  $b/2$ . Since the particle at A is located on the reference plane, its location is unaffected by the change in aperture location. Unsurprisingly, the shift of a particle on the CCD is also related to the particle's distance from the reference plane (Willert and Gharib 1992).

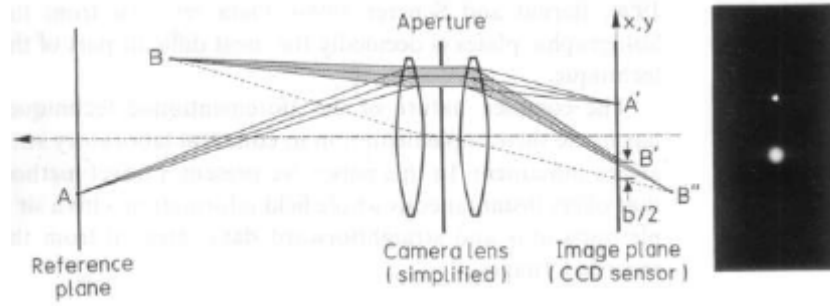


**Figure 3. Off-axis aperture setup for defocused imaging (Willert and Gharib 1992)**

This shift can thus be utilized to measure a particle's  $z$ -position by the addition of a second aperture mirrored about the  $z$ -axis. This setup is shown in Figure 4.

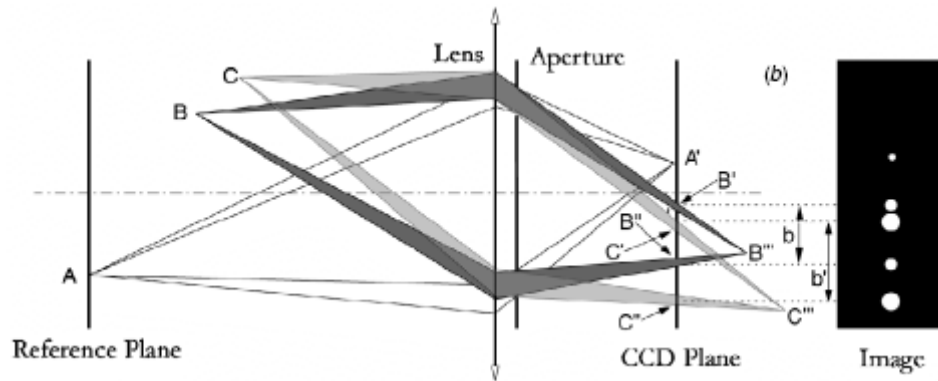
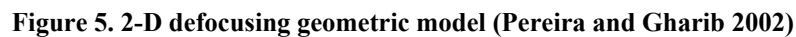


**Figure 4. Two-aperture defocused imaging (Kajitani and Dabiri 2005)**

In this configuration, particle A still focuses onto the same location,  $A'$ , on the CCD. However, rays from particle B now pass through both apertures and focus to  $B''$ , which as before is behind the CCD plane. This results in the imaging of two separate blurred spots  $B'$  and  $B''$  on the CCD, which are separated by a distance  $b$ . Likewise a particle placed at point C, which is closer to the CCD plane than B, will focus through the apertures and image two blurred spots at  $C'$  and  $C''$  separated by a distance  $b'$ . By

As a result of using multiple apertures, finding the position of a particle in space becomes an exercise in ray tracing and geometry. By using 2-D geometric analysis like that in Figure 5, Willert and Gharib (1992), Pereira, Gharib, Dabiri and Modarress (2000), and Pereira and Gharib (2002) derived the equations for the position of a particle in space based on the parameters shown in the diagram. These equations are listed below.



$$Y = \frac{-y_0 Z(L-f)}{fL} = \frac{-y_0 Z}{ML} \quad \text{where} \quad y_0 = \frac{y' + y''}{2} \quad (1)$$

$$X = \frac{-x_0 Z(L-f)}{fL} = \frac{-x_0 Z}{ML} \quad \text{where} \quad x_0 = \frac{x' + x''}{2} \quad (2)$$

$$Z = \frac{1}{\frac{1}{L} + Kb} \quad (3)$$

And

$$K = \frac{1}{MLd} \quad b = \frac{Md}{Z}(L-Z) \quad M = \frac{f}{L-f} \quad (4)$$

In this model,  $M$  is the optical magnification factor,  $d$  is the distance between the apertures,  $h$  is the sensor height,  $L$  is the distance from the aperture or lens plane to the reference plane,  $l$  is the distance from the sensor to the lens plane,  $b$  is the separation of the two blurred images on the sensor,  $Z_{min}$  is the distance from the lens plane to the beginning of the imaging volume,  $f$  is the focal length of the lens, and  $(X,Y,Z)$  are the coordinates of a particle in the imaging volume. It should also be noted, however, that to successfully image a particle in the imaging volume onto the sensor, the optical magnification factor defined above must agree with the geometric magnification factor (based on only  $h$ ,  $c$ ,  $d$ , and  $l$ ) defined below.

$$M = \frac{h(L-c)}{c(L+d)} \quad (5)$$

The observable domain of this system was defined by Pereira and Gharib (2002), and is shown in grey in the figure above. Although shown as a 2-D area, this region is in fact a volume that extends from the reference plane, to a point termed  $Z_{min}$  where the

fields of view from each aperture first overlap. Any particle present in this volume will be imaged onto the CCD, with the greatest value of  $b$  occurring for a particle positioned at  $Z_{min}$ . For any system defined in this manner  $Z_{min}$  can be calculated using the equation below (Pereira and Gharib 2002).

$$Z_{min} = \frac{d(L - c)}{c + d} \quad (6)$$

With this model it is important to quantify how well the system will be able to resolve  $Z$ -position using this blurred concept. This resolution physically represents how much the blurred image separation,  $b$ , changes with a corresponding change in a particle's  $Z$ -position. Mathematically this is depicted by Equation 7 below as the partial derivative of  $b$  with respect to  $Z$ .

$$\frac{\partial b}{\partial Z} = -\frac{1}{KZ^2} \quad (7)$$

In this definition,  $K$  represents the system's gain factor. Optimal performance will occur when the above function achieves a maximum. Due to the behavior of this function, there exists no specific maximum point, but the region between the lens plane and the reference plane exhibits higher values than does the region behind the reference plane. It is for this reason that the former region is typically used in DDPIV, as shown in the geometric analysis.

It should also be noted that the blurred image separation,  $b$ , is independent of the X and Y position of the particle, thus providing a variable that can determine Z-position and resolution independent of position along the image plane. Likewise, the size of the aperture in this arrangement has no effect on any of the above equations, and is only the controlling variable for the system's depth of field. This allows it to be adjusted independent of any other system parameters. Finally,  $b$  is a positive value only for a particle placed between the lens and reference planes. If a particle exists behind the reference plane,  $b$  will become negative and thus the separation of the image will reverse position. This can lead to incorrect identification of particle position for a 2-aperture setup as laid out above, due to the possible non-uniqueness of any blurred separation on the CCD.

### **2.1.3 3-D DDPIV System Design**

As pointed out by Willert and Gharib (1992), uniquely determining each particle in a densely seeded flow field for a 2-aperture system becomes increasingly difficult, even if particles only exist inside the imaging volume. When the non-uniqueness of particles located behind the imaging volume discussed above is also taken into account, determining particle location using 2-apertures proves extremely difficult. To counter this problem, a third aperture was added to the system, with the three pinholes (apertures) placed at the vertices of an equilateral triangle. This arrangement creates a corresponding triangular arrangement (triplet) of particle images on the CCD, where individual particles can be readily distinguished. The issue of the inversion of  $b$  for particles located behind the reference plane is also fixed by this arrangement, as any particle thus located will



image onto the CCD as an upside-down triangle and can be discarded. This aperture arrangement is shown in Figure 6.

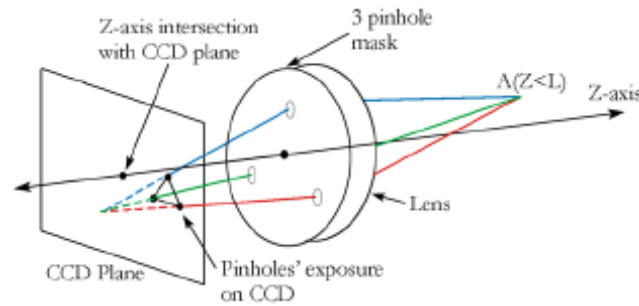


**Figure 6. 3-Pinhole DDPIV mask arrangement (Kajitani and Dabiri 2005)**

This three-pinhole arrangement was used successfully by Willert and Gharib (1992), Pereira and Gharib (2002), and Pereira, Gharib, Dabiri, and Modarress (2000) to perform 3-D DDPIV experiments. However, in each of these cases a 3-pinhole mask was applied to a single lens and particle images focused onto a single CCD, which created several problems. First, the aperture separation helps define the size of the potential imaging volume. As a result, increasing the size of the imaging volume to study different flow phenomena necessitates a corresponding increase in lens size, which can require very expensive custom made lenses. Second, using a 3-pinhole mask to project onto a single CCD triply exposes the sensor. The result is that for densely seeded flow fields, triplets on the image become indistinguishable from one another due to heavy overlapping of the blurred images.

To counter this problem, Kajitani and Dabiri (2005) proposed a redesign of the camera system, where three separate imaging systems are used to create a single image.

This was accomplished by using three separate lenses placed in a triangular pattern about the optical axis and equidistant from it, with three separate CCD sensors placed in a correspondingly larger triangular pattern about the optical axis behind them. While this arrangement makes the placement of each individual part of the camera system critical to the overall performance and accuracy, it fixes the aforementioned problems inherent in a 3-pinhole mask system. Using 3 CCDs, each part of the triangular pattern is singularly exposed onto one CCD, thus eliminating the problem of image overcrowding in densely seeded flow fields. In addition, by using 3 separate lenses, lens size is no longer dependant on imaging volume size, making cheaper, off the shelf optics viable.

Although seemingly different, this system functions in essentially the same way as the three-pinhole mask design discussed earlier. A schematic of the new design is displayed in Figure 7. Images from this system's three CCDs can be added together in post processing to create one image with the identifiable triangular triplets imaged from each particle. This can be seen on the schematic, with a particle placed at point A imaging to the upper-left side of CCD 1, the upper-right side of CCD 2, and the bottom of CCD 3 thus forming the triangular pattern on the superimposed image shown in the bottom right.

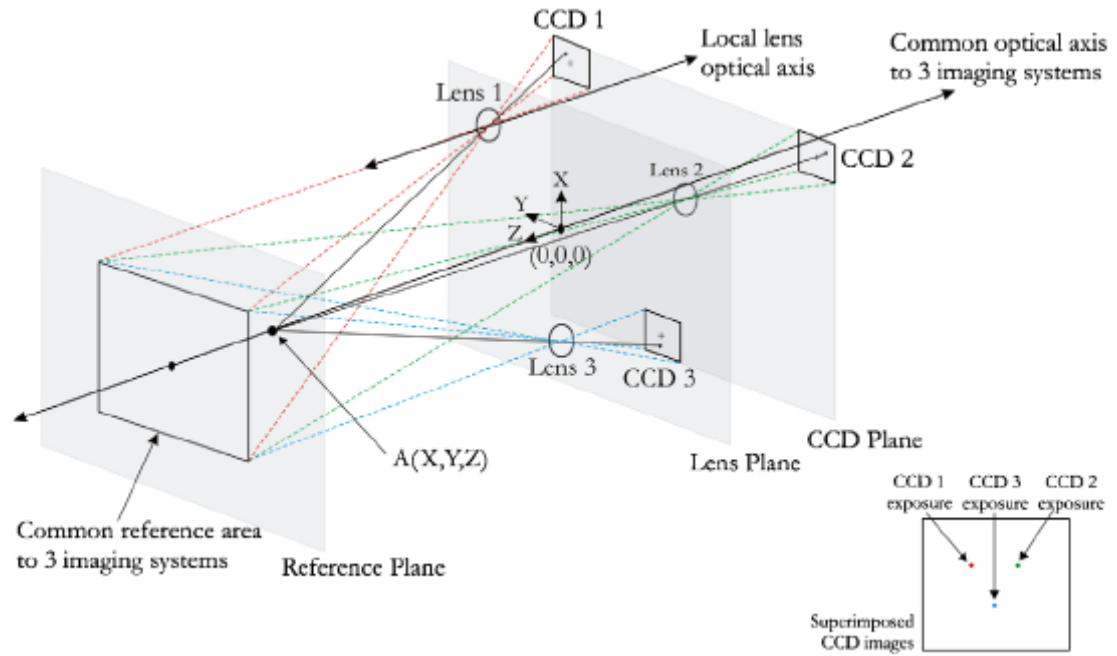
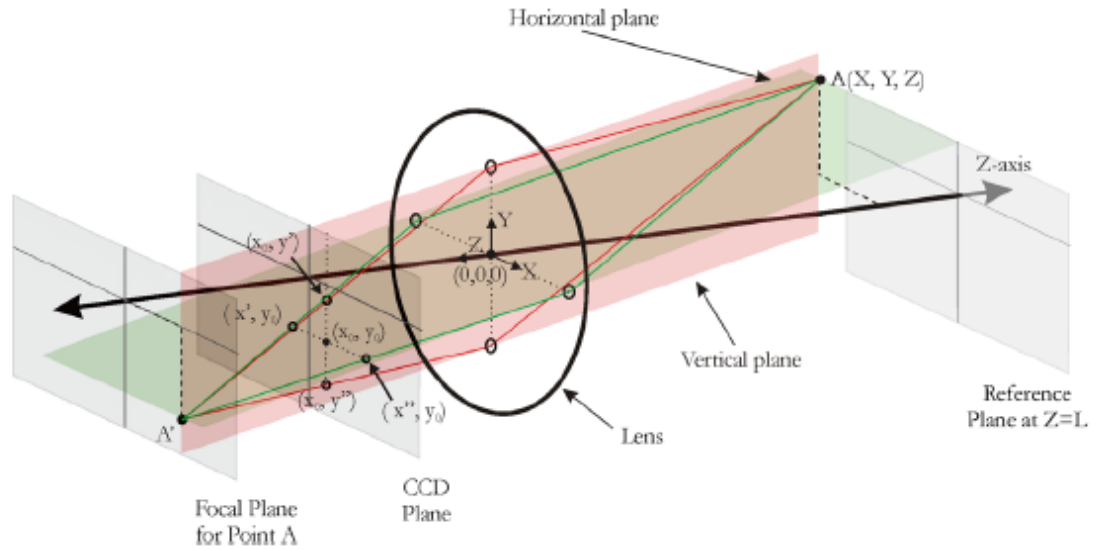


Figure 7. Schematic of 3-CCD, 3-dimensional DDPIV camera system (Kajitani and Dabiri 2005)

Although this system functions off of the same theory as that which was used to create the DDPIV equations displayed earlier, one must be careful before directly applying these equations to this system. The two-dimensional derivation of Willert & Gharib (1992) required that the apertures be in-plane and equidistant from the Z-axis. Functionally, this requires that pinholes must be placed either along the X or Y-axis for the equations previously derived to be valid. This fact is shown in Figure 8, where a 4 pinhole aperture is used to image the particle, with two pinholes placed equidistant from the optical axis along the X-axis, and two correspondingly placed along the Y-axis.



**Figure 8. Application of 2-D equations to a full 3-D imaging system (Kajitani and Dabiri 2005)**

Using the 2-D equations, the two projected images from the X-axis pinholes can be used to solve for the particles X and Z position, while the images resulting from the Y-axis pinholes can be used to find the particle's Y and Z position. In this manner the previous derivation can correctly calculate particle position in space for aperture arrangements that exist only along the X and Y-axes.

However, the same is not true for cases where the pinholes are placed off of both the optical, and the X and Y-axes. This fact is shown in Figure 9 where two pinholes are again placed on-axis for comparison, denoted by open circles, and three pinholes are placed off-axis and are denoted by open stars. The projected blurry images from the rightmost four apertures are shown on the CCD plane, with dots representing the on-axis apertures and stars representing the two rightmost off-axis apertures.

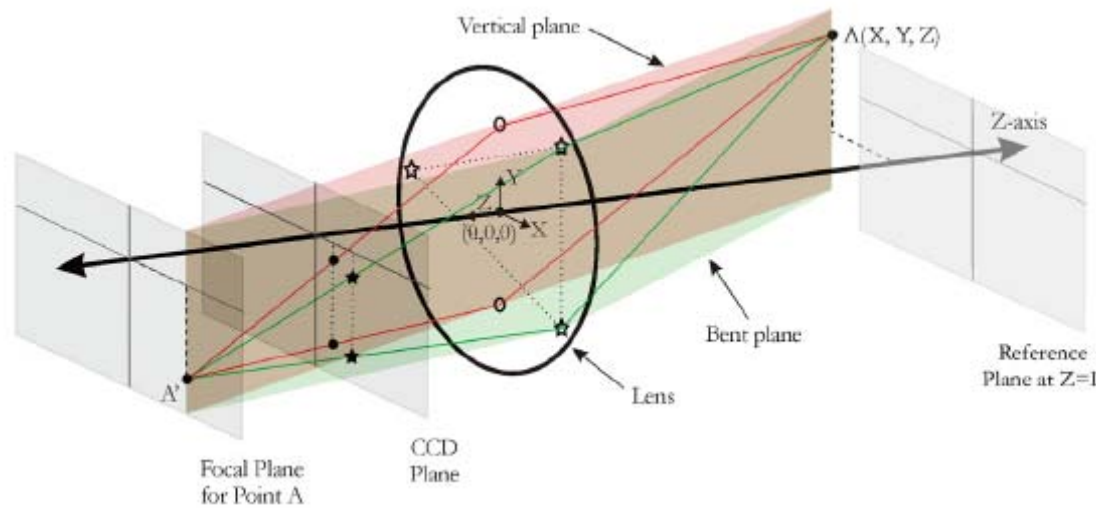


**Figure 9. Comparison of on-axis and off-axis pinhole placement (Kajitani and Dabiri 2005)**

In this arrangement the two rightmost off-axis pinholes are arranged vertically and at the same height and distance from one another as the on-axis pinholes. Thus the only difference between the two pairs is their X-position. If the two-dimensional equations were applied to these two aperture pairs, it seems logical that the particle at A would have the same position for both the on and off-axis pinholes. However, the projected images shown in the figure prove this result in error. The displacement between the dots and stars on the CCD appears to be the same for both aperture arrangements. This would result in finding the correct Z-position of the particle using either set of apertures. However, the off-axis images (closed stars) are noticeably further displaced from the Y-axis in the X-direction than the on-axis images (dots). This difference would result in finding two different X-locations for the two different aperture setups. As a result, the two-dimensional equations can clearly not be applied to the off-axis apertures. As a

result of this fact, a new geometric analysis is necessary to fully describe the 3-CCD DDPIV system (Kajitani and Dabiri 2005).

#### **2.1.4 Three Dimensional DDPIV Geometric Analysis**

In the previous analysis, the region of interest was shown as a 2-D slice of a 3-D volume; however the shape of this volume was dependant upon the placement of the system's apertures. Now that a specific aperture setup has been defined, the domain of interest and the observable domain take on a definite shape, shown in Figure 10a below. The observable domain is formed by the intersection of the three cones of view of the apertures and is colored light green. The point at which all three cones first meet is termed  $Z_{min}$ , as before, and represents the closest a particle may be positioned and still be imaged onto all three CCDs. The domain of interest is thus defined by a tetrahedron inscribed within the observable domain extending from  $Z_{min}$  to just in front of the reference plane, as particles imaged at the reference plane will render the defocusing concept invalid. A 2-D slice of the region of interest can be seen in Figure 10b. By defining the domain of interest thusly, the geometric properties of the system can be fully and uniquely described with equations. However, it should be noted that particles that exist outside of the domain of interest but still within the observable domain will still be imaged onto all three CCDs.

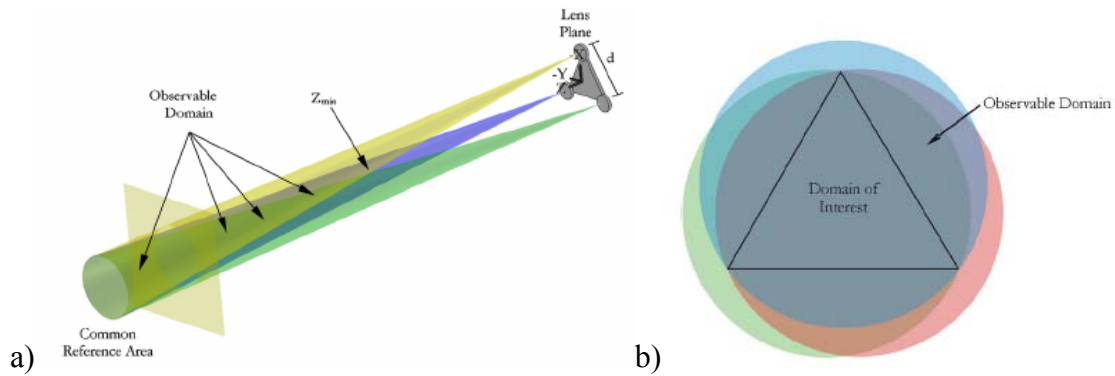


**Figure 10. a) Field of view of 3-CCD DDPIV system b) inscribed domain of interest in the observable domain of all three cameras (Kajitani and Dabiri 2005)**

For the purposes of experimentation only, a sliced section of finite thickness taken from the domain of interest must be imaged. This section is termed the “volume of interest” and is defined uniquely by the side length of the front equilateral triangle,  $a_{pf}$ , the side length of the back equilateral triangle,  $a_{pb}$ , and the thickness of the volume,  $a_z$ . Figure 11 depicts a frontal view of this volume. It should be noted that  $a_{pb}$  must be larger than  $a_{pf}$  in the system defined above due to the expanding nature of the observable domain.

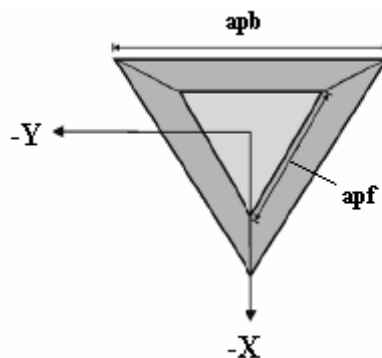


**Figure 11. Volume of interest as viewed from CCD plane for full 3-D system (Kajitani and Dabiri 2005)**

To accomplish a full 3-dimensional geometric analysis, Kajitani and Dabiri (2005) used projections of the 3-D system onto both the X-Z and Y-Z planes, shown in Figures 12 and 13 respectively.

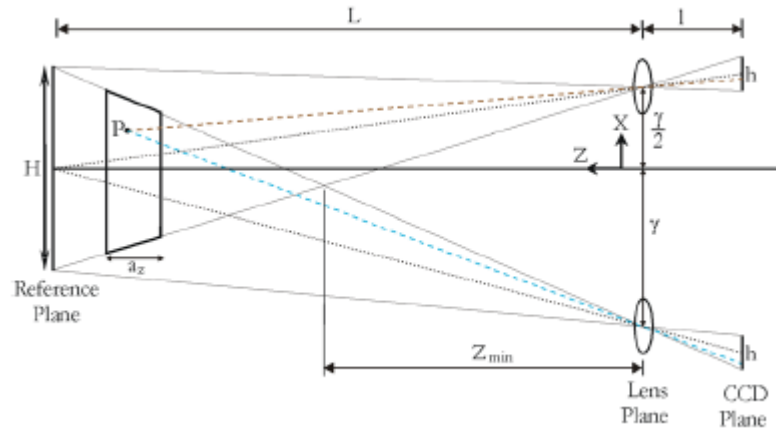


**Figure 12. X-Z projection of the full 3-D DDPIV system (Kajitani and Dabiri 2005)**

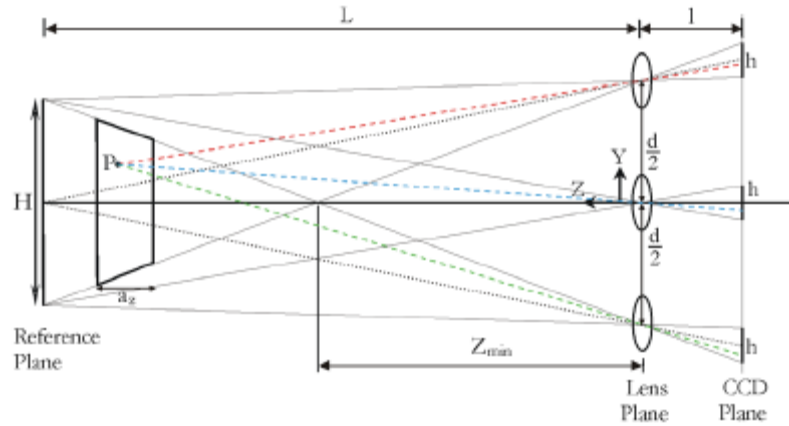


**Figure 13. Y-Z projection of the full 3-D DDPIV system (Kajitani and Dabiri 2005)**

By using the above figures to generate equations for the positions of the particle images on the CCD ( $x_{TR}$ ,  $x_{TL}$ ,  $x_B$ ,  $y_{TR}$ ,  $y_{TL}$ , and  $y_B$ ) as a function of the particle's position in space,



among other things, they were then able to solve for the particle's position (X,Y,Z) as a function of the generated image. These equations are listed below.

$$x_B = -\frac{M}{Z}[XL + \gamma(L - Z)] + \frac{2 - \sqrt{3}}{2\sqrt{3}}h \quad (8)$$

$$x_{TR} = x_{TL} = -\frac{M}{2Z}[2LX - \gamma(L - Z)] + \frac{2 - \sqrt{3}}{2\sqrt{3}}h \quad (9)$$

$$y_B = -\frac{Yl}{Z} \quad (10)$$

$$y_{TR} = \frac{M}{2Z}[-d(L - Z) - 2LY] \quad (11)$$

$$y_{TL} = \frac{M}{2Z}[d(L - Z) - 2LY] \quad (12)$$

And

$$X = \frac{-x_0 Z}{ML}, \quad \text{where} \quad x_0 = \frac{x_{TR} + x_{TL} + x_B}{3} \quad (13)$$

$$Y = \frac{-y_0 Z}{ML}, \quad \text{where} \quad y_0 = \frac{y_{TR} + y_{TL} + y_B}{3} \quad (14)$$

$$Z = \left(\frac{1}{L} + \frac{\xi}{M\gamma L}\right)^{-1} \quad (15)$$

Where

$$K = \frac{1}{MLd} \quad b = \frac{1}{K} \left| \frac{1}{Z} - \frac{1}{L} \right| \quad M = \frac{f}{L - f} = \frac{hZ_{\min}}{d(L - Z_{\min})} \quad (16)$$

In this model  $x_{tr}$ ,  $x_{tl}$ , and  $x_b$  represent the x-coordinates of the upper-right, upper-left, and bottom locations respectively, of the blurred particles in the combined image. Likewise,  $y_{tr}$ ,  $y_{tl}$ , and  $y_b$  represent the y-coordinates. As is obvious in the above equations, rather than referencing the planar separation between the pinholes and the corresponding images,  $d$  and  $b$  respectively in the 2-D derivation, using radial variables becomes much easier in the 3-dimensional system. As a result,  $\gamma$  is defined as the radial distance from the optical axis to each of the three lenses, and  $\xi$  is the radial distance from the center of any image triplet to one of its vertices. These definitions can be used due to the fact that all three lenses are positioned equidistant from the optical axis. The radial lens distance can be related to the lens separation in Equation 17 below, using simple geometry.

$$\gamma = \frac{d}{\sqrt{3}} \quad (17)$$

Additionally,  $(x_0, y_0)$  now marks the position on the sensor of the center of the triangular triplet. The definition of the system gain,  $K$ , remains unchanged, as does the optical magnification. However, due to changing system geometry, the geometric magnification is a function of  $Z_{min}$  rather than  $c$ , as it was under the old definition.

Perhaps the most noticeable change to the three dimensional model is the change to the input parameters of the system. Previously, parameters such as  $d$ ,  $L$ , and  $c$  defined the system performance. With this new model, the entire system can be defined based

almost entirely on the size of the volume of interest and the optical characteristics of the lens. This can be seen in the definition for  $Z_{min}$  under the new system,

$$Z_{min} = Z_a + a_z \left( \frac{a_{pf}}{a_{pf} - a_{pb}} \right) \quad (18)$$

where  $Z_a$  is the distance from the lens plane to the front face of the imaging volume, and in the definition of the lens separation,  $d$ .

$$d = \frac{Z_a(a_{pb} - a_{pf}) - a_z a_{pf}}{a_z} \quad (19)$$

Thus, the geometric arrangement of the imaging system, including lenses and CCDs, becomes solely dependant upon the size and location of the imaging volume for a given choice of lens. In this arrangement the lens focal length,  $f$ , helps solve for both the magnification factor and the distance between the lens and reference planes. Practically speaking, this aspect of the three dimensional model allows a camera system to be built based on only the size of the phenomena being studied, thereby easing the design process. It should also be noted that the general equation for system sensitivity does not change with the 3-D model, and thus Equation 7 can still be used.

One final note should be made about the full three dimensional derivation. In order to provide maximum resolution, the above equations were derived such that a particle at  $Z_{min}$  images the largest possible triangular pattern onto the CCD. In practice,

this requires the side length of the imaged equilateral triangle to be equal to the sensor size,  $h$ . However, this presents a problem, as the top and bottom vertices are not located at equal distances from the radial center of the triangle. Thus, when the center of the triplet resulting from a particle at  $Z_{min}$  is imaged onto the center of the CCD, the entire triplet is not located on the CCD, which results in a decrease of the volume that can be imaged. This effect is shown in Figure 14. It should be noted that the triangular image formed by a particle at  $Z_{min}$  represents the area of the CCD upon which every particle inside the volume of interest will be imaged.

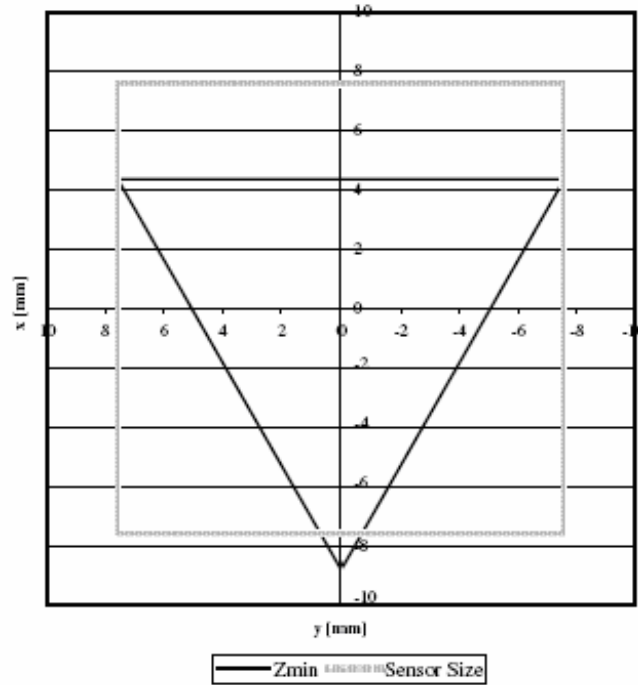


**Figure 14. Projection of a particle at  $Z_{min}$  without shift term (Kajitani and Dabiri 2005)**

To counter this, Kajitani and Dabiri (2005) proposed a downward shift of all three CCDs that comprise the 3-D system. This shift can be made independent of the system

magnification, and depends only on CCD size. It is reflected mathematically by introducing a shift term into the equations for the image coordinates. This is the final term in Equations 8-9, and will change only with sensor size. By utilizing this shift, it is possible to increase the percentage of the volume of interest that can successfully be imaged. Kajitani and Dabiri (2005), using the shift, were able to create a system that could image the entire volume of interest, including a particle located at  $Z_{min}$  as shown by Figure 15.

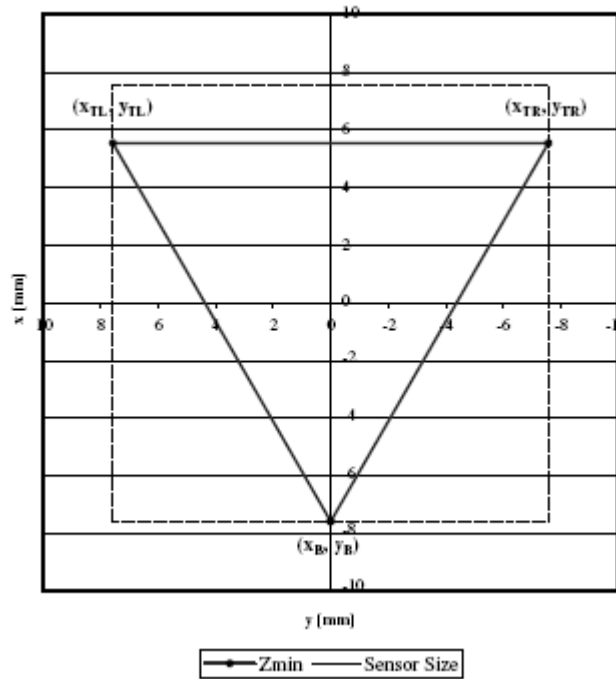


**Figure 15. Projection of a particle at  $Z_{min}$  including shift term (Kajitani and Dabiri 2005)**

While this shift will not allow the entire volume of interest to be imaged for every choice of CCD size, it is a valid method for increasing the imaging area, and must be considered when designing a full 3-D DDPIV system.

### 2.1.5 Velocimetry Error Analysis

The expressions for a particle's position on the CCDs in term of its spatial position can be differentiated to yield a particle's displacement on the sensor as a function of its spatial displacement. These equations are shown below

$$\begin{aligned}
 dx_B &= \frac{\partial x_b}{\partial X} dX + \frac{\partial x_b}{\partial Y} dY + \frac{\partial x_b}{\partial Z} dZ \\
 dy_B &= \frac{\partial y_b}{\partial X} dX + \frac{\partial y_b}{\partial Y} dY + \frac{\partial y_b}{\partial Z} dZ \\
 &\vdots \\
 &\vdots \\
 dx_{TL} &= \frac{\partial x_{TL}}{\partial X} dX + \frac{\partial x_{TL}}{\partial Y} dY + \frac{\partial x_{TL}}{\partial Z} dZ
 \end{aligned} \tag{20}$$

Where  $dx_b$ ,  $dy_b$ , etc are displacements in local image coordinates on the CCD and  $dX$ ,  $dY$ , and  $dZ$  are the displacements in space. Evaluation of the partial derivatives in space, and inversion of the ensuing matrix yields

$$\begin{Bmatrix} dX \\ dY \\ dZ \end{Bmatrix} = \begin{bmatrix} A & 0 & B & C & B & -C \\ -2D & E & D & F & D & G \\ -2H & 0 & H & -I & H & I \end{bmatrix} \begin{Bmatrix} dx_B \\ dy_B \\ dx_{TR} \\ dy_{TR} \\ dx_{TL} \\ dy_{TL} \end{Bmatrix} \tag{21}$$

where

$$\begin{aligned}
A &= \frac{-Z}{3LM} \left( \frac{d^2 + 3\gamma(\gamma - 2X)}{d^2 + 3\gamma^2} \right), & F &= \frac{-Z}{3LM} \left( \frac{d^2 + 3\gamma(\gamma + 3Y)}{d^2 + 3\gamma^2} \right), \\
B &= \frac{-Z}{3LM} \left( \frac{d^2 + 3\gamma(\gamma + 3X)}{d^2 + 3\gamma^2} \right), & G &= \frac{-Z}{3LM} \left( \frac{d^2 + 3\gamma(\gamma - \frac{Yd}{\gamma})}{d^2 + 3\gamma^2} \right), \\
C &= \frac{-ZXd}{LM} \left( \frac{1}{d^2 + 3\gamma^2} \right), & H &= \frac{-Z^2\gamma}{LM} \left( \frac{1}{d^2 + 3\gamma^2} \right), \\
D &= \frac{-ZY\gamma}{LM} \left( \frac{1}{d^2 + 3\gamma^2} \right), & I &= \frac{Z^2d}{LM} \left( \frac{1}{d^2 + 3\gamma^2} \right), \\
E &= \frac{-Z}{3LM} & & 
\end{aligned} \tag{22}$$

where uncertainties of the image plane coordinates ( $dx_B$ ,  $dy_B$ , etc) are assumed to be equal. Applying error analysis to these equations yields the uncertainty in a particle's displacement in space, shown below.

$$\begin{aligned}
\delta(dX) &= \frac{\Delta x}{\sqrt{3}} \frac{|Z|}{ML} \sqrt{1 + \frac{X^2}{\gamma^2}} \\
\delta(dY) &= \frac{\Delta x}{\sqrt{3}} \frac{|Z|}{ML} \sqrt{1 + \frac{Y^2}{\gamma^2}} \\
\delta(dZ) &= \frac{Z^2}{MLd} \Delta x = KZ^2 \Delta x
\end{aligned} \tag{23}$$

In this manner, the uncertainty in spatial coordinates for any particle imaged by the camera system can be roughly calculated (Kajitani and Dabiri 2005). It should be noted that this derivation of uncertainty is only a first cut, reflecting only the contribution of particle identification uncertainty on the CCD to the total uncertainty of a particle in

space. As a result, this analysis assumes perfect positioning of all optical components in the system.

Using the above derivation for a full 3-D DDPIV system, a camera can be constructed which will be able to measure the velocities inside a volume of interest in a flow field. However, the above work only lays the foundation for half of the camera system's proposed capabilities (i.e. velocity measurements). As such, different methods for measuring temperature using liquid crystals must now be examined to augment the DDPIV system. These methods are discussed in the ensuing section.

## **2.2 Thermometry**

The use of liquid crystals as a means of evaluating temperature is an accepted and widely used method for both 2-D surface heat measurements and 2-D fluid temperature measurement. The basis of surface thermometry is the painting of a heat-controlled plate with a thin layer of liquid crystals, which will predictably and consistently change in color with changing temperature. Particle Image Thermometry (PIT) in a fluid functions in much the same way. It uses temperature sensitive liquid crystals to seed a volume of interest in a fluid. However the name PIT is misleading, as it implies any type of particle can be used to seed the flow, which is incorrect, as liquid crystal particles must be used as tracers. As a result, this type of thermometry will be referred to as Liquid Crystal Particle Thermometry (LCPT). While these methods differ in their execution, the behavior of the liquid crystals is constant and thus both can provide valuable insight into the operation and calibration of any thermometry system. In either method, the region of interest must be illuminated by white light, which then reflects off the crystals towards a recording



device. Due to the properties of the crystals, which will be discussed in further detail later, different wavelengths and thus different colors will be reflected towards the camera as temperature varies in the region of interest. These various temperature-dependant colors can then be used to calibrate the measurement system to provide quantitative temperature measurements at any point in the region. The following sections will further describe liquid crystals themselves and the thermometry process.

### **2.2.1 Liquid Crystal Categorization**

The term “liquid crystal” seems to derive its name from two seemingly contradictory terms: liquid and crystal. A liquid is typically thought of as a loose, unorganized collection of molecules wherein its lack of structure causes it to fill whatever container it is placed in. Conversely, a crystal is thought of as a solid that displays a rigid molecular structure. Despite this contradiction there exists an intermediate phase between solid and liquid wherein the molecules lose their positional order, thus moving freely and behaving like a liquid, but maintain their orientation order, a key property of crystals. These substances are called liquid crystals (LCs), as they possess the useful optical properties of crystals while moving freely and filling their container like a liquid. They were first discovered as a state of matter in 1889 through the observation of a cholesterol derivative that appeared liquid in form but double refracted light, a property of crystals (Dabiri 2007, Hay and Hollingsworth 1996).

There are generally three different classifications of liquid crystals: lyotropic, polymeric, and thermotropic. Lyotropic liquid crystals, such as soap, exhibit liquid crystalline behavior when mixed with a solvent, where the density of lyotropic liquid

crystal molecules in the solvent determines its phase. Conversely, polymeric liquid crystals refer to polymers that display liquid crystal behavior when in a liquid state. While these two forms are useful in certain applications, liquid crystal thermometry requires that temperature determine the phase of the liquid crystal. This necessitates the use of thermotropic liquid crystals (TLCs), which are comprised of rod or disk shaped molecules whose phase, and thus reflected wavelength, vary directly with temperature. Since this phase variance with temperature provides the basis for liquid crystal thermometry, the different phases must be further explained.

The phases of liquid crystals can generally be classified as smectic, nematic, or cholesteric, with several subgroups therein. In the smectic phase the rod-shaped liquid crystal molecules are organized into layers with the long axis of each molecule pointing perpendicular to the plane of the layer. Inside of each layer the molecules can either have a definite structure of rows and columns as seen in Figure 16a, or be randomly distributed as in Figure 16b.

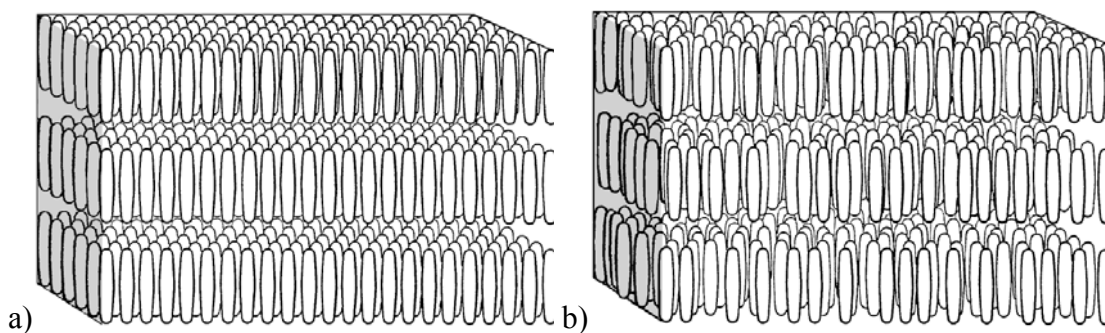


**Figure 16. Arrangement of liquid crystal molecules in the smectic phase. a) subgroup of smectic phase whose molecules are organized within each layer b) further subgroup whose layers' molecules are randomly placed (Ferguson 1964, Mitchell 2004)**

The second phase of liquid crystals is called the nematic phase. In this phase the rod-shaped molecules are not arranged in layers, but their long axes are still parallel to each other. This arrangement is depicted in Figure 17 below.

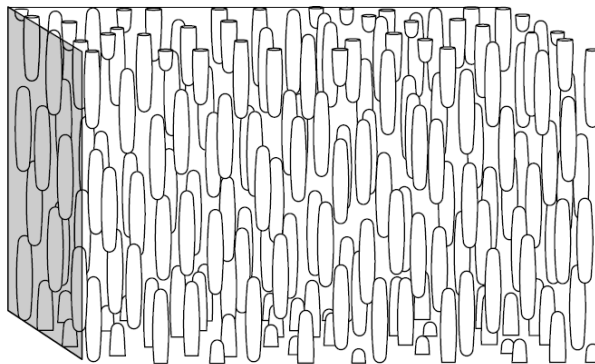


**Figure 17. Arrangement of liquid crystal molecules in the nematic phase (Fergason 1964, Mitchell 2004)**

The third and final liquid crystal phase is the cholesteric phase, so called because it was first observed in cholesterol esters. This phase contains some of the characteristics of both the smectic and nematic phases. Like the smectic phase, the molecules self arrange into layers and, like the nematic phase, arrange themselves randomly within those layers. However, the molecules of this phase differ in one regard. Rather than the standard rod shaped molecule seen above, these molecules are flat, with several molecular asymmetries that cause the molecule's long axis to rotate slightly between each layer. This rotation carves out approximately 15 arc minutes per layer, resulting in the creation of a helical structure defined by each layer's long axis (Oseen 1933). This behavior is well illustrated in Figure 18 below.

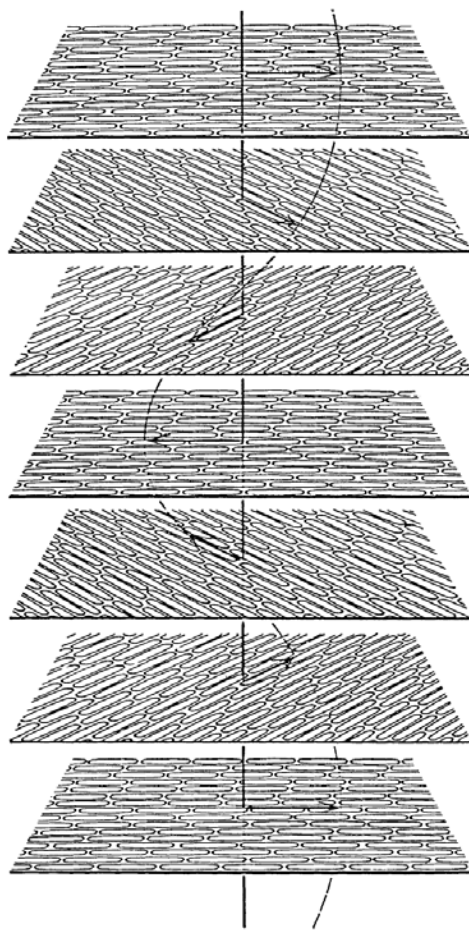


**Figure 18. Helix formation in cholesteric liquid crystals (Fergason 1964, Mitchell 2004)**

While cholesteric liquid crystals (CLCs) occur naturally, they are limited in many regards. They do not provide a large range of color play (i.e. CLCs change color from red to blue over a very small temperature range), are not perfectly stable, and their purity depends on their source. However, liquid crystals can now be synthesized to exhibit the same behavior as CLCs but with improved stability, color play, and purity. Due to their structure these liquid crystals are termed chiral nematic.

In the nematic phase, liquid crystal molecules can either be chiral or achiral. Achiral molecules, like those shown above, are symmetric about their long axes.

Conversely, chiral molecules are asymmetric about their long axes, just like cholesterol esters. As a result, intermolecular forces cause the long axis of each molecule to similarly tilt and thus become rotated relative to its neighboring particles. The result is the direction of the long axes of the molecules again forming a helix. This behavior is displayed in Figure 19 where the pitch ( $p$ ) is defined as the distance necessary for the helix to rotate 360 degrees.

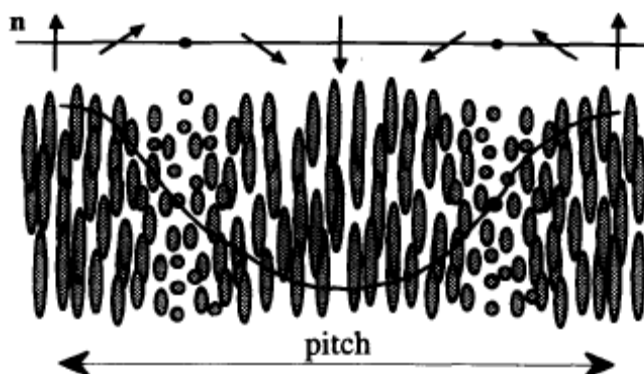


**Figure 19. Helical long axis rotation of chiral nematic liquid crystals (Hay and Hollingsworth 1996)**

In any phase, liquid crystals can be fragile and very susceptible to damage from various different sources including contamination, extreme temperatures and UV light. As a result, liquid crystals are typically protected by encapsulation in a polymer coating. This encapsulation is typically very thin and results in microencapsulated liquid crystal spheres on the order of 20 microns (Hay and Hollingsworth 1996). Despite the protection afforded by this method, liquid crystals must still be handled with care to obtain accurate results, as the liquid crystal's color response can slowly change after prolonged periods of exposure to the environment, and be permanently altered if the

temperature is elevated far above the crystals upper temperature design/clearing point (Wiberg and Lior 2004).

### **2.2.2 Optical Properties of Liquid Crystals**

In order to understand the colors produced by liquid crystal thermometry, it is essential to understand the optical properties of the liquid crystals themselves that facilitate this method. When light hits the liquid crystalline structure it is circularly polarized into left and right-handed components. The component of the light that has the same polarization as that of the liquid crystal completely transmits, as there is no change in its refractive index. However, the other component of the light will see a change in refractive index whenever the oppositely rotating helixes interfere with one another. This occurs at  $p/2$  intervals and results in reflection of that wavelength of light. In this manner the liquid crystals function as band pass filters. However, because only one of the two polarized components of light is reflected, liquid crystals will only reflect a maximum of 50% of the total light (McDonnell 1987), with typical reflection values being closer to 20% (Anderson and Baughn 2005).

As a result of this behavior, the pitch of the liquid crystal itself affects the wavelength of the reflected light. However, pitch is inversely related to temperature. Thus, as the liquid crystal is cooled from its isotropic stage where it transmits all light and is therefore colorless, it begins to selectively reflect light. At the highest active temperature the crystals will reflect violet. As the crystals are further cooled the pitch continues to increase and the reflected light will transition to blue, then green, then yellow, and finally to red. At this point further cooling drives the pitch of the crystals to

infinity, or in other words the molecules do not rotate and the liquid crystal has entered the colorless smectic phase.

A temperature varying pitch is what gives liquid crystals the ability to be utilized as a thermographic tool. However, as shown by Ferguson (1966), the reflected wavelength is also a function of scatter and incidence angle according to Equation 24,

$$\lambda = 2\bar{n}p \left[ \cos \frac{1}{2} \left\{ \sin^{-1} \left( \frac{1}{\bar{n}} \sin \phi_i \right) + \sin^{-1} \left( \frac{1}{\bar{n}} \sin \phi_s \right) \right\} \right] \quad (24)$$

where  $p$  is the pitch of the liquid crystal,  $\phi_i$  the incidence angle, and  $\phi_s$  the scatter angle. In practice, this behavior means that not only will color be a function of the temperature of the crystals, but also of the angles at which they are illuminated and viewed (Dabiri 2007).

### 2.2.3 Liquid Crystal Hysteresis

Liquid crystals were first widely used in thermometry experiments in part because they were thought of as an accurate, reversible, and repeatable temperature measurement method. However, recent research such as that accomplished by Sabatino et al. (2000) and Anderson and Baughn (2004) has shown that in fact this is not the case. Anderson and Baughn tested five different samples of TLCs, all with varying color ranges and differing clearing points. In all cases, non-trivial hysteresis was present when the TLCs were cooled rather than heated. This hysteresis was somewhat controllable. For cases where the temperature at which cooling begins is near the upper limit of the crystal's

color play, the observed hysteresis is small. However, if the maximum temperature is increased above that of the upper clearing point, hysteresis occurs and increases in magnitude as the maximum temperature is increased. They found that this hysteresis can be attributed to both a decrease in the reflectivity of the TLCs and a shift in the temperatures at which the peak R, G, and B values occur. For those TLCs that possess a large color play range (approximately 20 degrees), the magnitude of the hysteresis was significant, at approximately 20% of the total color play.

Anderson and Baughn theorized that this hysteresis was the result of permanent damage to the liquid crystals. They suspected that this damage resulted from high temperature exposure, i.e. above that of the TLC's upper clearing point. Sabatino et al. (2000) came to this same conclusion as they observed hysteresis totaling 13% of the crystal's color play when the upper clearing point of their crystals was exceeded. Wiberg and Lior (2004) also suspected that permanent damage of the TLC from aging at temperatures near the upper clearing point could be a source of hysteresis. However, the hysteresis described above can be significantly minimized by ensuring that testing and calibration procedures occur during heating of the TLCs from below the lower clearing point, and keeping the TLCs at or below the temperature of the upper clearing point. In addition, when not actively being heated, the crystals should be kept at a temperature near the lower end of the color play range to prevent damage due to high temperature aging.

#### **2.2.4 Liquid Crystal Calibration**

When used in any thermometry application, a color-temperature calibration must be performed on the associated liquid crystals in order to provide a quantifiable



relationship between liquid crystal color and the recorded temperature. Without an accurate, reliable calibration, quantitative digital processing of the temperatures in the image is impossible. Indeed, the accuracy of LC thermometry is influenced to a large extent by the quality of the temperature calibration. However, this aspect of the process creates a problem. Color is typically thought of as a linear combination of the three primary colors: red, green, and blue. This standard view has problematic implications when applied to liquid crystal thermometry, as there exist many different combinations of R, G, and B on a standard 8-bit 0-255 scale, which correspond to differing intensities of the same color. In essence a calibration curve using only R, G, and B would have to be able to account for all possible shades of color as well as possible intensities. In practice this variation introduced intensity based error into the method (Smith et al. 2001)

It is for this reason that a transformation from RGB color space into HSI (Hue, Saturation, and Intensity) color space has been almost universally applied in LC thermometry experiments. In this space, intensity, I, represents the brightness of the light, saturation, S, represents the purity of the color, and finally hue, H, represents the dominant wavelength of the light. In this space, a pure color will have low intensity or “whiteness,” while nearly white light will have low saturation (Park et al. 2001). Since hue represents the dominant wavelength of the light, it is a natural calibration variable for thermometry as it varies monotonically with color. This factor allows for the generation of smooth hue-temperature calibration curves like that shown in Figure 20 below from Park et al. (2001).

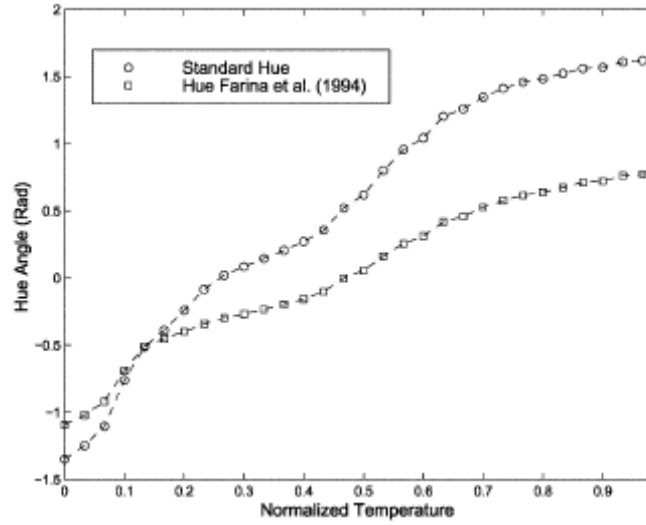


Figure 20. Sample hue-temperature calibration curve (Park et al. 2001)

The definition of hue demands that it be independent from both saturation and intensity. In essence, it must simply be an orthogonal vector to S and I. As a result of this fact, there are many different possible definitions of hue that will prove satisfactory for the purposes of thermometry. Despite this, several standard definitions are typically used. Hay and Hollingsworth (1996) defined and tested three of these definitions for both accuracy and computational time. The first of these definitions utilizes the uniform chromaticity or UVW scale. This scale uses a linear transformation from RGB space to generate the color diagram shown in Figure 21a. All possible colors are represented on this scale and radiate outward from a white light point. In this scale, hue,  $h_1$ , is defined as follows:

$$h_1 = \arctan[(v - v_0)/(u - u_0)] \quad (25)$$

The second definition of hue,  $h_2$ , originates from the formation in color space of a regular triangle with R, G, and B at each of the triangle's vertices and the white light point at its center. This triangle is oriented such that the red, having the longest wavelength, is aligned with the x-axis thereby making hue, defined as positive counterclockwise, a monotonically decreasing function of wavelength. The resulting color diagram is displayed in Figure 21b. Using this arrangement, hue relates to R, G, and B by Equation 26.

$$h_2 = \arctan\left(\frac{\sqrt{3} * (G - B)}{2 * R - G - B}\right) \quad (26)$$

The third and final definition explored by Hay and Hollingsworth was formed through a different linear transformation of R, G, and B values as in  $h_1$ . Using this transformation creates the color diagram shown in Figure 21c, where hue,  $h_3$ , is defined by Equation 27.

$$h_3 = \arctan(z_2 / z_1) \quad (27)$$

While all three of these definitions of hue resulted in monotonically increasing hue-temperature calibration curves,  $h_2$  proved to be the optimum choice. While both  $h_1$  and  $h_2$  produced approximately the same calibration ranges and uncertainties,  $h_2$  takes significantly less computing time, and is thus preferable. Possibly due to the shift of the hue pivot away from the white light point,  $h_3$  produced the smallest range and highest

uncertainties of the three and was thus found to be an undesirable definition. Due to these results,  $h_2$  will be used as the hue definition from this point forward.

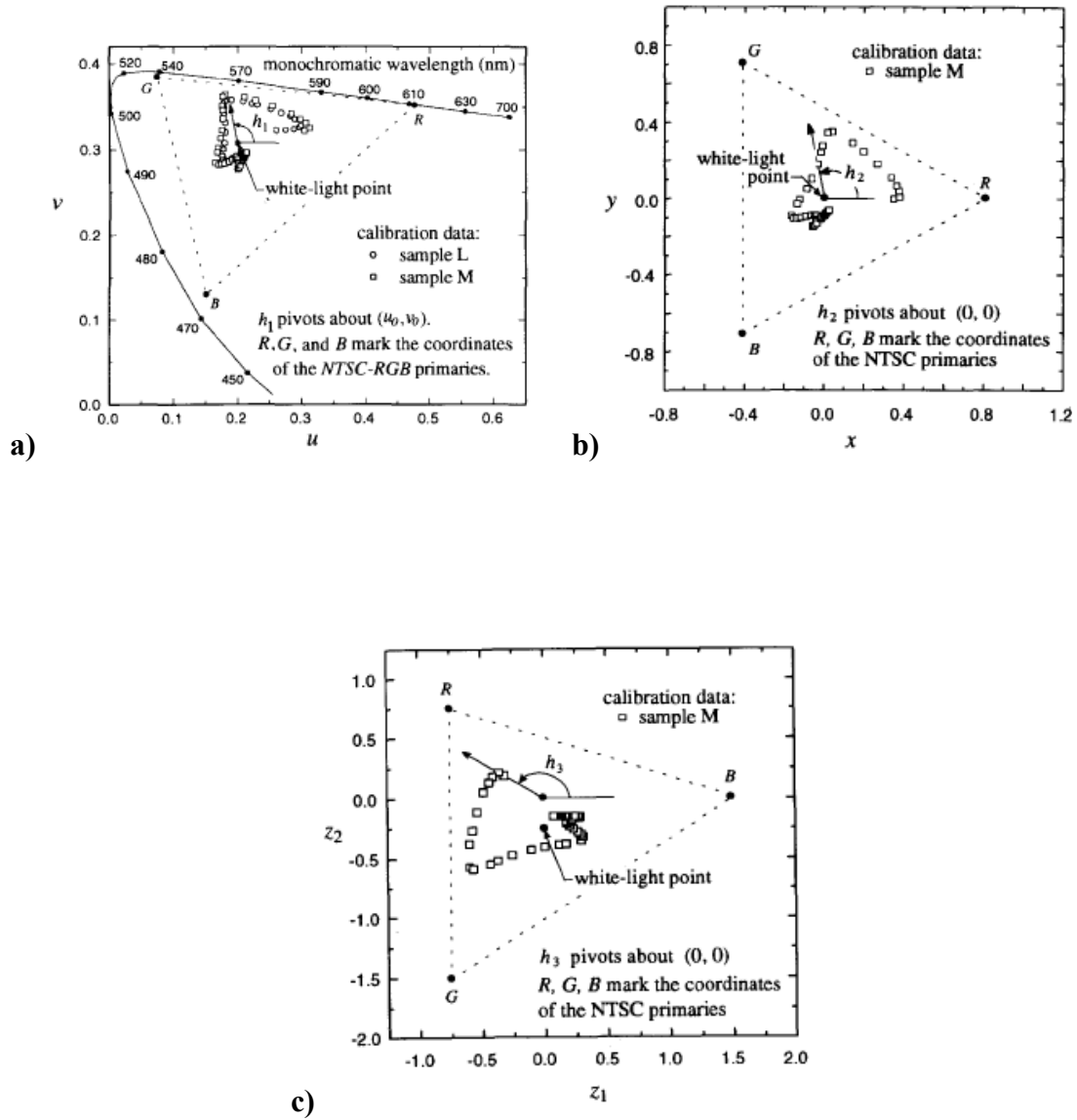


Figure 21. Color diagrams for different hue definitions a)  $h_1$ , b)  $h_2$ , c)  $h_3$  (Hay and Hollingsworth 1996)

### 2.2.5 Illumination Source

Previous work shows LC thermometry experiments to have a strong reliance on both the type and position of illumination used. In general, a full spectrum light source is desirable over other alternatives for LCPT. Experiments by Anderson and Baughn (2005) testing five different illumination sources found that, in general, full spectrum illumination produced lower uncertainties and a larger color range than other “off-white” illumination sources. Since previous testing by Park et al. (2001) on 2-D LCPT experiments displayed a high level of temperature uncertainty, it is essential to use a light source that is as close to full spectrum as possible. This biases LCPT experiments into using sources that have both high-energy outputs and full spectrums, such as short arc pulsed Xenon lamps.

In addition to the type of illumination source, the orientation of the light source is nearly as important. As previously discussed, the reflective properties of LCs vary with both viewing and illumination angle. As such, it is best to orient the light source in such a way that variations resulting from those angles are minimized. For LCPT experiments it has been found that collimated light sources oriented normal to the camera plane can create successful images (Park et al. 2001). This arrangement causes all light rays hitting the LCs to be both parallel to each other and normal to the CCD plane, reducing angular variations, in theory, to those caused only by the size of the imaging area/volume itself. This condition greatly eases the temperature calibration method.

### 2.2.6 Temperature Calibration

Perhaps the most difficult and influential aspect of creating a high accuracy LCPT system is the temperature calibration method. In general, two main techniques have been used on both surface and particle image LC thermometry (Smith et al. 2001). The first of these methods is the “narrow-band” technique. Using this technique LCs with a small temperature range (approximately 1°C) are used to track the path of a single color over time on a constant heat flux surface. This color is usually yellow, as it is displayed over the smallest range of visible wavelengths. While this method requires only one calibration point (i.e. the color yellow), it still necessitates a large number of calibration images, as the event color must be tracked over a series of images. In addition, for small temperature variations the accuracy of this calibration method is limited, which is an undesirable trait for most quantitative experiments.

The second and more widely used method is called the “wide-band” method. In this technique, crystals with a larger color play are utilized to create calibration curves over the full range of colors in the visible spectrum. While this method does necessitate many calibration points, it allows the full color range to be mapped accurately. In addition, given the correct setup the full color range can be mapped in only one picture. Jeschke et al (2000) used a surface with linearly varying temperature to capture the full range of LC reflection in one image. More typically however, this method uses a series of images at a constant temperature to provide full resolution of the color spectrum. Due to its accuracy and ease of implementation, the wide-band method has been used in most LCPT experiments and thus the various aspects of calibrating using this technique must be investigated further (Smith et al. 2001).

Much of the initial development of LC temperature calibration was performed with the goal of analyzing 2-D heat transfer on some kind of surface. While not as complicated as LCPT, these experiments do provide valuable insight into the calibration methods themselves. The first, and for a time most accepted wide-band method was, as described above, to use a series of constant temperature images and create a hue-temperature calibration curve joining these images. However, this method typically used a single reference point inside of each image to define the hue for that corresponding color and applied that reference point to the rest of the image. The major downside is that this method does not account for variations in viewing angle inside the area of interest. These effects were first thought to be negligible, but as images captured by Sabatino et al. (2000) show, there is a radial variation in color, and thus hue, over each constant temperature image. Constant temperature images that display this effect can be seen in Figure 22 below.

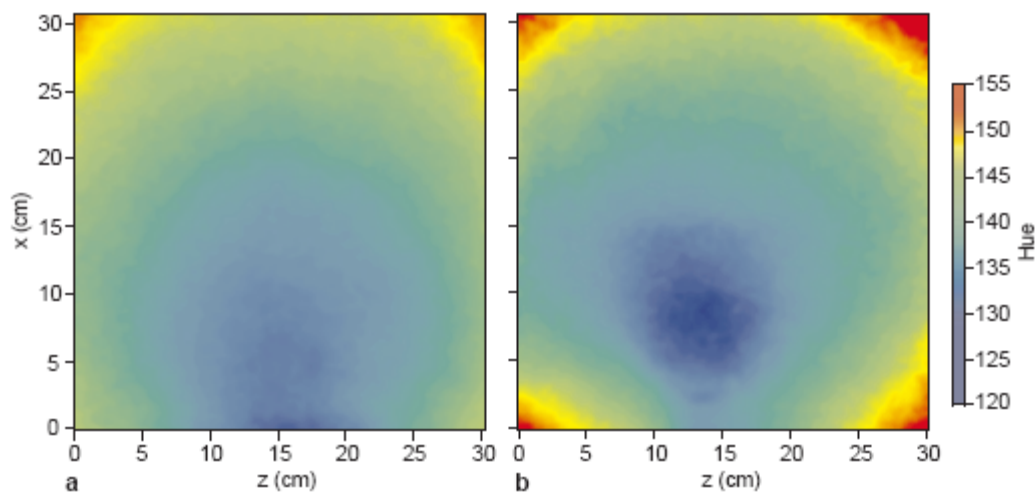


**Figure 22. Hue fields of two constant temperature images using different lighting angles (Sabatino et al. 2000)**

In order to counter this variation, several different methods have been applied. Hollingsworth et al. (1989) applied the first of these by dividing each constant temperature image into 13 different regions, and then creating a local calibration curve for each region. This gave the global result of the calibration accounting for variations due to viewing angle.

Sabatino et al. (2000) took the next step in the evolution of the wide band calibration method by further subdividing each image. Rather than use separate regions in which to define a calibration curve, they established calibration curves for each pixel on their CCD. This method, while very computationally intensive (185,000 calibration curves created), was able to drastically reduce the perceived radial variation in temperature. The result was calibration-based calculated temperatures that were within  $\pm 1\%$  of the actual calibration temperatures. This effect is shown in Figure 23.

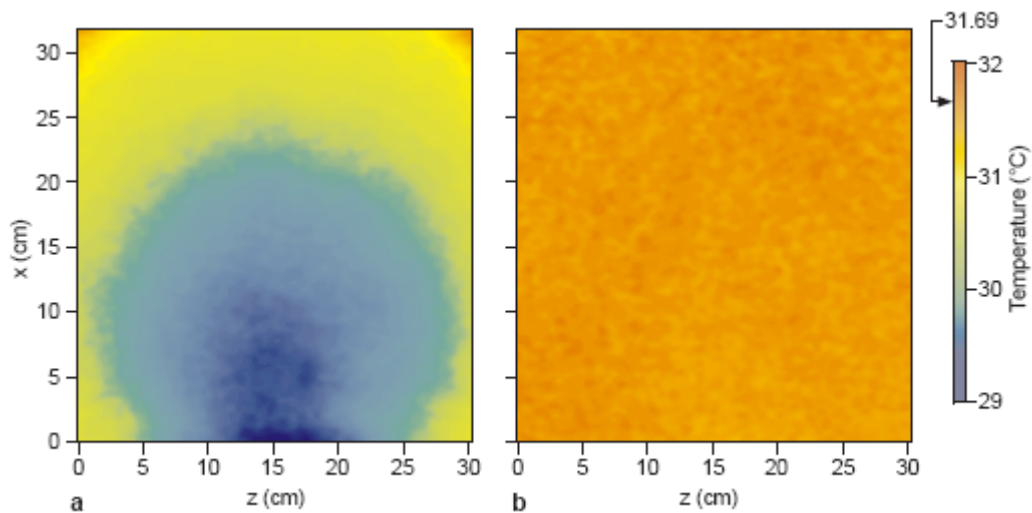


**Figure 23.** Calculated temperature fields of a constant temperature surface using a) single point calibration and b) pixel by pixel calibration (Sabatino et al. 2000)



A somewhat different approach using neural networks has also been applied in recent years to help create a more robust calibration technique. In this method, RGB data from the various constant temperature curves was used as training data for the network. In Grewal et al. (2006), a region of interest 120 x 120 pixels was further divided into 10 x 10 blocks to provide adequate resolution for the network to account for angular hue variations. With training based on RGB data sets from these points, total error was reduced over the single point method by approximately an order of magnitude (1°C to 0.1°C). A similar method to this was also used by Park et al. (2001) to create more accurate calibration curves over the single point technique.

While using a pixel-by-pixel calibration method to reduce error shows promise, this method cannot be directly applied to LCPT. In 2-D surface measurements, the entire area of interest is coated in a layer of LCs. As such, every pixel has the ability to be a calibration point. In LCPT only a small percentage of the total number of pixels actually contain images of LCs. The result is that other methods must also be implemented to successfully calibrate a LCPT system. Park et al. (2001) used a thresholding method to gather the relevant temperature data. First an intensity image was constructed from the R, G, and B images. This image was then used to create a second contrast-enhanced image, which was then thresholded to create a list of particle positions. Those positions were then used on the first image to locate the positions of maximum intensity for each liquid crystal. The pixel at the location of maximum intensity and the surrounding 8 pixels were then conditionally averaged to provide RGB information, as shown in Figure 24. This conditional averaging eliminated pixels with low saturation values, thereby stopping the data from being skewed due to bright spots on the crystals or dust and other

non LC material, which reflect white. This data was then fed into a neural network as discussed previously.

Alternatively, Dabiri and Gharib (1996) took thresholded data and used a combination calibration method, where both local and single calibration methods were combined. In this method, a local calibration curve is first calculated for the center of the image only. Then a global image is taken and the radial hue variations calculated. This variation data is then combined with the local curve to account for spatial variations in hue.

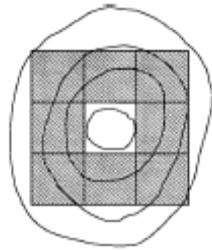


**Figure 24. Pixel arrangement used for conditional averaging (Park et al. 2001)**

All of the methods discussed heretofore have, for the most part, been 2-D methods. While these methods provide key insight into potential 3-D calibration techniques, they fail to resolve temperature calibration in the Z-direction. To this point, no full 3-D temperature calibrations have been successfully accomplished, though several attempts at calibrating in three dimensions have been made by using 2-D scanning. This is a process in which a 2-D white light sheet is moved in the Z-direction such that a series of 2-D images at various Z-positions are taken. The full range of these images can then be combined to give an approximation of a three dimensional calibration. Fujisawa and

Funatani (2000), used this method, where for each 2-D slice of the 3-D volume of interest a spline fitting technique was applied to every calibration point, which were distributed over the entire image. In this manner, spatial hue variations were accounted for. This same calibration was then used for each consecutive 2-D image in order to construct the full 3-D temperature profile. Using this method, they were able to reduce temperature measurement uncertainty to 0.11°C or 4.7% of the temperature range of the crystals. In addition, this spline fitting method proved to be an order of magnitude faster than using neural networks.

However, using a single 2-D calibration curve for the entire 3-D cavity could introduce added error into the system. For that reason, Lutjen et al. (2001) studied this effect and determined that in fact this is not the case. The hue-temperature calibration curves of 2-D slices at 3 separate Z-positions showed strong agreement, as seen in Figure 25. This finding led them to conclude that one 2-D calibration can be applied three-dimensionally. It should be noted that the LCs used by Lutjen begin to reflect red light at approximately 24.25 degrees, which is depicted in the figure below as the smoothly rising section of the calibration curve. Hue values that occur below that temperature are purely base reflections off of the LC's polymer coating prior to the LC's lower clearing point being reached.

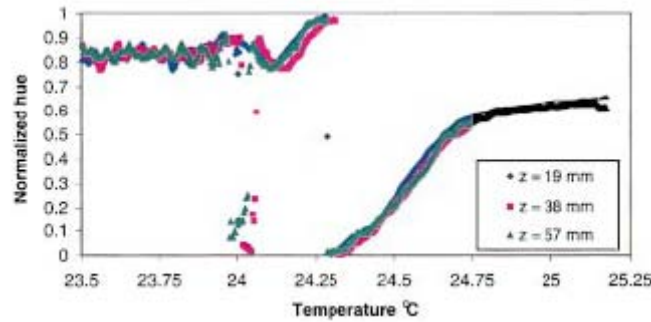


**Figure 25. Hue-temperature calibration curves for 2-D slices at 3 separate z locations (Lutjen et al. 2001)**

Despite these findings, one should be careful before applying these results to full 3-D thermometry (rather than scanning), as the use of a light sheet in 2-D methods eliminates variations in color due to the angle at which the light is emitted from its source. Theoretically, the use of a collimated light source in full 3-D experiments should render the above assumption valid, as all light would again impact the LCs at the same angle. However, no research has been done to confirm this.

Regardless of the calibration method chosen, there are several processes that can help reduce the total uncertainty of the experiment. Perhaps the most important of these processes is performing the calibration “in situ.” As has been previously discussed and shown, the perceived color and thus temperature produced by the LCs has a very strong and sensitive dependence on viewing and lighting angle. As such, even the most careful setup procedures would not be able to maintain the exact same orientations and positions of the camera, lighting system, and volume of interest. Thus, any movements will introduce unnecessary error into a system that is already very sensitive to uncertainty. By performing both the temperature calibration and the actual experiment using exactly the same setup and within the useful stable timeframe of the LCs, this error can be eliminated

entirely. The necessity of an “in situ” calibration has been well documented, and is a staple of virtually every high accuracy LCPT calibration.

Another process that has been theorized to create better images from a LCPT system is a background subtraction method outlined by Farina et al. (1994). This method supposes that some reflection from the micro-encapsulated polymer itself at approximately the spectrum of the illumination source can bias or wash out color images. Therefore in this method an image is taken with the LC outside of their color range such that the only values recorded are that of pure reflection from the polymer itself. These RGB values are then subtracted from any future color images, thus removing any “baseline reflection” of the crystals. While Sabatino et al. (2000) refuted this method’s effectiveness, his cited reason was its failure to remove spatial hue variations in a constant temperature image. Since those variations have been shown to be the cause of changes in viewing angle, the background subtraction method should not be expected to remove them but only to improve the color signal’s purity. As such, it should not be readily discarded as a potential means of improving color images.

Finally, Hay and Hollingsworth (1998) proposed using a dimensionless definition of temperature in order to generate standard hue vs. temperature calibration curves. Using this method they were able to collapse the calibration curves from several different experiments using different lighting conditions and angles as well as different LCs altogether into one curve. The result is the ability to use a single general hue vs. dimensionless temperature calibration curve to quantitatively describe the behavior of many different LCs, or the same LCs, under differing lighting conditions. While many experiments are only created to use a single lighting condition, the volume of light

necessary for full 3-D LCPT could require the use of two separate light sources. In this case, the use of a dimensionless temperature calibration curve could help account for positioning errors of the two light sources relative to one another.

## **2.3 3-D DLCTV**

While both 3-D DDPIV and 3-D scanning LCPT have been accomplished, these efforts have never been combined. In addition, a full 3-D LCPT system itself has never, to this author's knowledge, been successfully created. All of the efforts described above provide key insights into how such a system must be designed, created, aligned, and calibrated. However, as the scope of those efforts falls short of that for a full 3-D system for measuring both temperature and velocity, there are numerous issues and challenges that arise solely as a result of this expanded capability. These challenges, such as the development of a calibration technique or providing sufficient light intensity, are not unexpected, as this system will allow turbulence and other flow phenomena to be studied in ways that were previously impossible. As such, the goal of the remainder of this paper is to discuss the design, creation, calibration, and provide a proof of concept experimental design for a full 3-D DLCTV system.

### **3.0 Results – Design and Calibration**

#### **3.1 Camera Design**

In order to construct a fully three-dimensional DLCTV system, the triangular camera and lens arrangement required to perform DDPIV must be used as a starting point. This arrangement proves convenient when integrating with thermometry, as the triangles formed by the cameras and lenses are centered about the optical axis. LCPT, as described above, requires the use of a preferably on-axis, color CCD to extract temperature data from a TLC seeded flow field. As a result, a color camera can be positioned in plane with the other three CCDs and centered on the optical axis. In this setup, a fourth lens and aperture must also be added at the center of the equilateral triangle formed by the other three to complete the optical system. This arrangement, whose specific geometric properties will be discussed in the following paragraph, allows images from all four CCDs to be superimposed, forming a single composite image wherein particles in space can be readily and uniquely identified by the presence of four blurred spots at the vertices and center of an equilateral triangle. A particle's three-dimensional velocity can then be calculated by correlation analysis of the blurred spots at the vertices of the triangle in two consecutive images, while temperature data is obtained by hue analysis of the center spot. In this manner, a camera designed according to the DDPIV equations with a color camera placed along the optical axis can fully resolve the temperature and velocity of all particles located within the camera's volume of interest.

The first step in the design process of this camera system is to configure the 3-D DDPIV setup. While the thermometry aspect of this research has its own requirements,

other than physical space constraints of the hardware it imposes no requirements on the DDPIV system itself. As a result, it can be easily integrated into the triangular camera setup following initial design. To accomplish this configuration, the equations describing DDPIV (Eqns. 8-19) were first entered into an Excel spreadsheet (See Appendix A). The only required design variables for this system, as discussed previously, are the dimensions and location of the volume of interest and the focal length of the selected lenses, which will be discussed later. The size of the volume of interest was selected in order to adequately resolve the characteristic flow scales of the turbulent flow field behind a backward facing step (the ultimate goal of this camera system), thus providing validation data for LES modeling. It should also be noted that this size is large enough to capture good pictures of a heated vortex ring for use as a proof of concept. So, from the variables  $a_{pf}$ ,  $a_{pb}$ ,  $a_z$ ,  $Z_a$ ,  $t_w$ , and  $f$ , all other necessary geometric properties of the system were calculated using the equations describing this 3-D DDPIV system (Eqns. 8-19). Because there are a range of acceptable sizes for the volume of interest, a local optimization of its size is possible. This optimization was accomplished using in-house software and produced the dimensions that result in the best possible Z-resolution while at the same time minimizing overall volume size to maximize illumination intensity. It should be noted that this optimization also took into account the physical constraints of the camera hardware such as camera size and calibration rod length. These resultant values are listed in Table 1 below.



Table 1. 3-D DLCTV Camera system geometric properties

Description	Variable	Value	Units
Back side-length of volume of interest	$a_{pb}$	15.14	mm
Front side-length of volume of interest	$a_{pf}$	25.73	mm
Depth of volume of interest	$a_z$	19	mm
Focal length of lens	$f$	119.90	mm
Magnification	$M$	1.344	-
Linear distance between lenses	$d$	90.53	mm
Linear distance between CCDs	$d'$	212.22	mm
Radial distance from optical axis to lenses	$\gamma$	52.27	mm
Radial distance from optical axis to CCDs	$\gamma'$	122.53	mm
Gain	$K$	0.000039	$\text{mm}^{-2}$
Apparent distance from lenses to front of volume of interest	$Z_a$	189.54	mm
True distance from lenses to front of volume of interest	$Z_{ta}$	230.33	mm
Apparent distance from lenses to start of domain of interest	$Z_{min}$	162.39	mm
True distance from lenses to start of domain of interest	$Z_{tmin}$	194.12	mm
Apparent distance from lenses to reference (focus) plane	$L$	209.09	mm
True distance from lenses to reference (focus) plane	$L_t$	256.39	mm

It should be noted that in the above table, the apparent values,  $Z_a$ ,  $Z_{min}$ , and  $L$  are those values derived directly from the DDPIV equations (Eqns. 8-19). The true values of these variables take into account the actual experimental setup, to be discussed later, thus providing the optical corrections due to the differing refractive indices between the air, glass/acrylic, and water in the optical path between the camera and the LCs.

Once the above geometric properties of the system were calculated, the physical design of the camera system could be considered. While not strictly a necessity, the desire to use this system in multiple different orientations and physical locations demands that all aspects of the imaging system be physically affixed to one another. Having all

four lenses and all CCDs contained in one box greatly aids the ease with which this system can be setup, calibrated, moved, and transported. In addition, an enclosed case can provide protection from any outside interference, thus preventing external light from saturating the CCDs or delicate components being damaged by physical contact. The resulting enclosed design of this full 3-D DLCTV system as well as its implementation is shown in Figure 26 below.

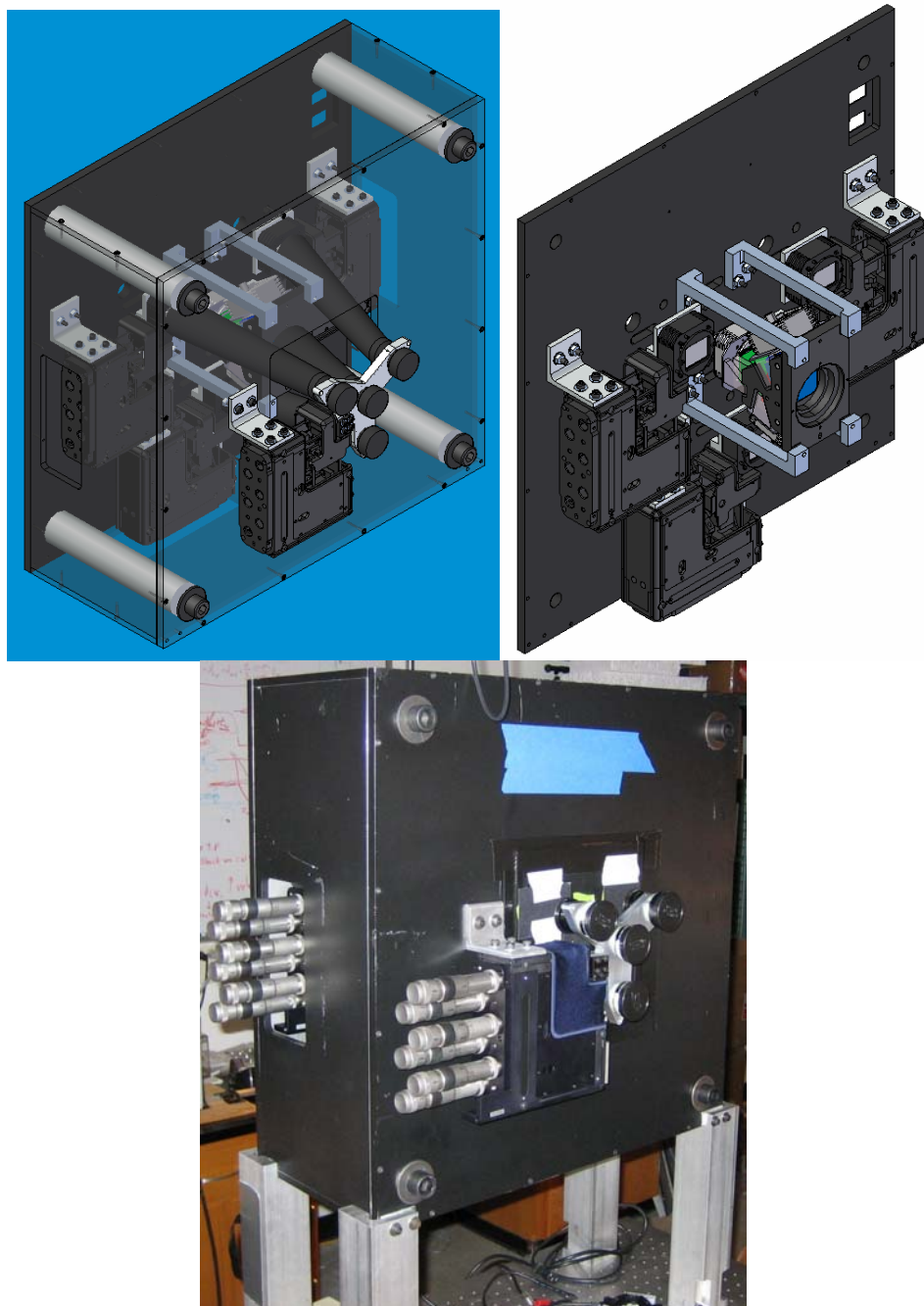


**Figure 26. Design of 3-D DDLCTV Camera System**

This design is based on the desire to have an enclosed camera system that can provide ample ability to position the system's optical components while minimizing the

uncertainty in their position. As a result, the main structural framework of the system consist of a rear “camera” plate, which is mounted to the front “lens” plate by four extremely sturdy aluminum connecting rods. In this manner the camera plate can help form a consistent sensor plane in which to position the CCDs, while the lens plate can do the same for the lenses. By having the connecting rods precision machined to the correct length, the geometric arrangement of the camera system is maintained to the maximum extent possible.

### **3.1.1 Translation Stage Selection**

While the design discussed above focused on maintaining system positioning integrity, additional care is also needed. CCDs positioned based on tight machining tolerances would be located relatively close to their correct position, but due to the resolution of the system, even a thousandth of an inch of position error could result in significant errors in imaging alignment, distortion, or particle identification. For example, a thousandth of an inch of purely translational CCD misalignment would result in approximately three pixels of image misalignment. This amount of error could prevent identification of image triplets and thus make the calculation of flow velocity impossible. As a result, much greater accuracy and resolution in CCD positioning is required. To accomplish this, the three black and white CCDs as well as the lens assembly were mounted on high accuracy six degree of freedom translation stages. These stages, manufactured by Thorlabs, have both a coarse and a fine adjustment on all six axes with total range of 12mm in translation and  $6^\circ$  in rotation for the coarse throw, and  $300\mu\text{m}$  and  $0.3^\circ$  for the fine throw. The corresponding listed resolutions of the stages are  $1\mu\text{m}$  and

$1.1 \times 10^{-3}^\circ$ , and 100nm and  $1.1 \times 10^{-4}^\circ$  for the coarse and fine adjustments respectively. It should be noted however, that the stage position is controlled using micrometer heads for each of the six degrees of freedom. As a result, the ability of the stage to achieve the listed resolutions is dependant on the skill of the operator. In practice, maximum resolution is on the order of 500nm in translation and  $5.5 \times 10^{-4}^\circ$  in rotation. Figure 26 displays four of these stages, which are the large, black, L-shaped objects seen supporting the lenses on the front plate and the three black and white CCDs on the back plate. Using these stages, all critical optical components of the system can be aligned relative to one another to correctly place them in space according to the design. However, the limiting factor of these stages is their load capacity. Each stage can only adequately support and accurately move up to 1kg. Objects mounted to the stage above 1kg can cause “creeping” of stage position or an undesired translation or rotation when one of the micrometers is adjusted. As a result, the selection of lenses and CCDs reflected this requirement.

### **3.1.2 CCD Selection**

CCD selection was a critical choice in the creation of this system, as it directly affects the size and quality of the volume that can be imaged. Poor quality can increase error in the system, while too small a size might not be able to fully capture flow phenomena, thus making size, quality, and weight determining factors. As a result, Illunis Corp’s XMV-11000 was used in this research. This camera is small (3” x 3” x 1.25”), lightweight, and still has desirable performance qualities. These include an eleven megapixel rectangular CCD (4008 x 2672 pixels), well depth of 60,000 electrons,

and a signal to noise ratio of approximately 30dB. In addition, camera performance can be modified through the use of software provided by Illunis to increase camera gain, change CCD exposure time, etc. This greatly eases processes such as white balancing the color camera assembly or synchronizing camera exposure with the pulsed illumination system. Since they are not clearly visible in the design drawing shown above, the three black and white cameras are shown mounted to their corresponding translation stages in the image below.

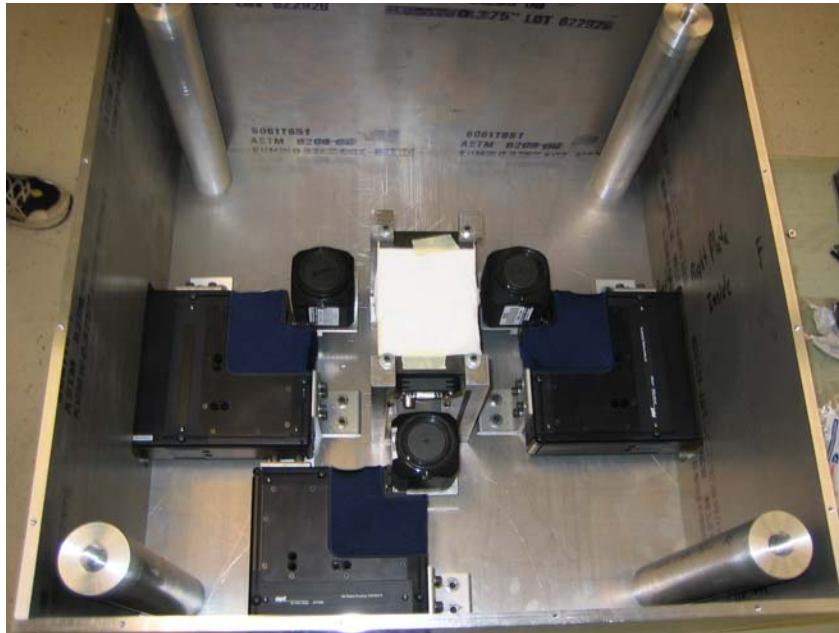


**Figure 27. Partial camera assembly displaying Illunis XMV-11000 CCDs**

### **3.1.3 Lens Selection**

While camera selection is critically important in the performance of the system, lens choice also has a critical impact in not only the performance, but also the design of the camera system. This is due to the lens focal length,  $f$ , being one of the four variables

from which all other dimensions of the system are derived. This derivation relied on the assumption that the lenses used will be thin with a large F-number, defined in Equation 28 below as the lens focal length divided by the lens diameter.

$$F = \frac{f}{D} \quad (28)$$

If the selection of a lens for the system is not in compliance with this assumption, system geometries could be incorrect. In addition, lenses with a high F-number will generally help minimize spherical aberrations that can cause distortion in the triangular image triplets, especially at the edges of the image (Kajitani and Dabiri 2005). In addition to the requirement of a large F-number, the lenses must also be lightweight enough that four lenses assembled together do not exceed the overall weight limit of the Thorlabs translation stage.

As a result of these requirements, Schneider Optics Macro-Symmar 5.6/120HM lens was selected. Small and lightweight, this lens has an F-number of approximately 3.7 with a focal length of 119.9mm that is toleranced to within  $\pm 1\%$ . This low uncertainty in the lens focal length is important due to its propagation into the error of the system. Small differences in the focal length can require large changes in the necessary positioning of the optical components that could exceed the ranges of the translation stages. Also important to note for this lens are its distortion and transmittance. A high distortion can lead to errors in the image triplets while low transmittance will affect the total amount of reflected light seen by the CCDs, which must be maximized. The Macro-

Symmar lens has transmittance above 90% for most of the visible spectrum and less than 0.5% distortion even at the lens' edge, as seen in Figures 28a and 28b.

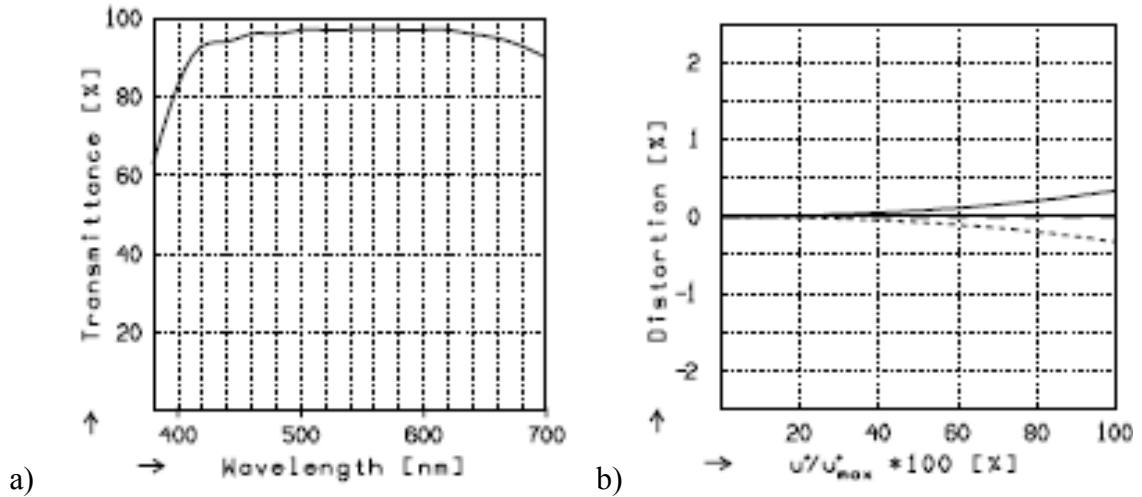


**Figure 28. a) Lens transmission over visible spectrum b) Lens distortion as a function radial position on the lens (in percent of lens radius) (Provided by Schneider Optics)**

Four of these lenses, one for each camera, are mounted in a lightweight, custom-built lens holder such that the total weight of the assembly is below the maximum load capacity of the translation stages described above. They are arranged in an equilateral triangle formation in accordance with the design spreadsheet, and mounted on a translation stage attached to the front plate. The lens holder can be seen in below in Figure 29 as the y-shaped component on the front of the camera box.



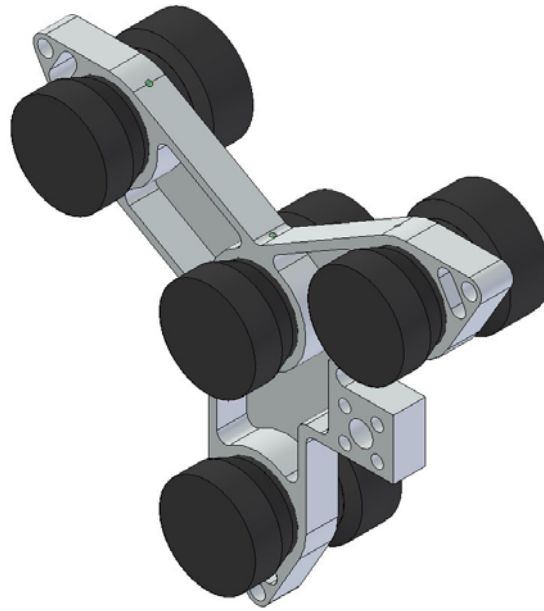


**Figure 29. Rear view of lens holder assembly showing the lens holder (Grey) and lenses (Black)**

Using this assembly, each lens is placed such that their individual lens planes are aligned, thus defining a single lens plane for the camera system. The lens holder can then be translated and rotated using the stage to position the lens system correctly with respect to the cameras.

### **3.1.4 Pinhole Design and Testing**

Related to the lens, and required in the DDPIV concept, is the addition of an aperture (pinhole) to the lens. The aperture must be placed on the lens plane for full effect, and in this regard the Macro-Symmar lenses provide a simple solution. These lenses are a “two-part” lens, meaning a series of lenses aligned with each other and separated by a small spacer tube. The optical center of the lens system (which defines the lens plane) is conveniently located at a point inside this spacer. As a result, by machining

a seat into which it can sit, a pinhole aperture can be placed inside the spacer at the lens plane. This setup is shown in Figure 30.

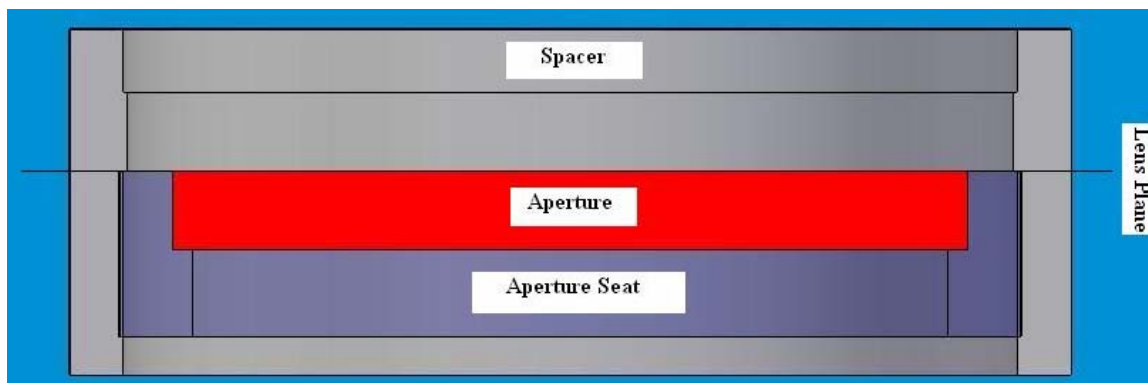


**Figure 30. Cross-Sectional drawing of spacer with aperture and aperture seat**

The required depth of field of the imaging system dictates pinhole size. The farther from the reference plane the volume of interest is, the smaller the aperture must be to create usable LC particle images. However, too small of a pinhole will decrease the amount of light that reaches the CCDs to such a point that either blank or unusable, dark images are obtained. Thus pinhole size must be balanced between these two competing requirements. In order to determine proper size, pinholes of 1mm, 2mm, 3mm, 4mm, and 5mm were obtained from National Aperture Inc. This range was based on previous experience in the necessary depth of field for this type of application.

To obtain the best possible combination of light and depth of field, a small square container of the same approximate size of the volume of interest was constructed and filled with LC-seeded water. This container was then placed into a filled fish tank at the location of the volume of interest. Using direct forward scattering (i.e. light source

pointed directly at the camera), a high intensity halogen lamp was used to illuminate the particles. While at this angle the particles do not reflect light, they do eclipse the lamp, thereby leaving a shadow on the CCD whose focus will be indicative of whether the required depth of field has been achieved. Each of the five pinhole sizes was tested, starting from 5mm. By beginning at the largest aperture and then decreasing, the pinhole that is first observed to provide adequate depth of field for the particles in the container is the best choice. It will provide the maximum amount of light from the set of all pinholes that meet the depth of field requirement. Images of these tests are displayed below in Figure 31. Without a pinhole, the particles are so diffuse that they are indistinguishable. With a 3mm pinhole a low particle density can be seen, but appears defocused, while a 2mm pinhole brings a larger number of particles into a respectable level of focus. By decreasing the aperture size further, the amount of light that reaches the CCD is significantly diminished, and the images unusable. As a result, the 2mm aperture was selected as the best choice.

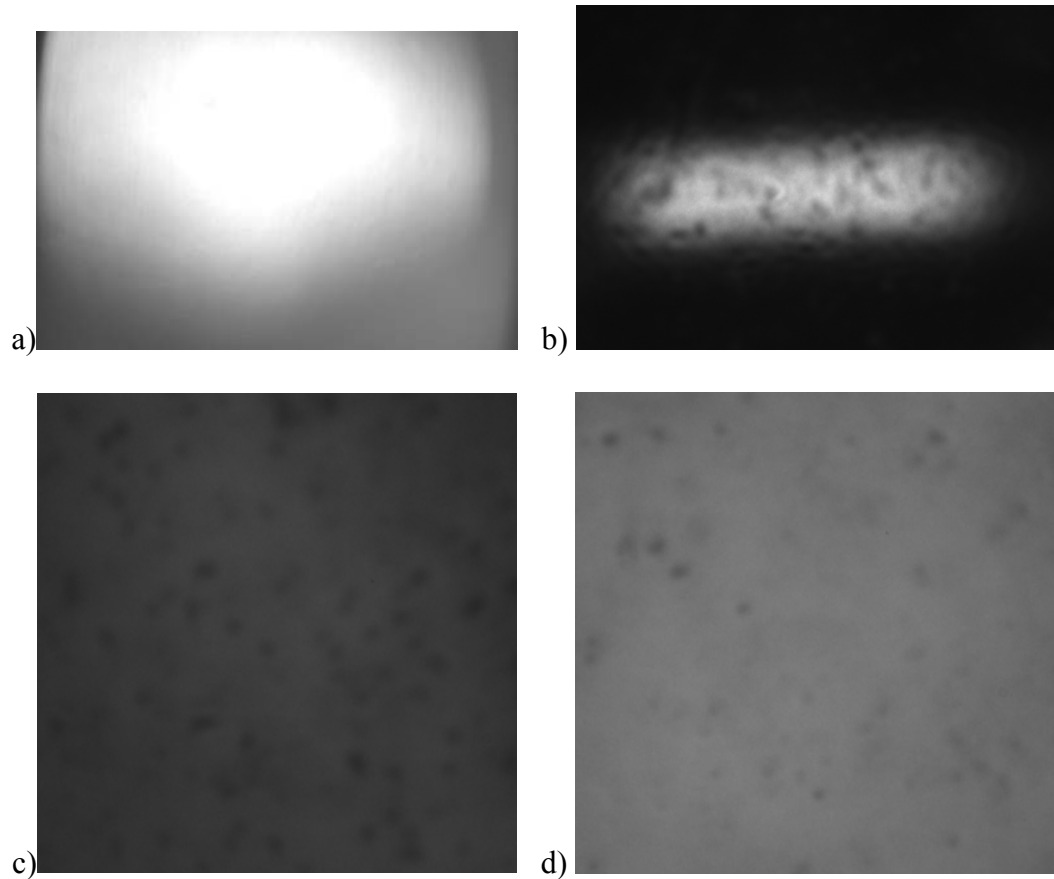


**Figure 31. Pinhole testing images for a) no pinhole b) 1mm pinhole c) 2mm pinhole and d) 3mm pinhole**

### **3.1.5 Color Camera Design**

The next aspect of the camera design that must be discussed is the color camera assembly. In order to keep the imaging hardware consistent, the “fourth,” or color camera in the DLCTV system is actually an assembly of three separate Illunis XMV-11000 cameras. Light enters the assembly through a prism that splits it evenly, with a third of the total light passed to each camera. This prism also arranges the light such that each camera sees the same image, a topic to be discussed later in this section.

In order to create color, each of the three cameras must be assigned to a particular primary color: red, green, or blue. As a result, each camera should only detect the wavelengths of light to which it is assigned, with the “red” camera only being passed red light for example. This is accomplished by placing color filters in front of each camera whose transmittance properties are shown in Figure 32 below.

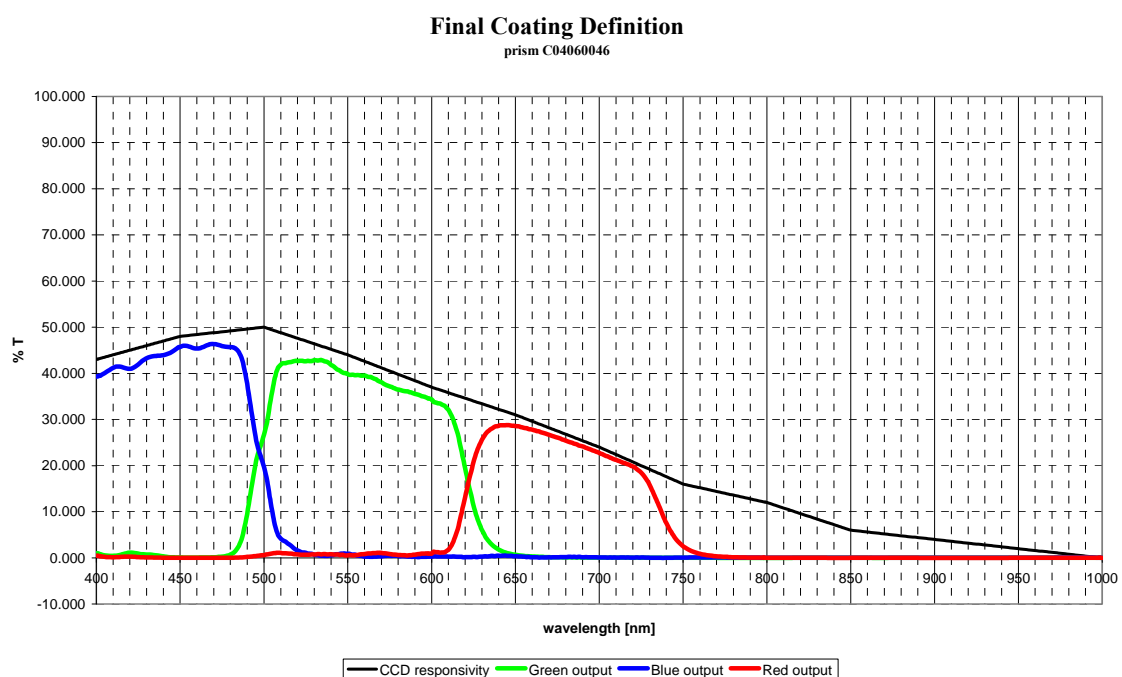


**Figure 32. Transmittance properties of color camera filters (Provided by Optec)**

These filters were chosen so that an image created by adding the three colors together would approximate the color response of the human eye. However, upon initial testing it was discovered that a color balance was still necessary. This is due to differing magnitudes of light transmitted by the red, blue, and green filters, as seen above. It should be noted that the black line in the above figure represents the responsivity of the

Illumis CCDs corresponding to each wavelength. Thus, the transmittance of the filters in the color camera is maximized for the highest possible total light intensity to reach the CCDs. To accomplish the white balance for this camera, a Macbeth Color Chart was used along with the adjustable digital gains of the three cameras to correctly match the observed RGB values with those listed on the color chart. This testing was accomplished using a short arc-xenon lamp in order to best approximate the lighting conditions of the actual testing. While white was the principal color against which the cameras were calibrated, the color response of others such as pure red, green, and blue were also observed to ensure proper color matching. Since the blue filter has the highest transmittance, it naturally provides the brightest image. As such, to attain white balance the other two cameras' gains were increased to match the blue. Since the red filter is the darkest of the three, the red gain had to be increased to approximately four times normal in order to match the blue, while the green camera only required an approximately 50% increase. It should be noted that the white balance, once established, also scales linearly, meaning that a 50% increase, for example, to the gains of all three cameras will increase the gain of the system without affecting the quality of the color balance.

Although it can be seen in previous figures, to provide increased detail, images of the color camera assembly's design and implementation are shown below in Figure 33.

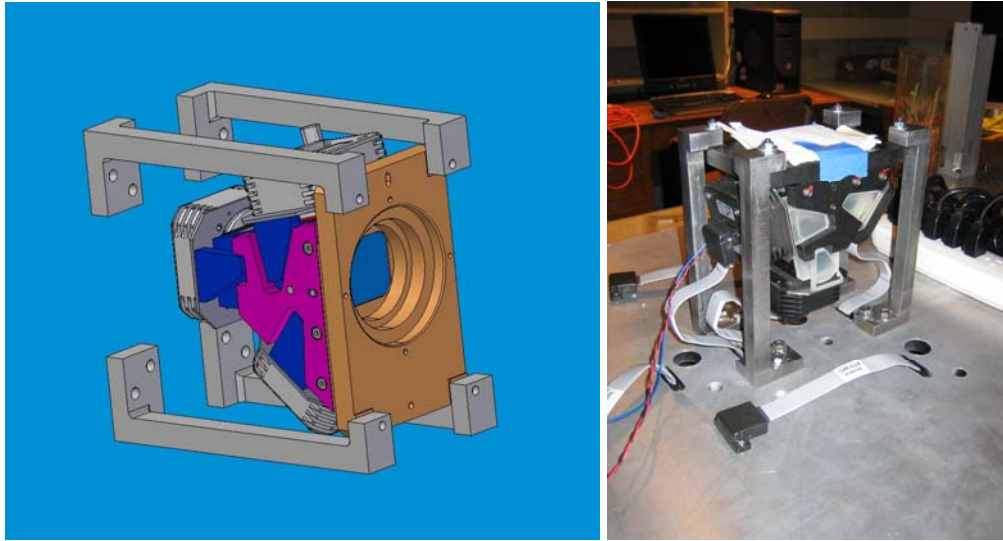


**Figure 33. Color camera assembly design**

Since this assembly is too heavy to mount on a translation stage, it must be statically affixed to the camera case. As a result, its viewing axis creates the optical axis of the camera system as a whole, meaning that all other cameras and lenses must be calibrated around it. Thus, to ensure that the camera system maintains maximum integrity, the connecting rods that mount the color camera to the case (shown in grey in the figure) were fabricated from steel to help prevent any bending from the color camera's significant weight (approx 20 lbs). A basic FEM analysis of the assembly indicated that very little bending, on the order of approximately 4 arc seconds of rotation and  $175\mu\text{m}$  of vertical deflection, will occur. These deflections are well within the adjustment ability of the stages and thus the configuration of the system will be adequately maintained with this design.

Initial imaging performed with the color camera revealed a small misalignment between each of the three images. After discussions with the camera manufacturer, this

misalignment was proven to be the result of the chromatic aberration characteristics of the Schneider lenses. Chromatic aberrations are present in virtually all lenses and represent a small dependence of the index of refraction of the glass on light wavelength. In essence, certain colors of light passing through the lens will focus in a slightly different position than others. The manufacturer, using their own lens, performed initial alignment of the color camera system via the placement of the three CCDs. This CCD placement accounted for the aberration present in their lens, but the Schneider lenses and those used by the manufacturer have different chromatic aberration qualities. Thus, the CCD placement does not account for the aberration present in the Schneider lenses, resulting in the observed image misalignment.

As the center of the three cameras, the green CCD was used as a basis of comparison for the other two. Thus using the green image as a datum, the red and blue images displayed misalignments on the order of one to four pixels at any given spot on the image. This misalignment can be seen below in Figure 34.



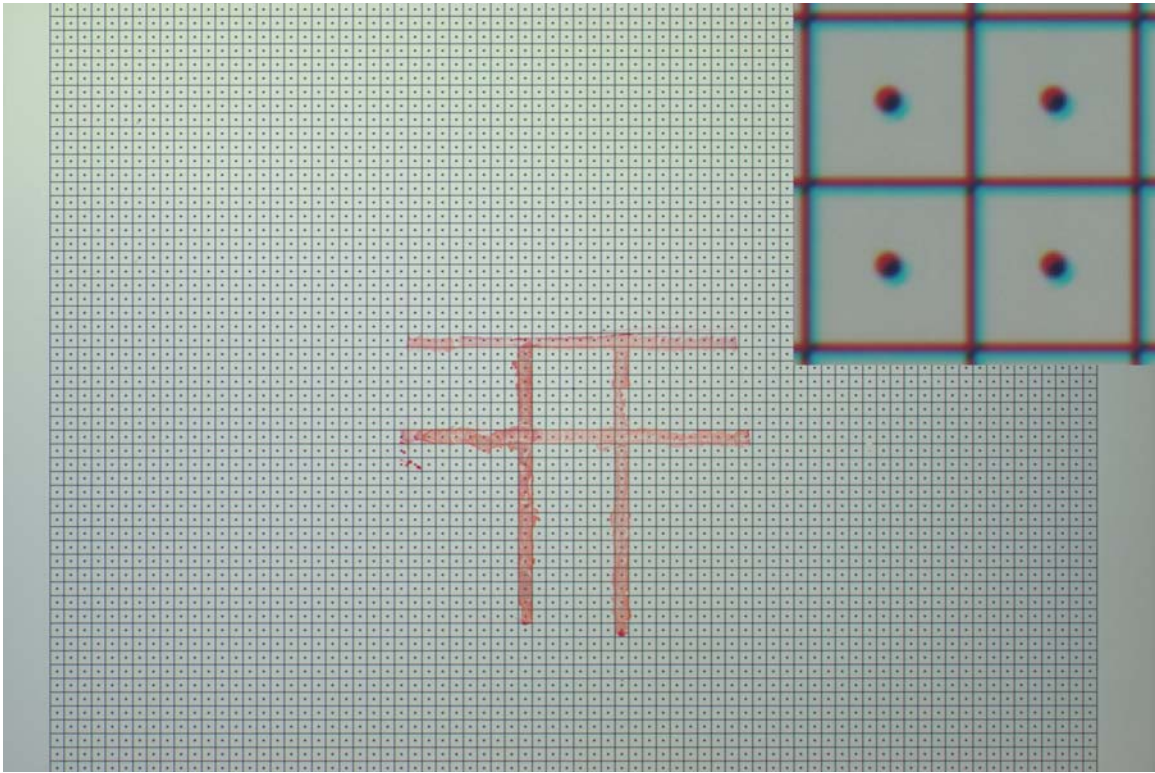


**Figure 34. Overlay of the three "color" CCDs prior to image correction**

These differences between the images translate into an unsatisfactory overlay of the red, green, and blue color images, which in turn leads to poor color quality and potential difficulty in particle identification. Due to the fixed nature of the color camera assembly, this misalignment cannot be corrected through the shifting of the respective red and blue cameras. As such, images from the two misaligned CCDs must be post-processed to correct this error.

This image correction consists of first imaging the calibration target, to be fully described in a later section, on all three of the color CCDs, and then transforming each of the misaligned images to match the green image. This is accomplished through the use of a perspective transform, as outlined in Jähne (1997). To determine the mapping

coefficients for the red-green and blue-green transforms, the green camera is taken as the desired output, and the red and blue cameras are the inputs to be transformed. The many grid intersections on the calibration target are used as the mapping points, and are found by performing a correlation between a grid intersection template and the full image (Park and Gharib 1999). The resulting correlation data is then thresholded to isolate the regions of highest correlation (the intersections) and a peak finding algorithm is used to determine the center of the intersections to sub-pixel accuracy. After the transform is applied to the red and blue camera images, the corrected data is then transferred back onto the standard pixel grid using bicubic interpolation. For completeness, it should be noted that a spline-based interpolation method was also tried, but was significantly more computationally (and therefore time) intensive, while providing negligible change in the quality of the interpolation. The results of this post-processing can be seen in Figure 35 below in an overlay of the green image with the interpolated red and blue images.

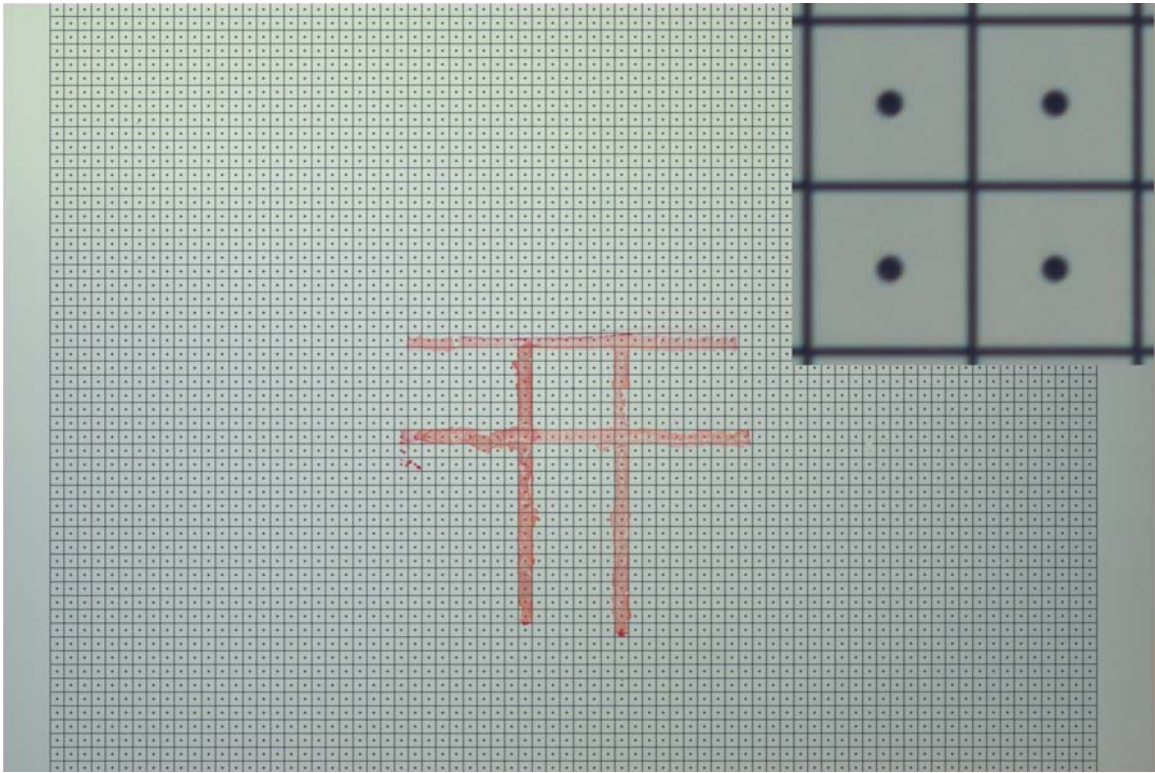


**Figure 35. Overlay of the three "color" CCDs after image correction**

Because the color assembly is fixed in place, once the mapping coefficients have been determined correctly, the same transform can be applied to every subsequent set of images.

Comparison of the locations of twenty-five equally spaced grid intersections on each of the three images showed that this method had successfully corrected the red and the blue images to match the green image to within an average of  $0.134 \pm 0.134$  pixels. The average X and Y deviations, from the green image, of those twenty-five points can be seen in the table below along with the corresponding error.

**Table 2. Overlay deviations and error for red and blue images**

	<b>Green-Red</b>		<b>Green-Blue</b>	
	<b>X</b>	<b>Y</b>	<b>X</b>	<b>Y</b>
<b>Average Deviation</b>	-0.250	-0.077	-0.153	-0.057
<b>Error</b>	0.137	0.094	0.148	0.157

Because of the quality of these overlays, the misalignment of the color camera has been accounted for.

### **3.1.6 Optical Isolation Tube Design**

The final aspect of the design that must be discussed is the optical isolation tubes. These can be seen in Figure 26 as the black, cone shaped objects that connect the CCDs to the lenses. Basic testing accomplished prior to the camera design indicated a strong need to control the lighting conditions of the test environment in order to obtain a good image. This testing was accomplished using a single CCD and lens aligned off axis in accordance with the DPIV equations to view a target grid placed in the focal plane. Due to an excess of light, any attempt to image the target without isolating the optical path of the system from the illumination device would result in a saturated image. By constructing a tube from the CCD to the lens such that the only light incident upon the CCD is reflected from the target through the lens, a good image was obtained. As a result, isolation tubes were included in the final design of the 3-D DLCTV system. Although the camera case will prevent a majority of excess light from reaching the CCDs, the tubes provide added confidence that the generated images are as clear and noise free as possible, and give a level of protection from dust and other foreign substances.

The fabrication of the 3-D DLCTV system, with the exception of the color camera, was accomplished at the University of Washington Department of Aeronautics and Astronautics machine shop. The color camera assembly was custom built in Italy by the Optec Company. All fabricated pieces of the system were constructed from 6061 Aluminum with the exception of the color camera mounting brackets (steel) and the optical isolation tubes (cardboard).

### **3.2 Water Filled Prism Design**

Due to the nature of the 3DDPIV system described above, each of the three CCDs used to measure velocity are placed away from the optical axis. This means that each of these three CCDs view the imaging volume at an approximately 14.5 degree angle from it. In general, off axis imaging can cause distortion and astigmatism in the image if proper precautions are not taken. In this case, the lens selection discussed above helps minimize these effects. As a result, initial imaging with these cameras showed no distortion due to their placement. However, these initial images were taken of a target suspended in front of the camera, meaning the cameras were viewing the target through a single medium, air. Although imaging through air proves valuable for camera calibration, this camera is designed to image LC particles suspended in water. This necessitates imaging through three separate mediums: air, glass/ acrylic, and water.

Therefore, additional test images were taken of a target and particles placed at the focal plane inside of a water-filled test tank. Due to the tank's presence, rays emanating from the target bend twice as they pass at an angle from water to glass and then glass to air. This bending is a product of the different indices of refraction of the mediums, and

its magnitude varies directly with the size of those differences. The result of this bending is the introduction of a sagittal (radial) astigmatism into the optical system. This astigmatism takes the form of a blurring in each image directed away from the optical axis. This blurring is non-trivial and makes particle identification nearly impossible. Images of particles from two of the off axis cameras with the astigmatism present and a simultaneous image from the center camera that is astigmatism free, are shown in Figure 36 below.

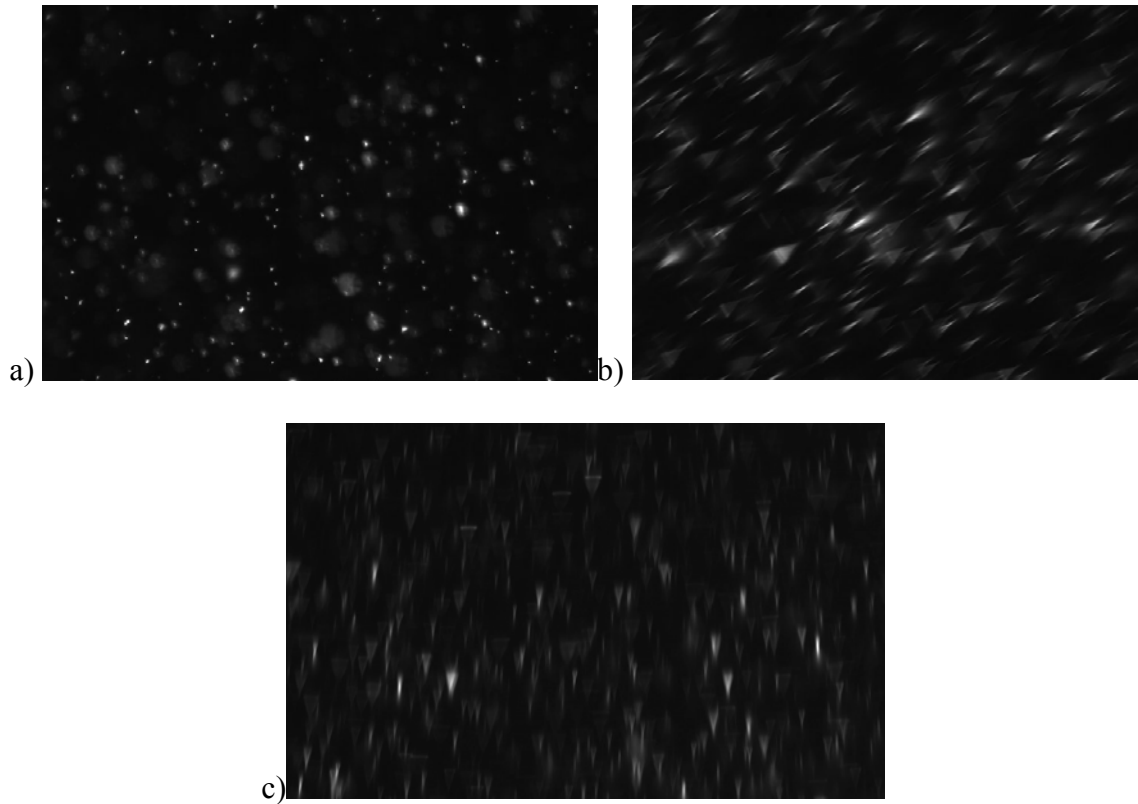


**Figure 36. Particles images showing the effect of a large viewing angle from a) Center CCD b) Top-Right CCD c) Bottom CCD**

Because the above astigmatism is the result of differing indices of refraction between mediums, as well as off-axis imaging, eliminating it requires minimizing one or

both of those causes. Due to space constraints inside the camera, decreasing the imaging angle to less than 14.5 degrees is not possible while still maintaining optimal resolution and imaging volume size. As a result, the index of refraction effects must be minimized. This can be accomplished through the use of a liquid filled prism as described by Zhang (1995), and Prasad (1995), which consists of a glass prism whose front faces are orthogonal to each camera's optical path and that is filled with the same liquid as the test section (water in this case). This prism is then placed against the test section, with each face aligned with its corresponding camera. The design of a water-filled prism for this camera system is shown in Figure 37 below, while the optical application of the prism to the imaging system can be seen in Figure 38.



**Figure 37. Water-filled prism design for 3DDLCPTV camera**



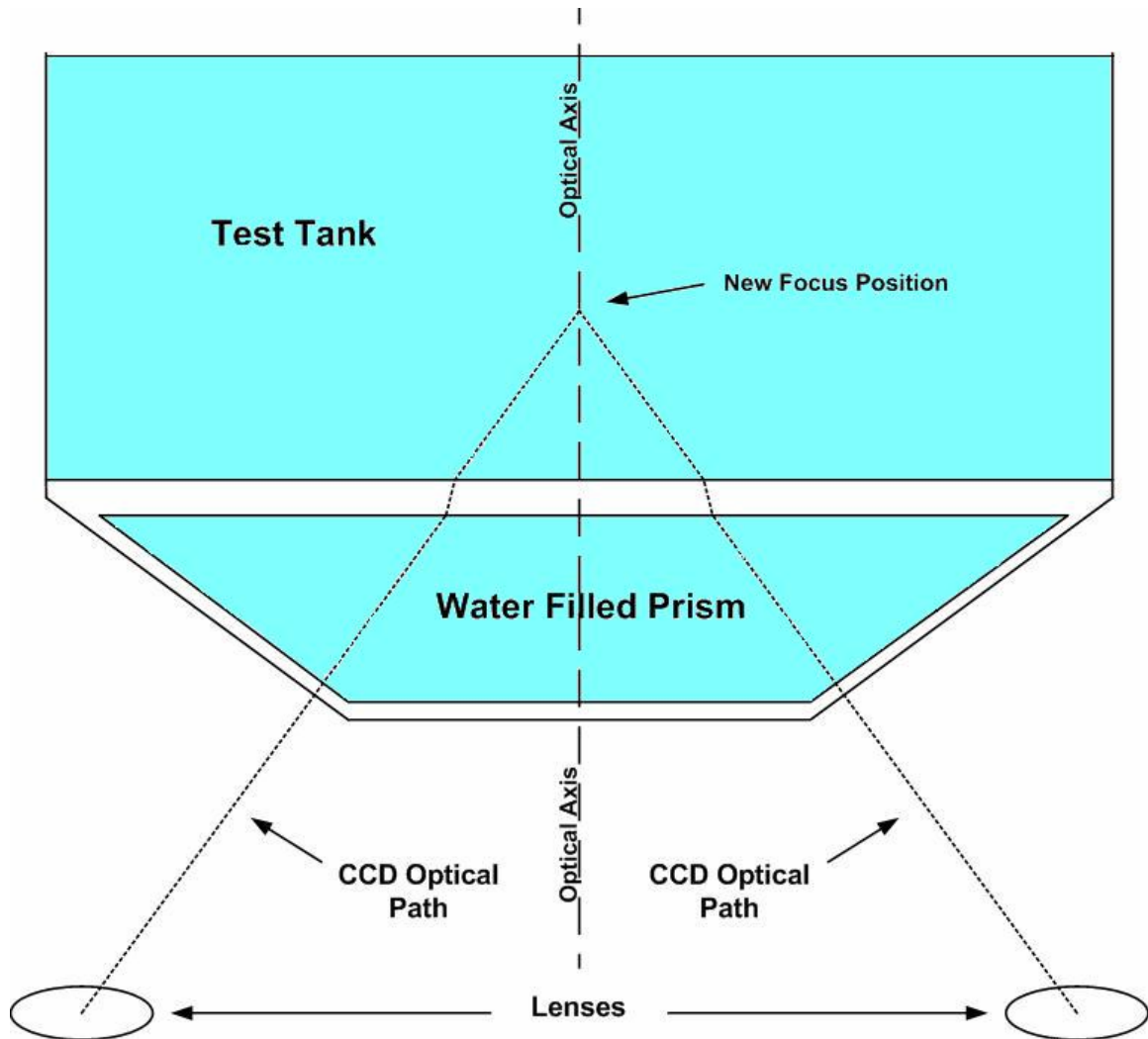


**Figure 38. Application and ray tracing for a single off-axis CCD using a water-filled prism**

Through the use of this prism, the bending of light rays due to differing indices of refraction is nearly eliminated. This is due to the rays transitioning between mediums at approximately zero angle, thereby passing directly through without bending. Because of this fact, the only difference from purely single medium imaging is the slight shift in the rays caused by their passage from the water-filled cavity, through the glass wall of the test tank, and into the water of the test section. In previous literature, this shift has been



ignored due to its small magnitude. However, due to the high precision of this camera system, any added approximations yield increased and unacceptable errors in particle velocity. To minimize these errors, the equations that calculate the dimensions of the optical system described above were re-derived to take into account the use of a water-filled prism including the small shift term. The complete derivation for this system can be found in Appendix B, while the three equations that are altered by addition of the prism are listed below

$$Z_{t_{\min}} = Z_{\min} + \left(1 - \frac{\tau_w}{\tau_g}\right)t_w \quad (29)$$

$$L_t = L + \left(1 - \frac{\tau_w}{\tau_g}\right)t_w \quad (30)$$

$$Z_a = d_{cw} + d_{wd} + \frac{\tau_w}{\tau_g}t_w \quad (31)$$

where  $d_{cw}$  is the distance from the lens plane to the front face of the test tank's front wall,  $d_{wd}$  is the distance from the back face of the front wall of the test tank to the start of the volume of interest,  $t_w$  is the test tank wall thickness,  $\tau_w$  is the index of refraction of water, and  $\tau_g$  is the index of refraction of glass. By utilizing this prism, images of objects inside

the water-filled test tank now show no sagittal astigmatism, as shown in images of a test target shown in Figure 39 below, with and without the prism.

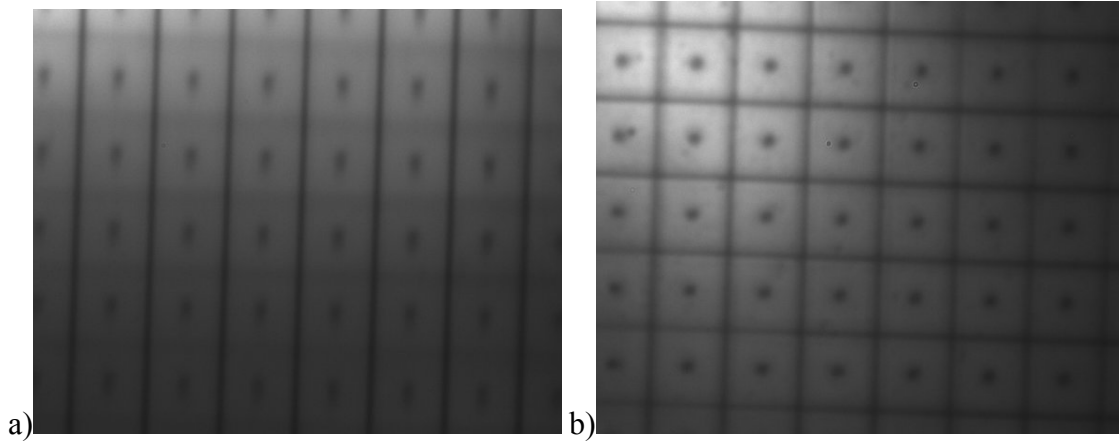


**Figure 39. Target images from the bottom CCD while a) using no prism b) utilizing a water-filled prism**

### **3.3 Camera Redesign**

While the prism described above effectively eliminates astigmatism in images taken of objects in water, the changed equations discussed above required alteration of the camera design spreadsheet to account for this new and different optical system. These changes had a ripple effect on all values listed previously in Table 1, in some cases changing them substantially. As a result, a redesign of the camera was required to account for these changes. The new dimensions of the redesigned camera, imaging volume, and optical system are displayed in Table 3 below while the new design spreadsheet can be seen in Appendix A.

**Table 3. Re-designed 3DDLCPTV camera system geometric properties**

<b>Description</b>	<b>Variable</b>	<b>Value</b>	<b>Units</b>
Back side-length of volume of interest	$a_{pb}$	35.6	mm
Front side-length of volume of interest	$a_{pf}$	26.4	mm
Depth of volume of interest	$a_z$	15.2	mm
Focal length of lens	$f$	119.90	mm
Magnification	$M$	.858	-
Linear distance between lenses	$d$	116.36	mm
Linear distance between CCDs	$d'$	216.20	mm
Radial distance from optical axis to lenses	$\gamma$	67.18	mm
Radial distance from optical axis to CCDs	$\gamma'$	124.82	mm
Gain	$K$	0.000039	$\text{mm}^{-2}$
Apparent distance from lenses to front of volume of interest	$Z_a$	235.87	mm
True distance from lenses to front of volume of interest	$Z_t$	236.70	mm
Apparent distance from lenses to start of domain of interest	$Z_{\min}$	192.25	mm
True distance from lenses to start of domain of interest	$Z_{t\min}$	193.08	mm
Apparent distance from lenses to reference (focus) plane	$L$	259.65	mm
True distance from lenses to reference (focus) plane	$L_t$	260.48	mm

Practically, this redesign required the shortening of the camera box and connectors, fabrication of a new lens holder and calibration rods, and resulted in an increase in the size of the imaging volume, as seen above. These changes are not trivial, as increasing imaging volume size will decrease the size of the LC particles on any given image and lower image resolution, as well as require additional illumination area. However, this new design still provides enough resolution to effectively compare to LES simulations, and particle size as well as illumination area can be increased. Thus, the new design is adequate for this investigation.

### **3.4 Flashlamp Selection**

While the 3DDLCP TV camera system provides the ability to image and calculate temperature and velocity fields, the second part of the overall testing system is the illumination source. While not as important as the camera itself, the illumination source proves critical, as without a high intensity of light concentrated in a short duration, the CCDs will not satisfactorily image the LC particles. The low reflectivity of LC particles and the use of small apertures, as well as the design of the color camera itself (prism and color filters) mandate that an extremely high intensity source be used. As discussed in the background, LCs reflect specific bands of the spectrum of light that are incident upon them. As a result, the full spectrum white light and high intensities provided by a short arc Xenon flashlamp are required for this effort. In addition, the flash duration of this lamp must be short enough to “freeze” LCs that are in motion. If the pulse duration is too long or the particles move faster than anticipated, the result is streaking in the images of the particles on the CCD. This adds uncertainty in finding the particles accurately and must be avoided. From experience and calculation the necessary pulse duration is on the order of 10-20  $\mu\text{s}$ .

#### **3.4.1 Linear In-House Lamp – Design and Testing**

The first attempt at meeting these criteria was the use of an in-house xenon flashlamp, custom built by the Department of Aeronautics and Astronautics resident electrical engineer, Dan Lotz. This lamp used a 3-inch bulb to create the necessary arc at an input power of approximately 10 Joules. Pulse durations of this lamp were on the

order of several microseconds, which was sufficiently small to eliminate particle streaking. Testing without apertures confirmed this result. Initially, the lamp utilized a small reflector taken from a previous camera system. Due to its small size and inconsistent, unknown shape, this reflector was judged inadequate as resulting images taken with the required 2mm pinhole resulted in extremely dark, unusable images. Several different options were considered for a new reflector including parabolic and elliptical designs. A parabolic reflector would collimate the emitted light as long as the bulb was placed at its focus. This is a desirable configuration for LCPT, and thus the parabolic reflector could achieve this result without the need for accurately placed optics and the reflective losses associated with them. However, a parabola whose shape meets the physical constraints of the system and creates a column of light of the approximate size of the volume of interest has a very small included angle. As a result, it can only reflect a small portion of the total light. Enlarging the parabola beyond that of the volume of interest would require custom optics to capture maximum light, thus negating the benefit of the parabolic design.

As a result, the elliptical design was chosen for this lamp. An ellipse with the bulb positioned at one foci will focus all reflected light onto the second focus. An optic can then be placed on either side of this focus to collimate the resultant light onto the volume of interest. In addition, an ellipse has the added advantage over a parabola of a much steeper shape. The result is that the total included angle of light incident on the reflector is much greater than that of a parabola. Because of these advantages, an elliptical reflector was designed to better harness the flashlamp's light. Because the relatively long arc gap of the bulb (approx. 3in) prevents the light source from being

treated as a point source, this reflector was designed two dimensionally. It was fabricated in-house and polished to a high reflectivity prior to use. The elliptical design and an image of the full flashlamp utilizing this new reflector are shown in Figures 40a and 40b respectively.

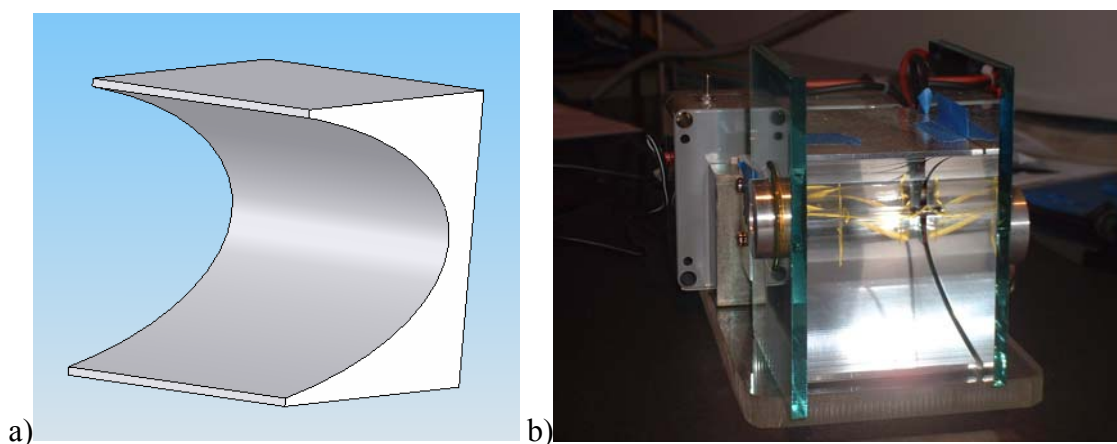


**Figure 40. Custom elliptical reflector a) design b) implementation**

Despite this reflector's improvement over the previous setup, the brightness of the resulting images was still grossly insufficient. Post-processing software gains had to be set to extremely high levels in order to capture faint images of LC particles. As a result of this, the custom lamp was discarded as a potential illumination source. Its power could potentially be sufficient, but without decreasing the arc-gap length there existed no way to harness its light better than previous attempts.

### **3.4.2 Perkin Elmer Parabolic Lamp - Testing**

The second flashlamp iteration was the result of a search for off-the-shelf high intensity xenon flashlamps. It was found that Perkin Elmer Corp. manufactures several

xenon lamps that, although functioning at a relatively low input energy (approx. 1J), can utilize the light in a much more organized and efficient fashion than had previously been accomplished. For that reason a FX-4400 Parabolic lamp, seen in Figure 41, was purchased from Perkin Elmer and used to conduct further testing. Despite its better ability to focus its energy, in order to achieve a maximal increase over previous efforts the input energy to this new lamp had to be maximized. As a result, its off-the-shelf power supply was altered by adding additional capacitors to increase the total input energy of the pulse to approximately that of the previous lamp, 10J. While this increase in energy had the effect of decreasing the life of the bulb, it allowed the effect of improved focusing of the light to be clearly distinguished.

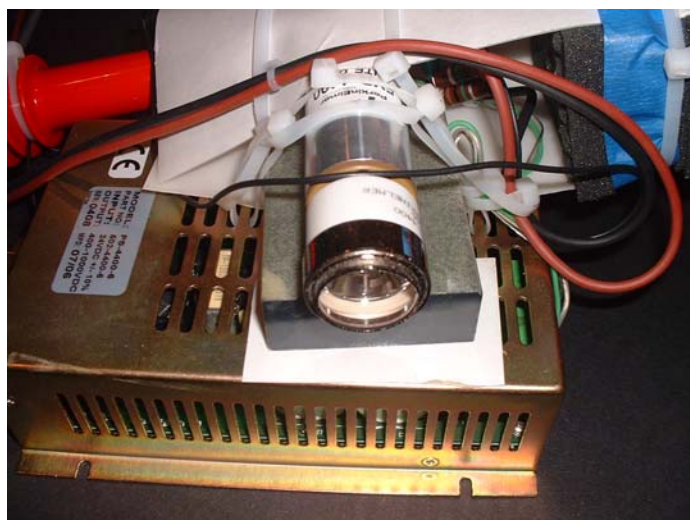


**Figure 41. Perkin Elmer FX-4400 Parabolic lamp with power supply and additional modifications**

This lamp was initially tested as is, meaning the lamp was fired directly at the volume of interest without any optics. Since the reflector utilized by this lamp was

parabolic, the resulting rays were approximately collimated. However, due to slight imperfections in the reflector, the light diverged by the time it entered the volume of interest. This divergence was small, but not insignificant, as the diameter of the spot created by the light increased by a factor of approximately 50%. As a result, initial results taken in this manner were not encouraging, and resulted in nearly blank images. Despite that fact, this new lamp still demonstrated an improvement over the previous attempt, as post-processing required a significantly smaller gain to be able to distinguish particles.

In order to counter the divergence discussed above, a converging optic of the approximate size of the diverged light spot was placed in the path of the light and directly adjacent to the test tank. This optic focused the light down to an area of the same size or smaller than the volume of interest, thereby greatly increasing the intensity incident upon the crystals. Using this method, crystals could be very clearly seen without an aperture, a feat which none of the previous efforts had totally accomplished. By illuminating from an approximately  $45^\circ$  angle, sufficient light was reflected from the crystals to provide vibrant color throughout the crystal's range. Color images taken at three different constant LC temperatures can be seen in Figure 42.



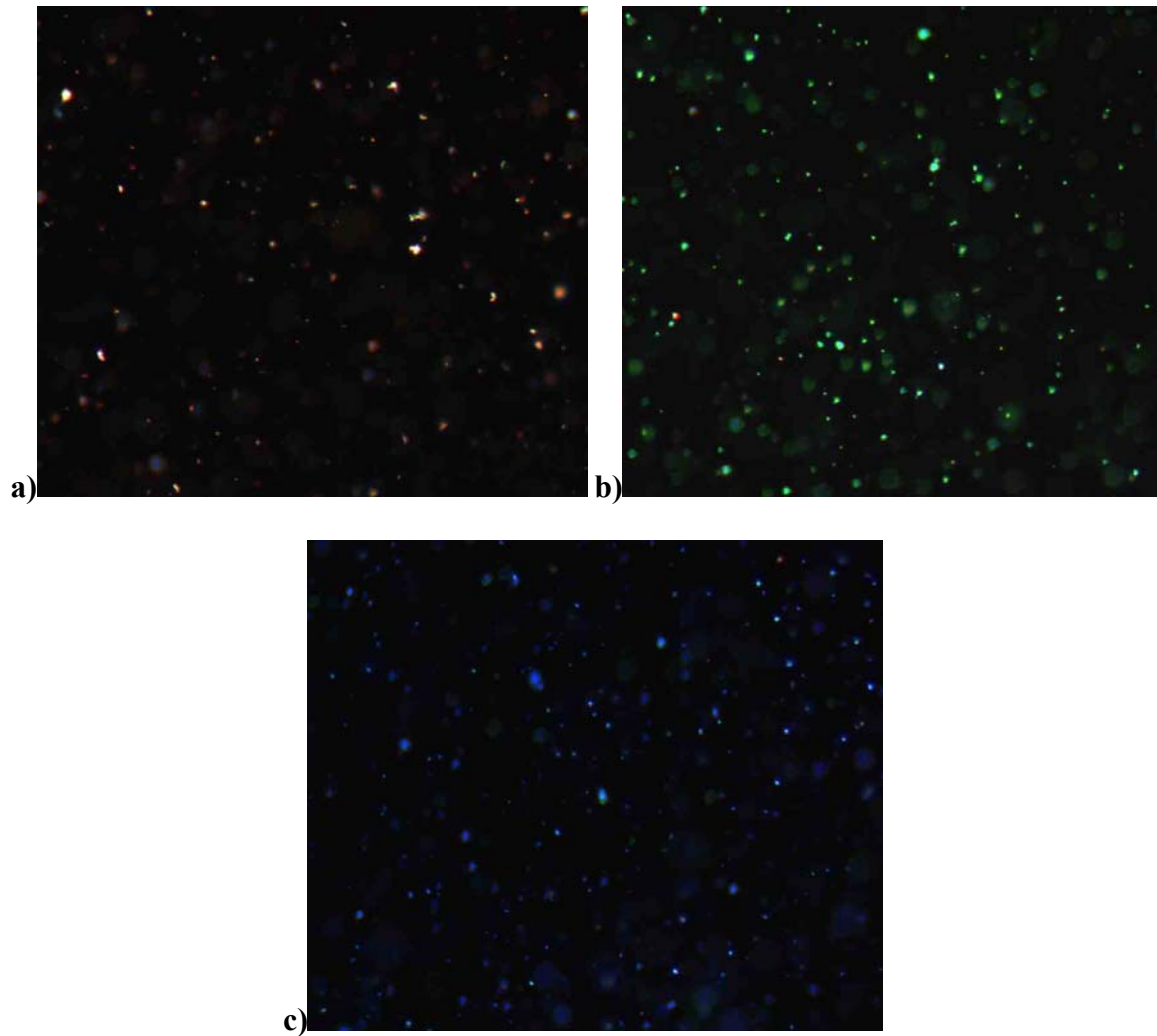


**Figure 42. Images of the LC's full color range using Perkin Elmer lamp with no aperture at approximately a) 24.5 degrees b) 25.5 degrees c) 26.5 degrees**

Despite creating quality images without a pinhole, the Perkin Elmer lamp, like its predecessor, could still not adequately illuminate the particles when a 2mm aperture was applied to the lens. Images taken with the pinhole proved extremely dark, and a gain setting of approximately 30 was required for a quality particle field to appear. This gain, which will be referred to as the LUT, was applied linearly. It operates on an 8-bit 0-255 scale, with 0 as the maximum setting and 255 corresponding to no added image

brightness. A LUT setting of 30 thus represents considerable image enhancement and results in significant image noise. So, due to the darkness of the pictures taken with a pinhole in place, this lamp was also discarded as an illumination source for this application.

### **3.4.3 Cooke Lamp – Testing and Reflector Design**

The failure of the Perkin Elmer lamp clearly indicated that although properly focused light can result in significant improvements in image quality, a greater magnitude of light is required than either of the previous lamps could produce. As a result of this, a search for extremely high-energy xenon flashlamps led to testing of the SensiFLASH 250 made by the Cooke Corporation. This lamp is designed specifically for short duration high intensity imaging with a maximum input energy of 200 joules spread over 200 microseconds that is produced from a 3mm long arc-gap. Although this pulse duration is too long to test actual flow phenomena due to streaking, the CCDs will be able to collect reflected light from the full pulse and thus give a good indication of how much more light is needed from the flashlamp.

Initially, the lamp was tested from  $45^\circ$  with a basic reflector and a condensing lens provided by Cooke, as well as the lens adjacent to the tank described previously. Images were taken of a still particle field to prevent streaking, with the 2mm aperture placed at the lens plane. The results of these first tests showed promise. Although a qualitatively acceptable particle field could only be obtained with a LUT setting of 40, this result was a small improvement over previous attempts. In addition, it was particularly encouraging because the methods used to harness the emitted light were fairly inefficient. As can be

seen in a picture of the SensiFLASH 250 in Figure 43, the total emitted light in this baseline optical setup is limited by the size of the lens attached to the front of the lamp.



**Figure 43. SensiFLASH 250 lamp with initial optical setup**

Because DLCTV requires that organized light illuminate the particles, only light rays that move directly towards the lens and are within its included angle can be captured and used. As a result, these optics can only capture a 2-D included angle of approximately  $56^\circ$ . In other words, a large amount of the increased energy of this new lamp is being wasted.

To counter this fact, a new reflector was designed and fabricated to increase the total included angle, and hence the total light “produced.” Due to the small size of the bulb’s arc-gap (3mm), it can be approximated as a point source of light. As a result, a

spherically shaped reflector centered on the bulb's arc-gap redirects rearward moving light incident upon it back through the arc gap along the same path it came. Because of this, any light rays that are within the lens' included angle will be captured and collimated by it, whether they are backward or forward moving. In essence, this new reflector doubles the total intensity of light in the test section. Figure 44a and b display this fact using 2-D ray tracing for both the initial setup and the spherical reflector.

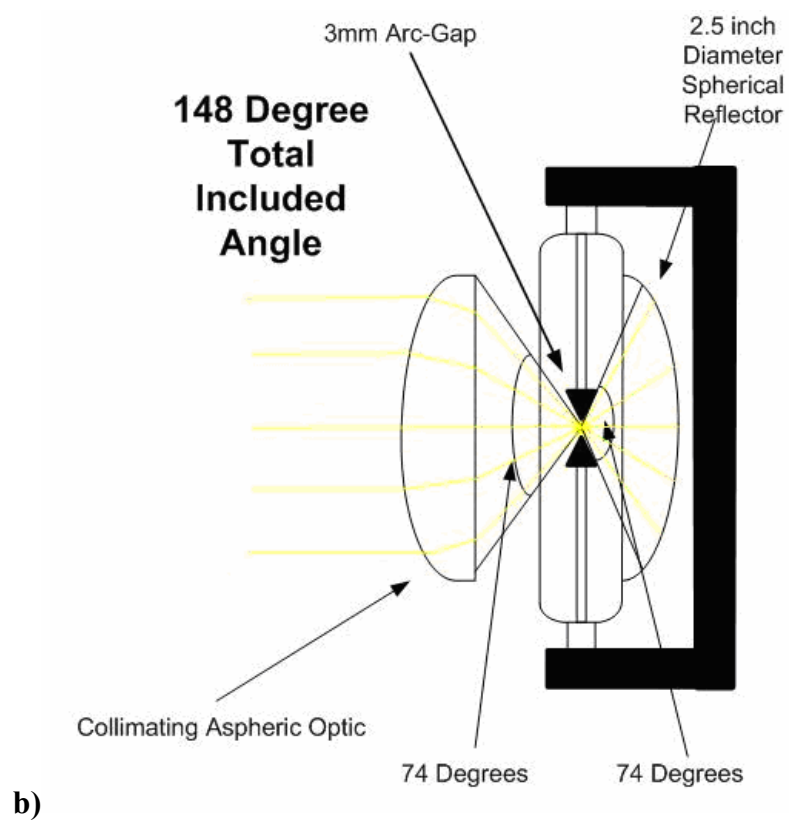
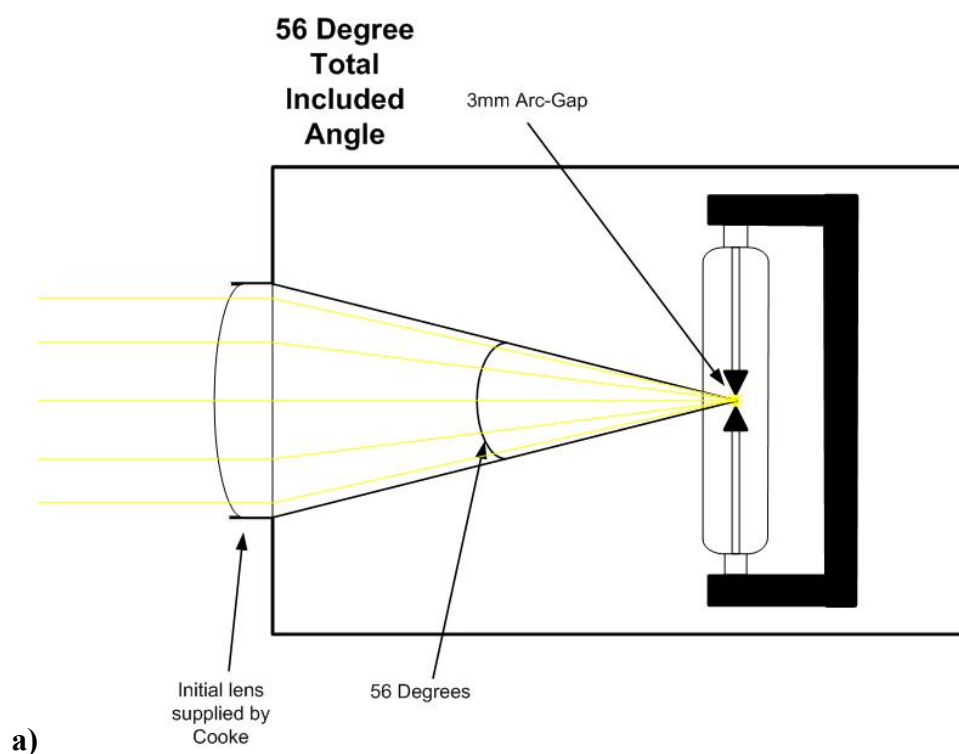


Figure 44. 2-D Ray tracing analysis using a) the initial optical setup b) the spherical reflector

In order to maximize the amount of light captured using this new reflector a new lens was also purchased to replace the one provided by Cooke. The included angle of the lens is a function of its size and focal length, as the lens must be positioned with the arc-gap at its focus. Increasing lens size and decreasing lens focal length (decreasing F-number) will increase the total included angle. As a result, an off the shelf aspheric lens with an F-number of 0.66 was selected to maximize the total included angle of the system. Aspheric lenses typically possess the lowest F-numbers and thus were the clear choice for this application. Figure 45 shows an image of the SensiFLASH 250 utilizing both the new lens and the spherical reflector.



**Figure 45. SensiFLASH 250 with new optical configuration**

This new optical setup was a success as it resulted in the expected performance increase of the system. By approximately doubling the lens' included angle, the intensity of light incident upon the crystals effectively doubled. Images taken with this new setup required a LUT setting of 80 to produce a particle field image of comparable quality. Despite this fact, two major problems remained. The first was that the large pulse duration of this lamp caused streaking when images of moving LC particles were taken. Second, although light intensity increased significantly over previous attempts, it was still insufficient. A LUT setting of 80 increases image noise, causing the center camera assembly to produce a dark and essentially colorless combined image. This fact makes finding particle temperature from the image impossible. Because of these two issues, additional light intensity is needed and pulse duration must be shortened before usable images can be obtained.

To counter these issues, a two-pronged approach was used to both improve the reflector and the power of the lamp. The spherical reflector was chosen due to its ability to double the included angle captured by the lens while also being easy to implement. Given the space constraints of the lamp, a fully three-dimensional ellipse, while more difficult to fabricate, can harness the most light out of any reflector shape. As discussed previously, the use of an elliptical reflector necessitates the placement of a lens at a precise distance from the bulb to organize the light. The total angle of light that this lens can collimate drives the shape and performance of the reflector, while its size must be approximately that of the volume of interest. Because light reflected off of the ellipse will focus on its second foci, it was treated as a point source of light. To maximize the amount of light captured, the largest angle at which light rays approach the second foci

must match the largest angle the lens can collimate. In this manner lens availability drives ellipse shape. A weak lens with a large focal length requires a steep ellipse, while the opposite is also true.

Because of the physical size of the bulb, a large clearance hole must be drilled through the reflector centered at the ellipse's foci. This hole decreases the included angle of the reflector as a function of reflector shape. As the ellipse shape becomes steeper, the foci moves closer to the back of the reflector and the bulb clearance hole eliminates an increasing amount of the reflector's included angle. As a result, the steepest possible ellipse will yield the least losses due to the bulb clearance hole, and maximize the total reflected light. To accomplish this, a strong aspheric lens with a low F-number (0.707) was again selected to maximize its included angle. This lens determined the shape and design of the new reflector, shown in Figure 46, whose 2-D included angle of  $290^\circ$  was double that of the previous attempt.



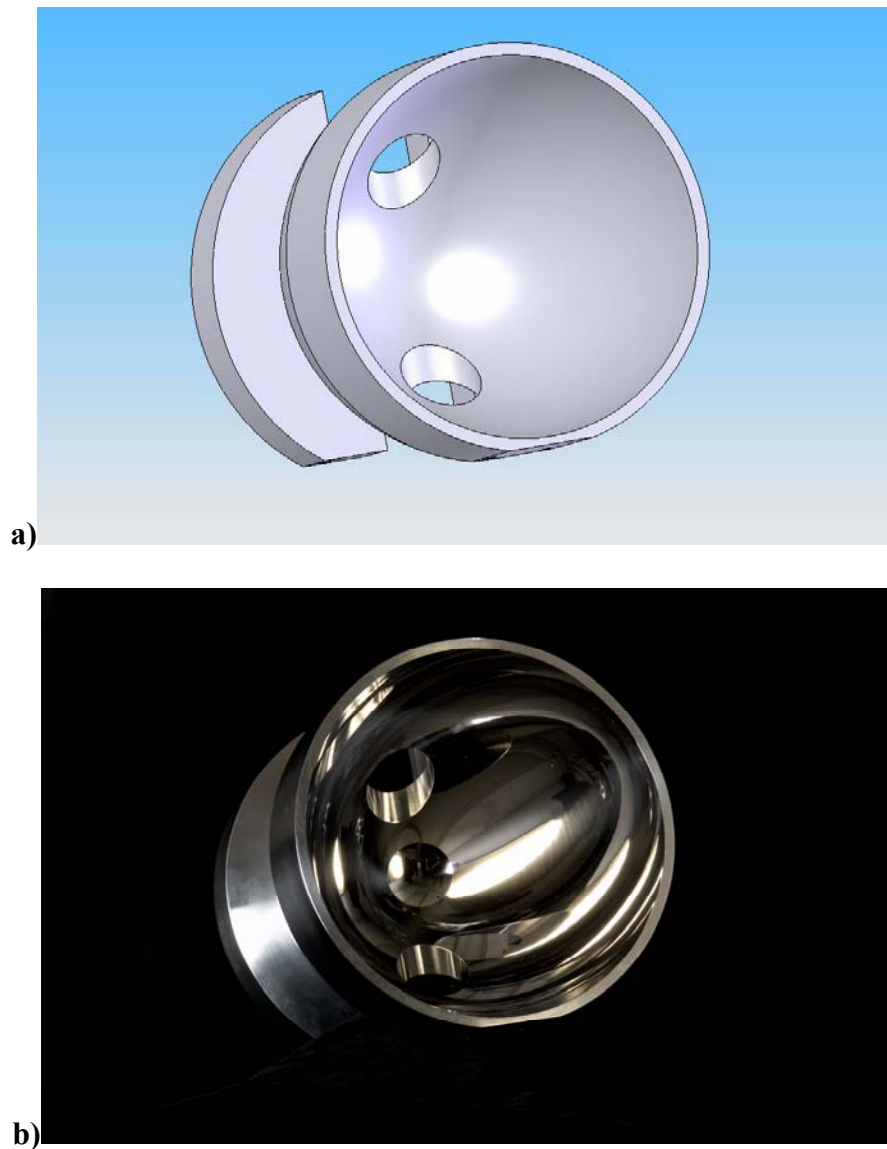


**Figure 46. Elliptical reflector a) design b) image**

This new reflector was precision fabricated out of 6061 aluminum and diamond polished to provide high reflectivity.

In addition to improving the reflector, the second effort taken to improve the performance of the system was to improve the lamp itself. By altering the current SensiFLASH 250, Cooke Corp was able to create an improved version of the lamp whose

input power is increased to 700 Joules over a 200 $\mu$ s pulse. In addition to the energy increase, the lamp is designed to ground itself 20 $\mu$ s after pulse initiation, decreasing its effective length. The result is a lamp that can place an increased amount of light in the volume of interest over only 20 $\mu$ s, thus increasing intensity and eliminating particle streaking.

### **3.5 Vortex Generator**

To provide a proof of concept for the 3-D DLCTV system, a simple and well understood flow phenomenon should be imaged so results can be easily compared to previous efforts. As a result, a hydrostatically driven heated vortex ring generator was designed and created to provide a simple way to validate both the velocity and temperature measuring capabilities of the camera system. This generator consists of a large reservoir placed above the test section that runs water through a solenoid valve to an output tube placed above of the volume of interest. This output tube contains an injection hole through which hot water can be added and is placed below a plastic piston that pushes water uniformly down the tube, creating the heated vortex ring. Figure 47 displays an image of this generator.



**Figure 47. Vortex generator**

### **3.6 Image Processing**

Processing of all images in this experiment is accomplished using a digital data acquisition system made by IO Industries. This system utilizes three DVR Express frame grabber boards, each capturing the output images of two of the system's six CCD cameras. Images recorded by the frame grabbers are then processed and visualized using IO's Streams 5 software. LUT references used previously result directly from the image enhancement ability of the Streams 5 software.

Images captured by this system are then output in bitmap format and analyzed using in-house DLCTV software based on the method used by Pereira and Gharib (2002). This software analyzes an image by first searching for particles. It accomplishes this by comparing image data with a theoretical "perfect particle." Parts of the image that sufficiently match this example particle are then selected as potential particles and their coordinates are recorded. After finding all potentials in an image, the software then looks

for the triangular triplets that indicate a true particle in the volume of interest. It does this by moving horizontally along the image from each potential particle until another particle is found. Based on that distance the software searches for a third particle in what would be the third vertex of the triangle. Upon finding each triplet, the fourth particle at the center of the triangle is located and its hue value extracted. Particle positions can then be compared between two separate images using in-house cross-correlation software, and temperatures determined based on temperature calibration data.

### **3.7 Optical Calibration**

Although precise fabrication and careful arrangement and assembly of all pieces of the camera system yield a result that is physically close to the spreadsheet camera design, an optical calibration is still required to ensure that, with a high degree of accuracy, each part of the optical system is correctly oriented. Indeed, this is perhaps the most important aspect of the 3-D DLCTV setup, as even small errors in the positioning of each component can create non-trivial error in the system as well as incorrect identification of LC particles, both of which can render any result quantitatively meaningless.

#### **3.7.1 Laser Calibration Attempt**

An initial attempt at optical calibration used a laser method to align the lens holder to the color CCD assembly. This method was seen as a first step, whose goal was to fix the center lens perpendicular to the color CCD and aligned on the optical axis. The

physical arrangement for this method can be seen in Figure 48, with a laser mounted on one of the 6 DOF translation stages and pointed directly at the camera system.

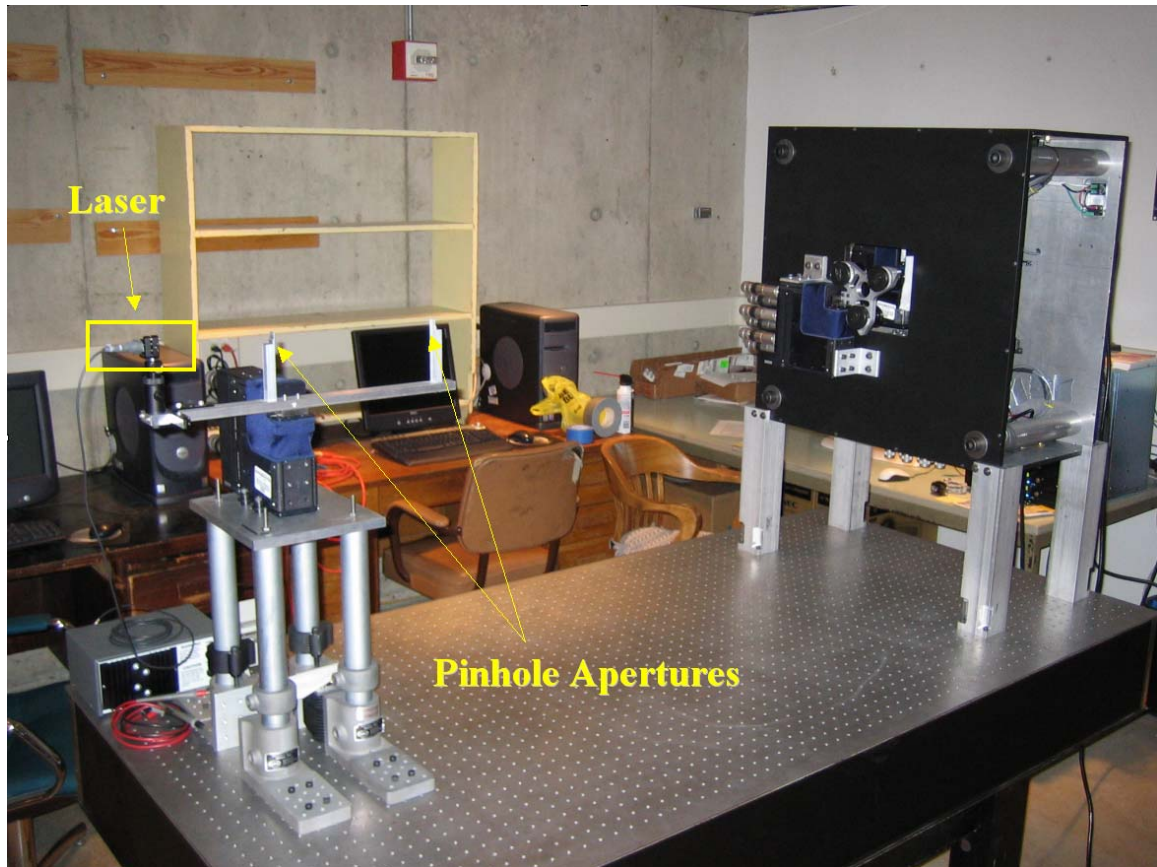


**Figure 48. Initial laser alignment setup**

In this image, the laser was also passed through two pinhole apertures to ensure a straight beam, which had the added effect of decreasing the size of the spot on the CCD. Using this arrangement, initial calibration consisted of a two-part process. First, the lens was removed and the laser fired at the CCD. The translation stage holding the laser was then rotated until the beam hit the center of the CCD and remained there as the laser was translated forward in the Z-direction. This indicated that the laser and the CCD were

correctly aligned, as any misalignment was visible through a shift in the laser spot location on the CCD. Next, the lens was replaced and the procedure repeated with the only difference being the translation stage holding the lenses was moved until the laser spot was centered and did not move with Z-translation of the lens. Once this was accomplished the lens was, in theory, correctly aligned with the CCD.

Although sound in principal, this method failed to converge to the correct alignment of the optical system. Its failure was primarily due to the fact that the stage's axes are independent of one another. In essence, if the stage was level and then rotated about the X-axis such that the laser was pointed slightly towards the floor, translation in the Z-axis would result in movement that was perfectly parallel to the floor rather than in that slightly downward direction. This independence means that the movement in the Z-direction in both parts of this calibration method cannot result in the laser spot being stationary on the center of the CCD unless the Z-axis motion of the stage itself is already perfectly perpendicular to the camera. Without rigorous adjustment this is impossible, and due to the size and weight of the translation stages, stacking several stages on top of one another could not be accomplished. As a result, this method was slightly modified and a second calibration method attempted.

Also involving lasers, this method instead used a laser grid for calibration rather than a simple spot. To better facilitate calibration, this grid consisted of a 4 x 4 array of squares seen in Figure 49.

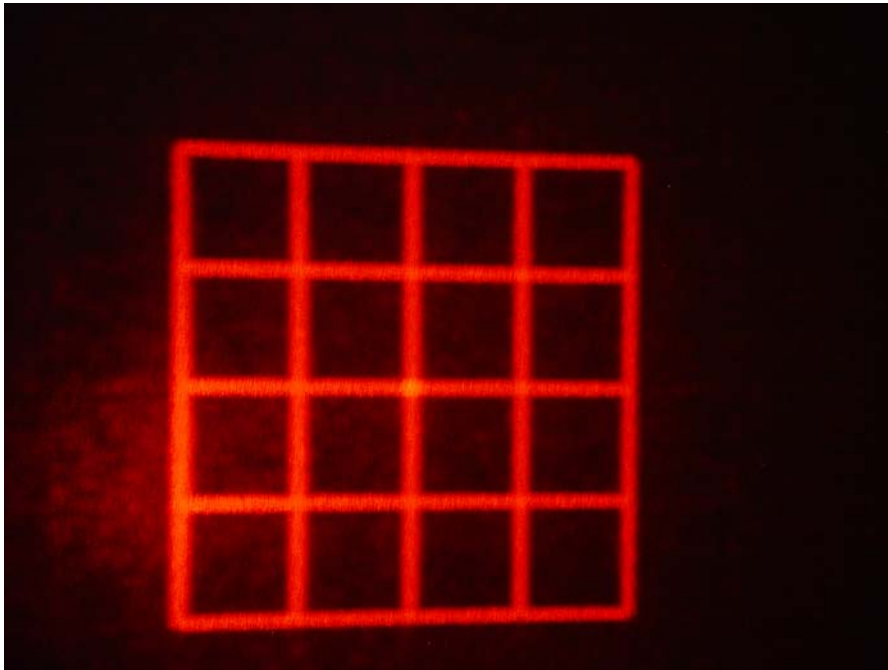


**Figure 49. 4 x 4 square laser grid**

With this grid, the center of the pattern was readily identifiable as an intersection and any distortion could be easily seen as a skewing of the square in one direction or another. As a result, the laser could be placed directly in front of the lenses and fired at the CCD for calibration without requiring Z-axis translation. Thus, the same method described previously could be used for the laser grid. The lens was first removed and the laser rotated and translated until the grid was centered on the CCD and distortion free. Once this was accomplished, the lens could be replaced and the same procedure repeated, this time moving the lenses.

Although simple in theory, analysis of the grid proved difficult due to the resolution of the laser. Although the grid appeared continuous in Figure 49, upon closer

inspection using the CCDs it actually consists of a series of dots, as seen in Figure 50 below. It should be noted that this image has been inverted for printing purposes only.

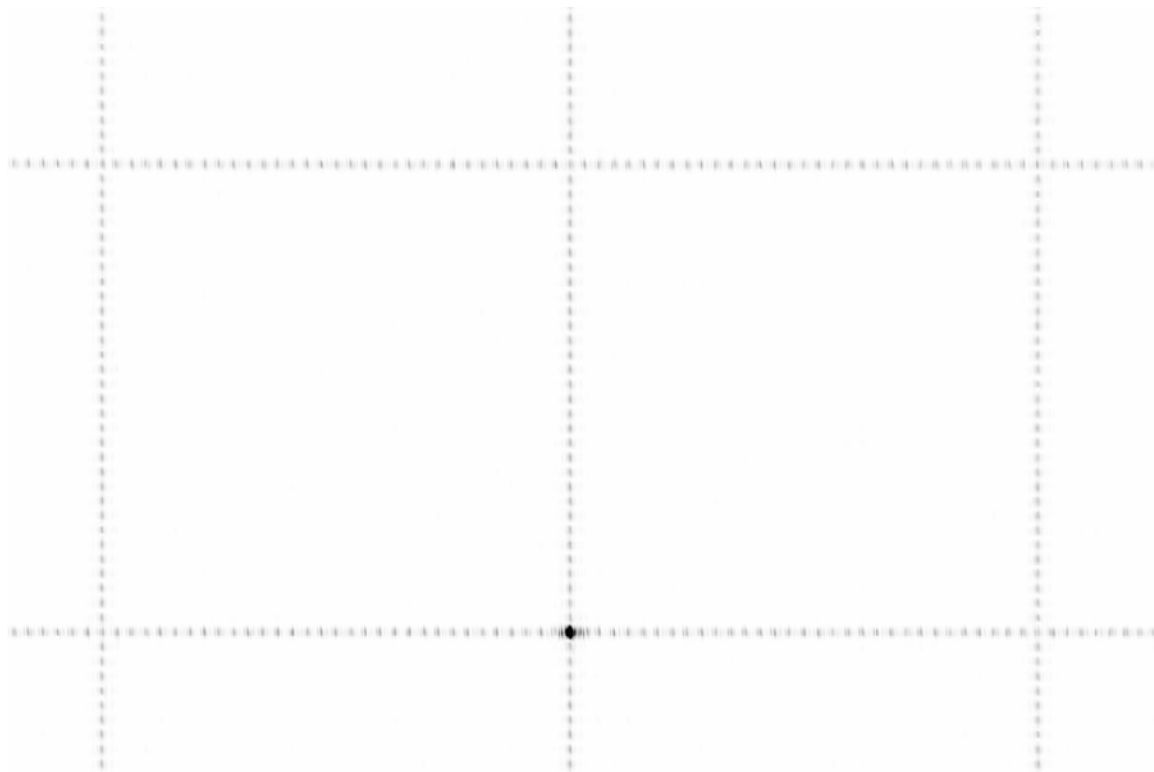


**Figure 50. Image of laser grid as seen on CCD**

To analyze this discontinuous image, in-house software was created to quantitatively identify the center of the grid and measure distortion. This software consisted of a series of Gaussian fits applied to approximately 10 dots on each side of the rectangular portion of the grid visible on the CCD. The location of the center of each dot on all four sides was calculated by performing two Gaussian fits across it at the dot's local maximum, one in  $x$  and one in  $y$ . This information was then extracted for each dot and used to fit a continuous line through the dots on each side. By fitting a line to each side, a continuous



rectangle was artificially created that very closely approximates the shape of the rectangular grid seen in the image above. The coordinates of the corners of this artificial rectangle were then calculated as the intersection of the fit lines of any two sides. Using these coordinates, the center of the grid was calculated along with the differences in the horizontal and vertical coordinates of each corner. These differences are representative of distortion present in the beam that must be calibrated out. For example, the top two corners of the grid should have the same vertical coordinate in an undistorted image.

Despite the rigorous analysis used in this process, it failed to properly calibrate the camera system for several reasons. The first reason was the focus of the grid. Although the focus of the laser grid could be adjusted, a focused grid fired at the CCD without its corresponding lens will not be focused when the lens is replaced. The opposite was also true. Refocusing the grid for each case would result in slight movement of the laser and invalidation of any calibration performed up to that point. As a result, the laser was slightly defocused when imaged without the camera lens such that when the lens was replaced the grid was similarly defocused. However, in this defocused position the laser dots widened and in some cases split into several different dots as can be seen in Figure 51. Again, note that this image has been inverted for printing purposes.



**Figure 51. Laser grid showing defocused dot splitting**

This fact greatly increased the uncertainty in the calibration method, which is the second reason this method failed to calibrate the optical system. Because of the defocusing,

identification of each laser dot became more difficult as they became larger, more oddly shaped, and in some cases split into several different dots. This resulted in an increase in the uncertainty of the identified center of each dot found using the Gaussian fit. This error then propagated to the creation of the continuous lines that make up the box, which had error themselves. The result was occasional non-linear and unpredictable behavior in the calculated position and distortion of the grid. This behavior prevented convergence of the calibration method to an acceptable level of accuracy and prevented confidence in any particular solution. As a result, this method was also deemed unacceptable for calibration and an entirely new method was devised.

### **3.7.2 Target Calibration Method**

The common flaw with both methods discussed heretofore was that they relied on projecting an external light source onto the CCD. That projection apparatus, a laser, also had to be calibrated prior to camera calibration beginning. In contrast, the final optical calibration method involved pure imaging of a target that could be rigidly affixed to the camera system. In this manner another variable of the optical system (target/focal plane location) could be fixed prior to calibration beginning and all calibration could be accomplished with the lens in place, thereby eliminating the need for a defocused calibration.

To accomplish this calibration, a precision distortion target was designed, and custom built by Applied Image Corp. This target consisted of a square grid with dots placed at the center of each smaller square that when added together make up the whole target. In addition, for easier identification of the center of the target, a dot was placed on

top of the line intersection at the target's center. This target was then rigidly affixed to the lens holder at the proper focal distance using three precisely fabricated calibration rods. A sample of this pattern can be seen in Figure 52, while the mounting method is shown in Figure 53.

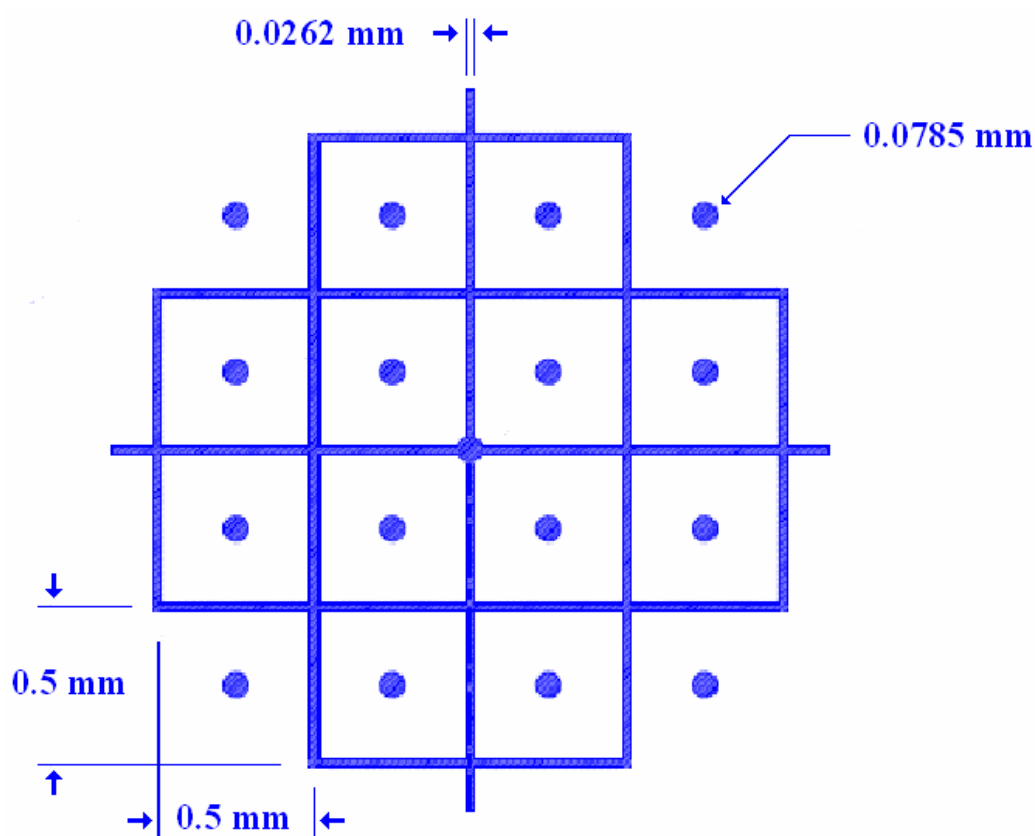
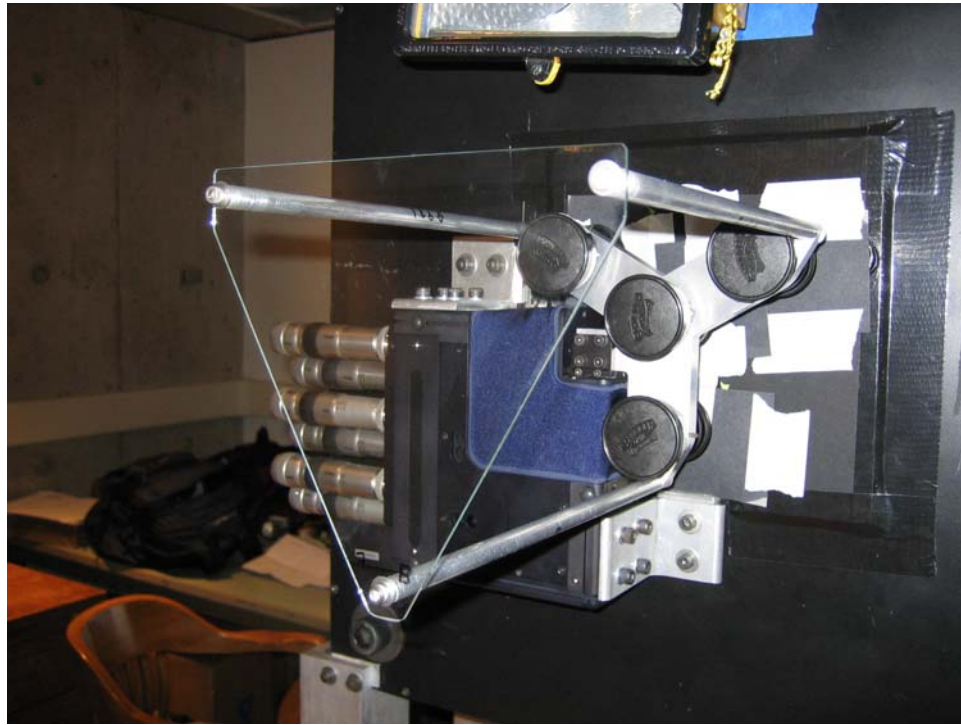


Figure 52. Distortion target grid pattern



**Figure 53. Distortion target mounting method**

The full grid measures approximately 1.5"x1.5", with a square grid spacing of 0.5262 mm  $\pm$  0.02 $\mu$ m. and is made up of 0.0262 mm  $\pm$  2 $\mu$ m thick lines (approximately 3 CCD pixels), while the dots in the grid measure 0.0785 mm  $\pm$  2 $\mu$ m in diameter (approximately 7 CCD pixels).

Calibration using this target proved far simpler than previous methods. Because the holes used to mount the target to the lens holder form an equilateral triangle centered about the center of the pattern, the center of the target pattern is by design aligned with the center of the lens, within manufacturing tolerances. As a result, if the lens holder stage can be moved such that an image of the target taken by the color CCD is distortion free and centered on the CCD, the lenses will be both arrayed about the optical axis and parallel to the sensor plane. Because of this fact, optical calibration of the lenses and

each of the three black and white CCDs involves five steps: initial alignment, focus, distortion removal, centering, and final overlay. While the following method applies to both lens and CCD calibration, it should be noted that the lens/color camera calibration was accomplished prior to any calibration of the black and white CCDs. Although the order in which the black and white CCDs are calibrated does not matter, the lens holder must be aligned first to establish the optical system.

Initial alignment is the coarsest step in the process and is accomplished without and aperture in any of the four lenses. It consists of capturing a live image with the camera being calibrated, or the color camera for the lens calibration, and adjusting the corresponding translation stage such that the target image is approximately distortion free and centered upon visual inspection of the image. This step can typically fix distortion and centering to within a few pixels, which both provides a good starting point for more rigorous removal of distortion and target centering as well as ensuring a consistently good image for the focusing step.

The focusing step was accomplished using in-house software modeled after that used in previous calibration methods. This software takes a series of eight one-dimensional Gaussian fits across the grid lines at the corners of the image. Two fits are taken at each corner, one vertically and one horizontally. The width parameters of all fits are then extracted and averaged. Because a focused image will yield the sharpest and hence smallest lines, focusing any given camera involves simply moving the stage that is holding the camera (or lens holder for the color camera) through its Z-translational range. As the stage is moved, the widths of the lines, and hence the Gaussian width parameter, will decrease and then increase as the target comes into and then drops out of focus. By

mapping this data and performing a curve fit to it, the optimal focus point for that particular camera can be found as the lowest point on that curve. A sample focus calibration curve is shown in Figure 54.

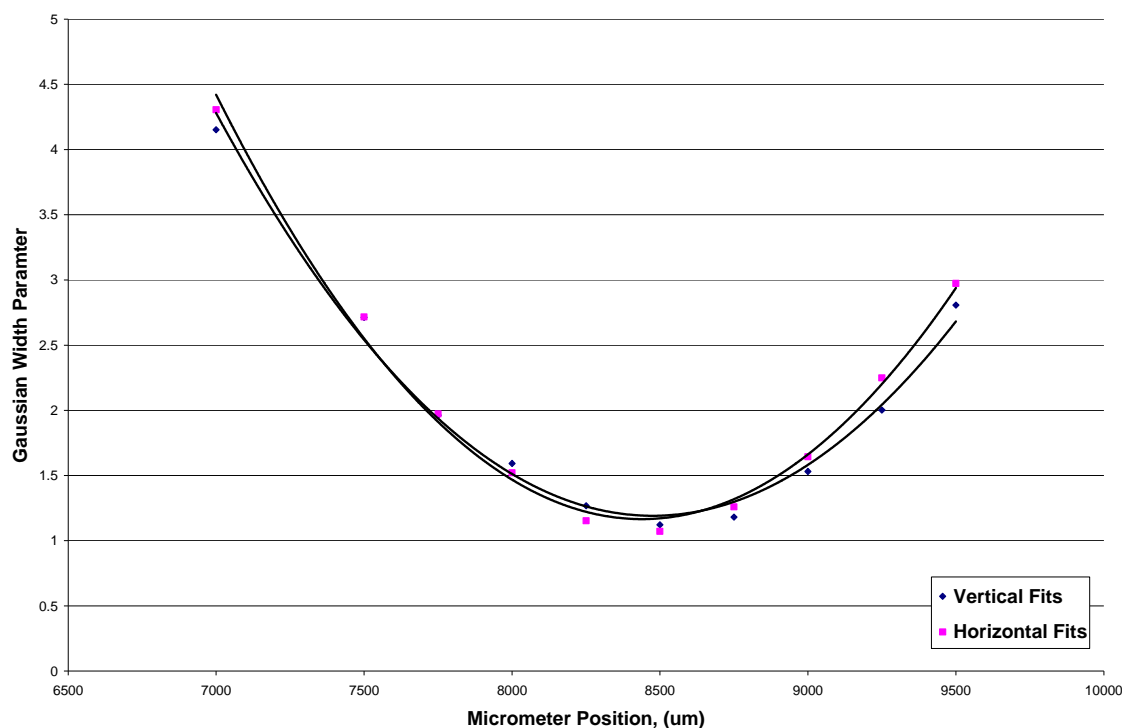


**Figure 54. Lens holder focus calibration curve**

The third step in this method is the removal of distortion. This method uses the same basic software as that for focusing, but instead of using Gaussian width, it calculates the center of the fits. It then uses that information from each of the eight fits to calculate the degree to which each of the four lines that make up the largest square visible on the image deviate from being purely vertical or horizontal. This method closely resembles that used for the laser grid; however a line fit does not have to be applied to

each series of Gaussian fits, as a continuous line already exists on the target grid. The final output of the software is the deviation amount, in number of pixels, of the vertical grid lines from top to bottom and of the horizontal lines from left to right. Using these values, the incorrect orientation of the component being calibrated can be inferred and proper corrective action taken. After much iteration, the average shift of any given line was removed to within  $0.3 \pm 0.036$  pixels of zero distortion for the color camera and lens combination. It should be noted that this represents a maximum of  $0.3 \pm 0.034$  pixels of deviation over 4008 pixels horizontally and  $0.3 \pm 0.042$  pixels over 2672 pixels vertically. Each black and white CCD was then calibrated such that their distortion values were within  $0.5 \pm 0.072$  pixels horizontally and  $0.5 \pm 0.084$  pixels vertically of that for the color camera. This was done to produce quality triplets when all CCD images are superimposed.

Once distortion was removed, the next step in the calibration process, centering, could occur. This step again involved the use of in-house software based on those described above. Similarly, this software uses one-dimensional Gaussian fits, however this time only four fits are used, one across each of the four lines that comprise the intersection at the center of the target pattern. By extracting the center location of each of the fits across the horizontal lines, their vertical coordinates are averaged to find the vertical position of the center. Likewise, the horizontal coordinates of the fits across the vertical lines are averaged to give the horizontal coordinates of the center. Once the center position is found, the lens stage is translated in the proper direction to image the center of the target on the center of the CCD (2004.5, 1336.5). For the lens stage, the target was centered to within  $0.3 \pm 0.018$  pixels of that value. As before, each of the

black and white CCDs were centered to within  $0.5 \pm 0.036$  pixels of the lens holder/color camera value to ensure triplet uniformity.

It should be noted that the vertical shift of all three black and white CCDs discussed in Kajitani and Dabiri (2005) would be implemented at this stage of the calibration for the black and white CCDs. This shift will increase the total amount of the volume of interest that can successfully be imaged by the camera. However, the value of this shift, shown previously as the final term of Equations 8 and 9, must first be changed to reflect the fact that the CCDs used in this effort are rectangular and not square. As a result, the camera system was sized to fill the width of the CCD (represented by the variable  $h$ ), but the shift term must now be dependant on the CCD height,  $h_v$ , as well. The resulting equation for the new shift value is shown below, and must replace the final term of Equations 8 and 9 if this shift is utilized.

$$\frac{1}{2}(h_v - \frac{h}{\sqrt{3}}) \quad (32)$$

Substitution of the dimensions of the CCDs used in this effort into the above equation yield a shift amount of 1.563mm downward. As a result, the image center should now be positioned at (2004.5, 1157.51) during the centering phase to account for this shift. In order to aid in the simplicity of this first effort, the above shift was omitted during the calibration procedure. However, future efforts can use this shift value to increase the viewing area of the camera system, thus utilizing an advantage of this three-camera arrangement over previous efforts.



Following the first four steps of the calibration method, pinholes must be placed in each of the four lenses. The 3DDLCPTV system requires the use of pinhole apertures to obtain the necessary depth of field, but the addition of the pinholes can slightly move the lens holder. As a result, centering and distortion must be checked and slightly adjusted prior to the final calibration step occurring. While this does not prove difficult, it should be noted that images taken with the pinholes are noisier than those without. This noise increases average distortion error to 0.3 pixels and average centering error to 0.09 pixels. The significantly smaller error of the centering method on these noisy images suggests that a future improvement of the calibration method could be made by utilizing the centering software to calculate distortion.

Once the first four calibration steps were accomplished for the lens holder and each of the black and white CCD stages, a final alignment check was required to ensure perfect image overlay between all four cameras. This check consisted of superimposing images taken simultaneously from each of the four cameras, and then adjusting each of the black and white CCDs until they perfectly matched the color camera. While the initial four steps in the calibration process described above were rigorous in matching the centering and distortion values of the black and white CCDs to the center camera, its accuracy in matching focus position of the black and white CCDs was not nearly as precise. As a result, a superimposed image taken after individual calibration of each camera, shown below in Figure 55, displayed a slight deviation of the black and white CCD images from the color image.

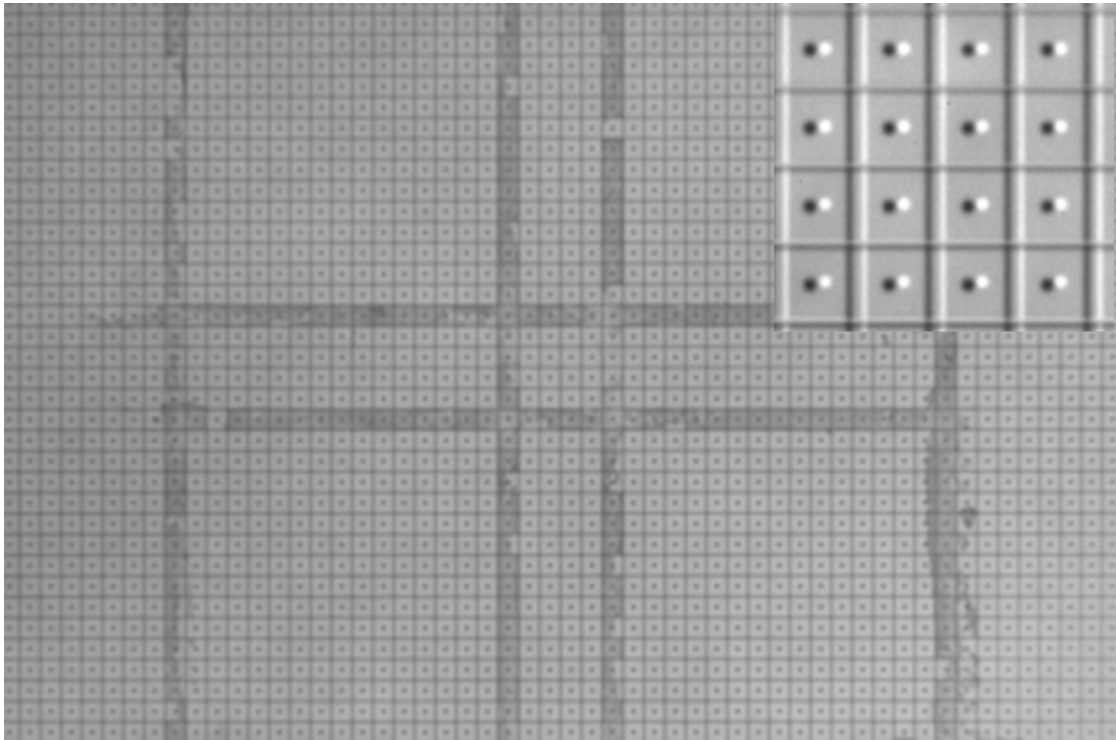


**Figure 55. Overlay of center, top left, and bottom CCDs after individual calibration**

This deviation is due to slight errors in the Z-position of the black and white CCDs in question, and as a result is non-uniform in magnitude across the image.

To correct for these errors, each deviant CCD was translated in the Z-direction until its grid image showed uniform deviation from the center camera image. This indicated a properly focused position. It was then translated in the X and Y-directions to once again obtain perfect grid overlay. Once this alignment check was completed for all three black and white cameras, an overlay of simultaneous images from each camera showed perfect grid agreement, as shown in Figure 56.

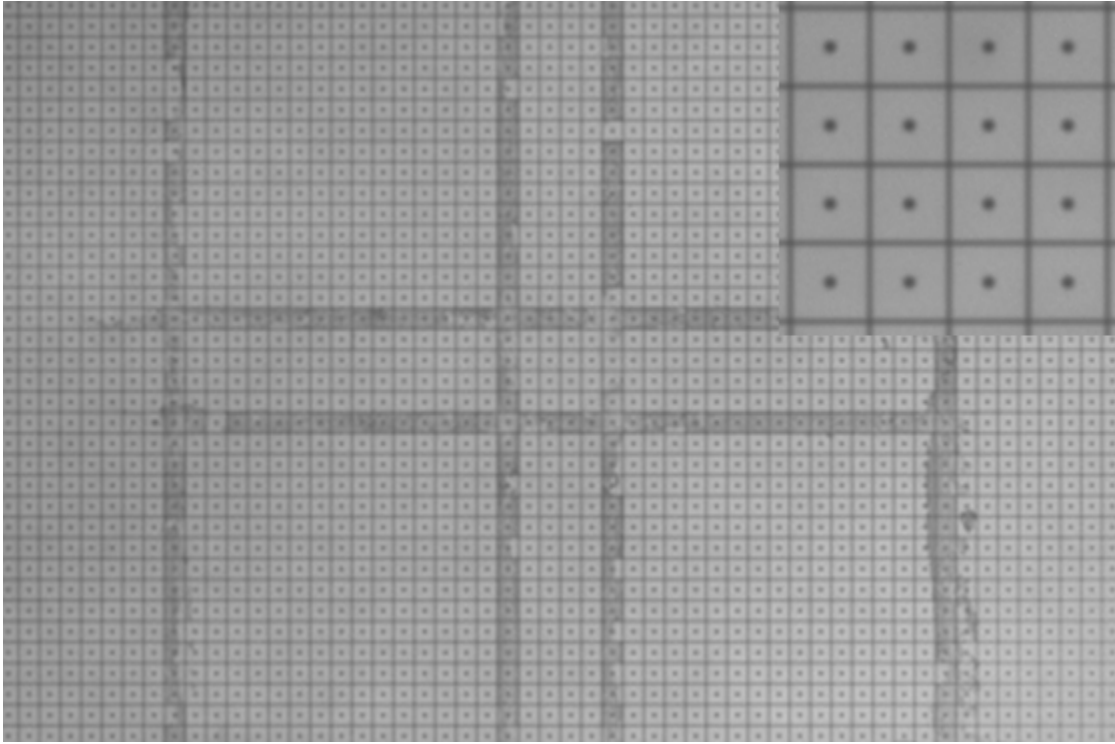


**Figure 56. Overlay of center (Green), top left (Red), and bottom (Blue) CCDs after final alignment check**

Although this final check proved all CCDs were imaging an identical area, it did not necessarily prove that each camera was in its proper position about the optical axis per the design discussed above. As a result, a defocused image of the target grid was taken to ensure triplets could be found in the superimposed image of the three black and white cameras. This was accomplished by moving the target grid away from the camera by approximately 3mm, which was within the domain of interest but on the opposite side of the focal plane as the volume of interest. Analysis of the superimposed image, Figure 57 below, reveals that perfect triplets can be identified using the dots on the target grid as makeshift “particles.” The identification of usable triplets in this image marks the

successful conclusion of the optical calibration of the 3DDLCPTV system, and validates the accuracy of the technique.

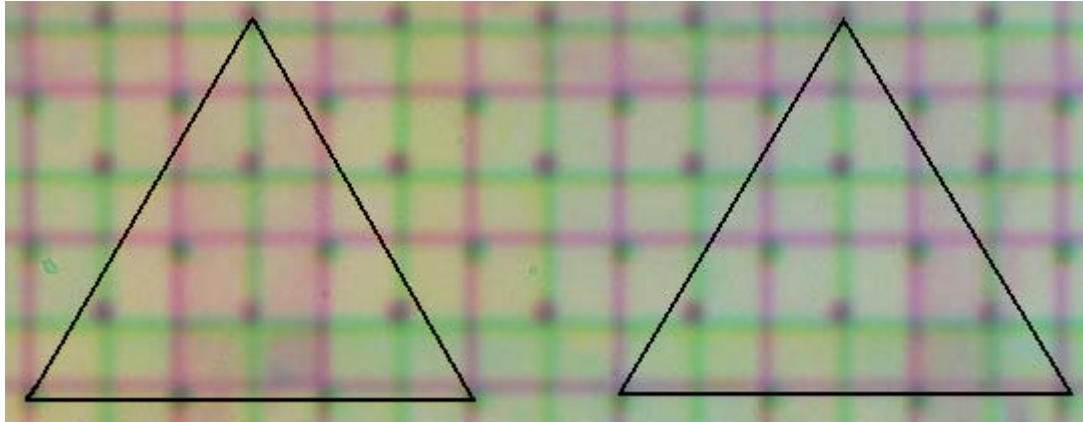


**Figure 57. Overlay of defocused images from the top right (Green), top left (Red), and bottom (Blue) CCDs showing image triplets**

### 3.8 Experimental Arrangement

The final setup for this experiment can be seen in Figure 58, and consists of the precise placement of all aforementioned components. The test tank must be placed at the proper distance from, and parallel to, the lens plane, as defined by the design spreadsheet, such that the equations which define the camera for the desired volume of interest are valid. The vortex generator is placed above the volume of interest on a moveable platform thus providing the ability to image different parts of the vortex ring. Finally, both light sources and their corresponding optics are placed on opposite sides of the test tank at  $45^\circ$  angles to the optical Z-axis, ensuring consistent lighting between consecutive flashes.

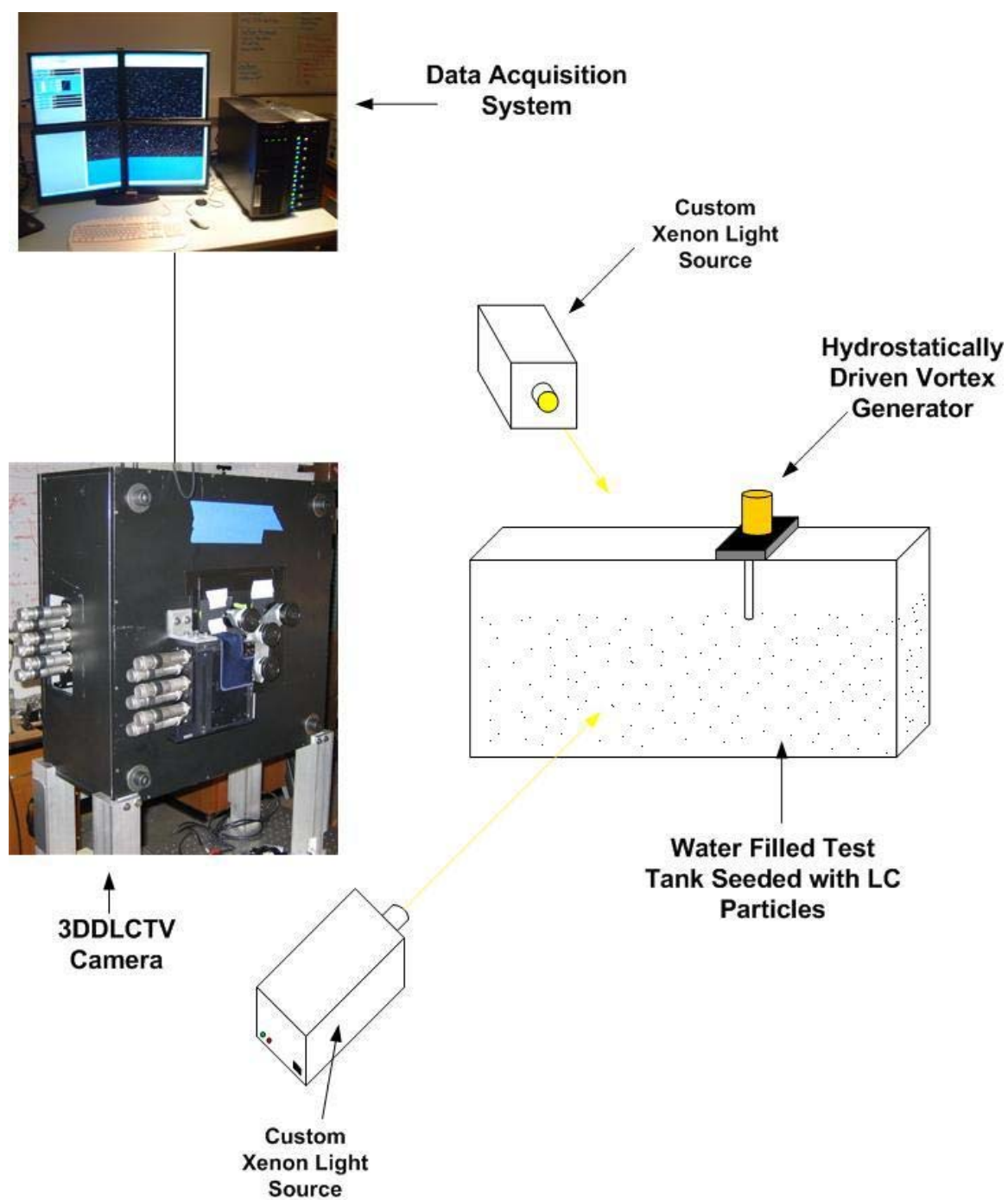


Figure 58. Experimental setup for 3DDLCPTV camera system

## 4.0 Conclusion

A fully Three Dimensional Defocusing Particle Liquid Crystal Thermometry and Velocimetry (3DDLCPV) system has been designed, fabricated, and calibrated to image a three dimensional volume of interest. This system utilizes three, eleven megapixel CCDs and a 3-CCD custom color camera assembly arranged in an equilateral triangle formation to use the theory of defocusing velocimetry to provide velocity measurements while at the same time utilizing liquid crystal thermometry to obtain temperature data. This will be accomplished by the seeding of liquid crystals in the imaging medium to provide temperature sensitive tracer particles in the flow. These particles will then be illuminated with a high intensity xenon flashlamp to provide adequate illumination for imaging. To eliminate astigmatism in the optical system brought about by necessarily large off-axis viewing angles, a water-filled prism was designed and constructed. When placed on the side of the test tank and properly aligned with the camera system, this prism effectively eliminates image astigmatism seen when imaging through water, leaving only a slight shift in the optical rays that has been accounted for through a camera redesign. To test the validity of the camera system once all components are in place, a heated vortex ring generator was constructed to provide a simple and well-understood proof of concept experiment. Optical calibration of the camera system was accomplished to sub half pixel accuracy in distortion and centering through the use of a high accuracy calibration target. After completion of this calibration, images taken of the test target when placed behind the focal plane showed identifiable image triplets, thereby confirming the validity of this calibration method. Pending the arrival of new xenon

flashlamps to provide adequate light intensity, a temperature calibration of the LC particles and testing on the heated vortex ring will occur.

## WORKS CITED

- 1) Adrian R 1996 Strategies for Imaging Flow Fields with PIV *AIAA Paper 96-1988*, 27<sup>th</sup> *AIAA Fluid Dynamics Conference*
- 2) Anderson M R and J W. Baughn 2004 Hysteresis in Liquid Crystal Thermography *J. Heat Transfer* **126** 339-346
- 3) Anderson M R and J W. Baughn 2005 Thermochromic Liquid Crystal Thermography: Illumination Spectral Effects. Part 2--Theory *J. Heat Transfer* **127** 588-597
- 4) Dabiri D and M Gharib 1996 The Effects of Forced Boundary Conditions on Flow Within a Cubic Cavity Using Digital Particle Image Thermometry and Velocimetry (DPITV) *Exp. Therm. Fluid Sci.* **13** 349-363
- 5) Dabiri D 2007 Digital Liquid Crystal Thermometry/Velocimetry (DLCT/V) - a Review." Submitted to *Exp. Fluids*
- 6) Farina D J, Ahcker J M, Moffat R J and Eaton J K 1994 Illuminant invariant calibration of thermochromic liquid crystals *Exp. Therm. Fluid Sci.* **9** 1-12
- 7) Fergason J L 1964 Liquid Crystals *Scientific American* **211** 77-85
- 8) Fergason J L 1966 Cholesteric structure – I optical properties *Molecular Crystals* **1** 293-307
- 9) Fujisawa N and S Funatani 2000 Simultaneous Measurement of Temperature and Velocity in a Turbulent Thermal Convection by the Extended Range Scanning Liquid Crystal Visualization Technique *Exp. Fluids Supp* S158-S165
- 10) Grewal G S, M Bharara, J E Cobb, V N Dubey and D J. Claremont 2006 A Novel Approach to Thermochromic Liquid Crystal Calibration Using Neural Networks *Meas. Sci. Technol.* **17** 1918-1924
- 11) Hay J L and D K Hollingsworth 1996 A Comparison of Trichromatic Systems for Use in the Calibration of Polymer-Dispersed Thermochromic Liquid Crystals *Exp. Therm. Fluid Sci.* **12** 1-12
- 12) Hay J L and D K Hollingsworth 1998 Calibration of Micro-Encapsulated Liquid Crystals Using Hue Angle and a Dimensionless Temperature *Exp. Therm. Fluid Sci.* **18** 251-257



- 13) Hollingsworth D K, Boehman A L, Smith E G and Moffat R J 1989 Measurement of temperature and heat transfer coefficient distributions in a complex flow using liquid crystal thermography and true-color image processing *Collected Papers in Heat Transfer* 35-42
- 14) Jähne B 1997 Practical Handbook on Image Processing for Scientific Applications *CRC Press*
- 15) Jeschke P, R Bierumpf and H Beer 2000 Liquid-Crystal Thermography for Heat-Transfer Measurements in the Presence of Longitudinal Vortices in a Natural Convection Flow *Meas. Sci. Technol.* **11** 447-453
- 16) Kajitani L and D Dabiri 2005 A Full Three-Dimensional Characterization of Defocusing Digital Particle Image Velocimetry *Meas. Sci. Technol.* **16** 790-804
- 17) McDonnell D.G. 1987 Thermochromic cholesteric liquid crystals. In: Gray G W (ed) *Thermotropic Liquid Crystals John Wiley & Sons* **22** 120-144
- 18) Meneveau C and J Katz 2000 Scale-Invariance and Turbulence Models for Large-Eddy Simulation *Annu. Rev. Fluid Mech.* **32** 1-32
- 19) Mitchell B S 2004 An Introduction to Materials Engineering and Science: For Chemical and Materials Engineers *John Wiley & Sons, Inc*
- 20) Murai S, Nakamura H and Suzaki Y 1980 Analytical orientation for non-metric camera in the application to terrestrial photogrammetry *Int. Arch. Photogramm.* **23** 516-25
- 21) Oseen C W 1933 The theory of liquid crystals *Trans. Faraday Soc* **29** 883-900
- 22) Park H G, D Dabiri and M Gharib 2001 Digital Particle Image Velocimetry/Thermometry and Application to the Wake of a Heated Circular Cylinder *Exp. Fluids* **30** 327-338
- 23) Park, H and Gharib, M 1999 Personal communication
- 24) Pereira F and M Gharib 2002 Defocusing Digital Particle Image Velocimetry and the Three-Dimensional Characterization of Two-Phase Flows *Meas. Sci. Technol.* **13** 683-694
- 25) Pereira F, M Gharib, D Dabiri and D Modarress 2000 Defocusing Digital Particle Image Velocimetry: a 3-Component 3-Dimensional DPIV Measurement Technique. Application to Bubbly Flows *Exp. Fluids Supp* S78-S84

- 26) Prasad A K and K Jensen 1995 Scheimpflug Stereocamera for Particle Image Velocimetry in Liquid Flows *Appl. Optics* **34** 7092-7099
- 27) Sabatino D R, T J. Praisner and C R. Smith 2000 A High-Accuracy Calibration Technique for Thermochromic Liquid Crystal Temperature Measurements *Exp. Fluids* **28** 497-505
- 28) Smith C R, D R. Sabatino and T J. Praisner 2001 Temperature Sensing with Thermochromic Liquid Crystals *Exp. Fluids* **30** 190-201
- 29) Virant M and Dracos T 1997 3D PTV and its application on Lagrangian motion *Meas. Sci. Technol.* **8** 1539-52
- 30) Westerweel J 1993 *Digital Image Velocimetry: Theory and Application* (Delft: Delft University Press)
- 31) Wiberg R and N Lior 2004 Errors in Thermochromic Liquid Crystal Thermometry *Review of Scientific Instruments* **75** 2985-2994
- 32) Willert C and Gharib M 1991 Digital particle image velocimetry *Exp. Fluids* **10** 181-3
- 33) Willert C and M Gharib 1992 Three-Dimensional Particle Imaging with a Single Camera *Exp. Fluids* **12** 353-358
- 34) Zhang, Z, and K Eisele 1995 Off-Axis Alignment of an LDA-Probe and the Effect of Astigmatism on Measurements *Exp. Fluids* **19** 89-94
- 35) Zhang J, Meng H and Hussain F 1993 Innovative holographic particle velocimeter: a multibeam technique *Opt. Lett.* **18** 1101-3

## REFERENCES

- 1) Adrian R 1996 Strategies for Imaging Flow Fields with PIV *AIAA Paper 96-1988*, 27<sup>th</sup> *AIAA Fluid Dynamics Conference*
- 2) Anderson M R and J W. Baughn 2004 Hysteresis in Liquid Crystal Thermography *J. Heat Transfer* **126** 339-346
- 3) Anderson M R and J W. Baughn 2005 Liquid-Crystal Thermography: Illumination Spectral Effects. Part 1—Experiments *J. Heat Transfer* **127** 581-587
- 4) Anderson M R and J W. Baughn 2005 Thermochromic Liquid Crystal Thermography: Illumination Spectral Effects. Part 2--Theory *J. Heat Transfer* **127** 588-597
- 5) Dabiri D and M Gharib 1996 The Effects of Forced Boundary Conditions on Flow Within a Cubic Cavity Using Digital Particle Image Thermometry and Velocimetry (DPITV) *Exp. Therm. Fluid Sci.* **13** 349-363
- 6) Dabiri D 2007 Digital Liquid Crystal Thermometry/Velocimetry (DLCT/V) - a Review." Submitted to *Exp. Fluids*
- 7) Farina D J, Ahcker J M, Moffat R J and Eaton J K 1994 Illuminant invariant calibration of thermochromic liquid crystals *Exp. Therm. Fluid Sci.* **9** 1-12
- 8) Fergason J L 1964 Liquid Crystals *Scientific American* **211** 77-85
- 9) Fergason J L 1966 Cholesteric structure – I optical properties *Molecular Crystals* **1** 293-307
- 10) Fujisawa N and S Funatani 2000 Simultaneous Measurement of Temperature and Velocity in a Turbulent Thermal Convection by the Extended Range Scanning Liquid Crystal Visualization Technique *Exp. Fluids* **Supp** S158-S165
- 11) Fujisawa N and Y Hashizume 2001 An Uncertainty Analysis of Temperature and Velocity Measured by a Liquid Crystal Visualization Technique *Meas. Sci. Technol.* **12** 1235-1242
- 12) Grewal G S, M Bharara, J E Cobb, V N Dubey and D J. Claremont 2006 A Novel Approach to Thermochromic Liquid Crystal Calibration Using Neural Networks *Meas. Sci. Technol.* **17** 1918-1924
- 13) Hay J L and D K Hollingsworth 1996 A Comparison of Trichromic Systems for Use in the Calibration of Polymer-Dispersed Thermochromic Liquid Crystals *Exp. Therm. Fluid Sci.* **12** 1-12

- 14) Hay J L and D K Hollingsworth 1998 Calibration of Micro-Encapsulated Liquid Crystals Using Hue Angle and a Dimensionless Temperature *Exp. Therm. Fluid Sci.* **18** 251-257
- 15) Hollingsworth D K, Boehman A L, Smith E G and Moffat R J 1989 Measurement of temperature and heat transfer coefficient distributions in a complex flow using liquid crystal thermography and true-color image processing *Collected Papers in Heat Transfer* 35-42
- 16) Hunt E M and M L Pantoya 2004 A Laser Induced Diagnostic Technique for Velocity Measurements Using Liquid Crystal Thermography *Int. J. Heat and Mass Transfer* **47** 4285-4292
- 17) Jähne B 1997 Practical Handbook on Image Processing for Scientific Applications *CRC Press*
- 18) Jeschke P, R Bierumpf and H Beer 2000 Liquid-Crystal Thermography for Heat-Transfer Measurements in the Presence of Longitudinal Vortices in a Natural Convection Flow *Meas. Sci. Technol.* **11** 447-453
- 19) Kajitani L and D Dabiri 2005 A Full Three-Dimensional Characterization of Defocusing Digital Particle Image Velocimetry *Meas. Sci. Technol.* **16** 790-804
- 20) Lawson N J and Wu J 1997 Three-dimensional particle image velocimetry: error analysis of stereoscopic techniques *Meas. Sci. Technol.* **8** 894-900
- 21) Lutjen P M, D Mishra and V Prasad 2001 Three-Dimensional Visualization and Measurement of Temperature Field Using Liquid Crystal Scanning Thermography *J. Heat Transfer* **123** 1006-1014
- 22) Ma X, G E Karniadakis, H Park and M Gharib 2002 DPIV/T-Driven Convective Heat Transfer Simulation *Int. J. Heat and Mass Transfer* **45** 3517-3527
- 23) McDonnell D.G. 1987 Thermochromic cholesteric liquid crystals. In: Gray G W (ed) *Thermotropic Liquid Crystals John Wiley & Sons* **22** 120-144
- 24) Meneveau C and J Katz 2000 Scale-Invariance and Turbulence Models for Large-Eddy Simulation *Annu. Rev. Fluid Mech.* **32** 1-32
- 25) Mitchell B S 2004 An Introduction to Materials Engineering and Science: For Chemical and Materials Engineers *John Wiley & Sons, Inc*
- 26) Murai S, Nakamura H and Suzuki Y 1980 Analytical orientation for non-metric camera in the application to terrestrial photogrammetry *Int. Arch. Photogramm.* **23** 516-25

- 27) Muwanga R and I Hassan 2006 Local Heat Transfer Measurements in Microchannels Using Liquid Crystal Thermography: Methodology Development and Validation *J. Heat Transfer* **128** 617-626
- 28) Oseen C W 1933 The theory of liquid crystals *Trans. Faraday Soc* **29** 883-900
- 29) Park H G, D Dabiri and M Gharib 2001 Digital Particle Image Velocimetry/Thermometry and Application to the Wake of a Heated Circular Cylinder *Exp. Fluids* **30** 327-338
- 30) Park, H and Gharib, M 1999 Personal communication
- 31) Pereira F and M Gharib 2002 Defocusing Digital Particle Image Velocimetry and the Three-Dimensional Characterization of Two-Phase Flows *Meas. Sci. Technol.* **13** 683-694
- 32) Pereira F, M Gharib, D Dabiri and D Modarress 2000 Defocusing Digital Particle Image Velocimetry: a 3-Component 3-Dimensional DPIV Measurement Technique. Application to Bubbly Flows *Exp. Fluids Supp* S78-S84
- 33) Prasad A K and K Jensen 1995 Scheimpflug Stereocamera for Particle Image Velocimetry in Liquid Flows *Appl. Optics* **34** 7092-7099
- 34) Sabatino D R, T J. Praisner and C R. Smith 2000 A High-Accuracy Calibration Technique for Thermochromic Liquid Crystal Temperature Measurements *Exp. Fluids* **28** 497-505
- 35) Smith C R, D R. Sabatino and T J. Praisner 2001 Temperature Sensing with Thermochromic Liquid Crystals *Exp. Fluids* **30** 190-201
- 36) Stasiek J A Stasiek, M Jewartowski and M W Collins 2006 Liquid Crystal Thermography and True-Colour Digital Image Processing *Optics & Laser Technology* **38** 243-256
- 37) Virant M and Dracos T 1997 3D PTV and its application on Lagrangian motion *Meas. Sci. Technol.* **8** 1539-52
- 38) Walree P V Jan. 2007 Astigmatism and Field Curvature *Vanwalree.Com* **21. Autumn 2006** <http://www.vanwalree.com/optics/astigmatism.html>
- 39) Westerweel J 1993 *Digital Image Velocimetry: Theory and Application* (Delft: Delft University Press)

- 40) Wiberg R and N Lior 2004 Errors in Thermochromic Liquid Crystal Thermometry  
*Review of Scientific Instruments* **75** 2985-2994
- 41) Willert C and Gharib M 1991 Digital particle image velocimetry *Exp. Fluids* **10** 181-3
- 42) Willert C and M Gharib 1992 Three-Dimensional Particle Imaging with a Single Camera *Exp. Fluids* **12** 353-358
- 43) Zhang, Z, and K Eisele 1995 Off-Axis Alignment of an LDA-Probe and the Effect of Astigmatism on Measurements *Exp. Fluids* **19** 89-94
- 44) Zhang J, Meng H and Hussain F 1993 Innovative holographic particle velocimeter: a multibeam technique *Opt. Lett.* **18** 1101-3

## APPENDIX A: CAMERA SPREADSHEETS

### Initial Design

# 3D Camera Design

## Definition of Color Code

Fixed Input	parameter
Variable Input	parameter
Secondary Result	parameter
Main Result	parameter

## CALCULATIONS

number of pixels		npix=	4008.000000
size of pixel	mm	pix=	0.008733
sensor height (mm)	mm	hp=	35.000000
wall thickness	mm	w=	7.925000
distance wall-front of domain	mm	dwd=	152.4
distance camera-wall	mm	dcw=	70

refractive index of air		ria=	1.000000
refractive index of glass		rip=	1.512000
refractive index of water		riw=	1.333333

in-plane tolerance	pixel	kx=	0.010000
out-of-plane tolerance	% of FS	kz=	0.001000
in-plane tolerance	mm	rx=	0.000065
out-of-plane tolerance	mm	rz=	0.000010

side of observation domain--front face	mm	apf=	15.138065
side of observation domain--back face	mm	apb=	25.73
depth of observation domain	mm	az=	19
focal length	mm	f=	119.900000

size observed on focal plane	mm	H=	26.035045
magnification		m=	1.344342

Connecting distance between lenses	mm	d=	90.525646
Connecting distance between CCDs	mm	d'=	212.223059
distance from origin out to each CCD	mm	$\gamma_d$ =	122.527040
altitude (X) (Top cam to base cams)	mm	Xd=	78.397509
distance from origin out to each lens	mm	$\gamma$ =	52.265006

image focal distance	mm	<b><math>L_p =</math></b>	<b>281.086585</b>
----------------------	----	---------------------------	-------------------

apparent Z min	mm	<b><math>Z_{min} =</math></b>	<b>162.386502</b>
true Z min	mm	<b><math>Z_{tmin} =</math></b>	<b>194.118438</b>
apparent distance camera-front of domain	mm	<b><math>Z_a =</math></b>	<b>189.541431</b>
optimal object apparent focal distance	mm	<b><math>L =</math></b>	<b>209.088626</b>
true distance camera-front of domain	mm	<b><math>Z_t =</math></b>	<b>230.325000</b>
object true focal distance	mm	<b><math>L_t =</math></b>	<b>256.387920</b>

Gain	$\text{mm}^{-2}$	<b><math>K =</math></b>	<b>0.000039</b>
------	------------------	-------------------------	-----------------

Apparent Z intermediate (mm)	Apparent size at intermediate range (mm)	Apparent db/dZ at intermediate range (-)	b/h
209.0886257	26.03504494	-0.58203746	0
197.4130949	19.52628371	-0.6529198	0.205643023
185.7375641	13.01752247	-0.737585316	0.437139636
174.0620333	6.508761235	-0.839853717	0.699692371
162.3865024	0	-0.964965746	1
189.5414307	15.138065	-0.708277498	0.358586218
199.0414307	20.4340325	-0.642280569	0.175515166
208.5414307	25.73	-0.585095901	0.009123534

True Z intermediate (mm)	True size at intermediate range (mm)	Apparent db/dZ at intermediate range (-)	b/h
256.3879202	52.40299507	-0.387094174	0
232.8875657	39.3022463	-0.469158026	0.350866103
209.3872113	26.20149754	-0.580378676	0.780490385
185.8868569	13.10074877	-0.736401026	1.318743358
194.118438	17.68961049	-0.675271121	1.115377213

front gap (mm)	mm	20.36620128
back gap (mm)	mm	0.547195001
effective distance to front of domain (mm)	mm	189.5414307
relative difference with the target distance (% of az)	% of az	0
b at mid domain (% of sensor)	% of sensor	17.55%
db/dZ at mid domain	--	-0.642280569
b/h at the greater of the two faces	--	0.358586218

Should be around 12-19%

off-axis distance (dp)	mm	60.84870633
diameter sensors (d')	mm	212.223059
angle (o)	deg	14.03439937

$(d-d')/2$

Needs to be below 8



degrees

## Re-Design

## 3D Camera Design

## Definition of Color Code

Fixed Input	parameter
Variable Input	parameter
Secondary Result	parameter
Main Result	parameter

**FOR PRISM  
CASE**

## CALCULATIONS

number of pixels		npix=	4008.000000
size of pixel	mm	pix=	0.008733
sensor height (mm)	mm	hp=	35.000000
wall thickness	mm	w=	7.925000
distance wall-front of domain	mm	dwd=	165.775
distance camera-wall	mm	dcw=	63

refractive index of air		ria=	1.000000
refractive index of glass		rip=	1.490000
refractive index of water		riw=	1.333333

in-plane tolerance	pixel	kx=	0.010000
out-of-plane tolerance	% of FS	kz=	0.001000
in-plane tolerance	mm	rx=	0.000102
out-of-plane tolerance	mm	rz=	0.000010

side of observation domain--front face	mm	apf=	26.4
side of observation domain--back face	mm	apb=	35.6
depth of observation domain	mm	az=	15.2
focal length	mm	f=	119.900000

size observed on focal plane	mm	H=	40.793731
magnification		m=	0.857975

Connecting distance between lenses	mm	$d=$	<b>116.361436</b>
Connecting distance between CCDs	mm	$d'=$	<b>216.196635</b>
distance from origin out to each CCD	mm	$\gamma_d=$	<b>124.821186</b>
altitude (X) (Top cam to base cams)	mm	$X_d=$	<b>100.771960</b>
distance from origin out to each lens	mm	$\gamma=$	<b>67.181307</b>

image focal distance	mm	$L_p=$	<b>222.771198</b>
----------------------	----	--------	-------------------

apparent Z min	mm	$Z_{min}=$	<b>192.249330</b>
true Z min	mm	$Z_{tmin}=$	<b>193.082609</b>
apparent distance camera-front of domain	mm	$L_a=$	<b>235.866721</b>
optimal object apparent focal distance	mm	$L_{opt}=$	<b>259.647668</b>
true distance camera-front of domain	mm	$L_t=$	<b>236.700000</b>
object true focal distance	mm	$L_{fa}=$	<b>260.480947</b>

Gain	$\text{mm}^{-2}$	$K=$	<b>0.000039</b>
------	------------------	------	-----------------

Apparent Z intermediate (mm)	Apparent size at intermediate range (mm)	Apparent db/dZ at intermediate range (-)	b/h
259.6476678	40.79373109	-0.384502583	0
242.7980833	30.59529832	-0.439721404	0.197951861
225.9484987	20.39686554	-0.507749137	0.425427322
209.0989141	10.19843277	-0.59287694	0.689563587
192.2493295	0	-0.701355886	1
235.8667208	26.4	-0.465945128	0.287592874
243.4667208	31	-0.437309489	0.189574524
251.0667208	35.6	-0.411234756	0.097490369

True Z intermediate (mm)	True size at intermediate range (mm)	Apparent db/dZ at intermediate range (-)	b/h
260.480947	41.29808427	-0.382046468	0
243.4230426	30.97356321	-0.437466438	0.199884737
226.3651383	20.64904214	-0.505881767	0.429894385
209.3072339	10.32452107	-0.591697367	0.697394208
193.0826087	0.504353187	-0.695315319	0.995684339

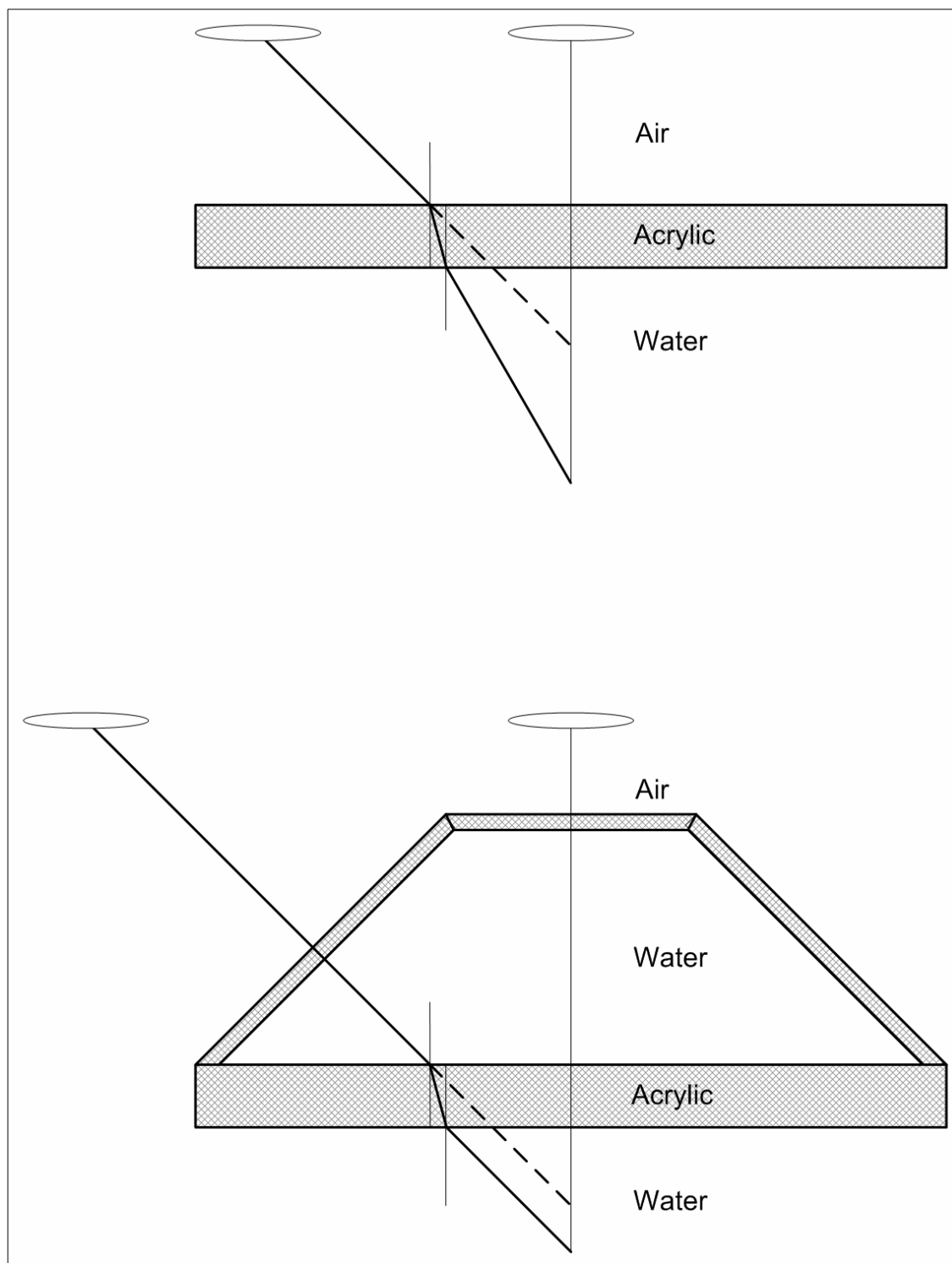
front gap (mm)	mm	32.71305166
back gap (mm)	mm	8.580947014
effective distance to front of domain (mm)	mm	235.8667208
relative difference with the target distance (% of az)	% of az	0
b at mid domain (% of sensor)	% of sensor	18.96%
db/dZ at mid domain	--	-0.437309489
b/h at the greater of the two faces	--	0.287592874

Should be around 12-19%

off-axis distance (dp)	mm	49.91759944	$(d-d')/2$
------------------------	----	-------------	------------

diameter sensors (d')	mm	216.196635
angle (o)	deg	14.50658827

Needs to be below 8  
degrees

**APPENDIX B: WATER-FILLED PRISM OPTICAL DERIVATION****Optical layout without (top) and with (bottom) prism**



**True Focal Length ( $L_t$ ):**

$$L_t = L + \Delta d_{wf}$$

$$\tan \theta_1 = \frac{x_2}{d'_{wf} + \Delta d_{wf}} \Rightarrow \Delta d_{wf} = \frac{x_2}{\tan \theta_1} - d'_{wf}$$

$$x_2 - x_1 = [\tan \theta_1 - \tan \theta_2] t_w \Rightarrow x_2 = [\tan \theta_1 - \tan \theta_2] t_w + x_1$$

$$\Delta d_{wf} = \frac{x_2}{\tan \theta_1} - d'_{wf} = \left[ 1 - \frac{\tan \theta_2}{\tan \theta_1} \right] t_w + \frac{x_1}{\tan \theta_1} - d'_{wf}$$

$$\text{Since } \tan \theta_1 = \frac{x_1}{d'_{wf}} \Rightarrow \frac{x_1}{\tan \theta_1} = d'_{wf}$$

$$\Delta d_{wf} = \left[ 1 - \frac{\tan \theta_2}{\tan \theta_1} \right] t_w$$

$$\text{From Snell's Law: } \tau_{water} \sin \theta_1 = \tau_{acrylic} \sin \theta_2$$

$$\frac{\tan \theta_2}{\tan \theta_1} = \frac{\sin \theta_2}{\cos \theta_2} \frac{\cos \theta_1}{\sin \theta_1} = \frac{\tau_w}{\tau_a} \frac{\cos \theta_1}{\cos \theta_2}$$

$$L_t = L + \left( 1 - \frac{\tau_w}{\tau_a} \frac{\cos \theta_1}{\cos \theta_2} \right) t_w \quad \text{Assuming } \frac{\cos \theta_1}{\cos \theta_2} = 1$$

$$\boxed{L_t = L + \left( 1 - \frac{\tau_w}{\tau_a} \right) t_w}$$

$$\text{Note: } \tau_{acrylic} \approx \tau_{glass}$$

**Apparent Location, Front of Domain (apf) ( $Z_a$ ):**

$$Z_a = d_{cw} + d'_{wd} + t_w$$

$$d'_{wd} = \frac{x_1 - x_{apf}}{\tan \theta_1} = \frac{x_1 - (L_t - Z_t) * \tan \theta_1}{\tan \theta_1} = \frac{x_1}{\tan \theta_1} - L_t + Z_t$$

Expanding for  $L_t$  (from above) and using the definition of  $Z_t$ :  $Z_t = d_{cw} + t_w + d_{wd}$

$$d'_{wd} = \frac{x_1}{\tan \theta_1} - L - \left( 1 - \frac{\tau_w}{\tau_a} \frac{\cos \theta_1}{\cos \theta_2} \right) * t_w + d_{cw} + t_w + d_{wd}$$

$$\text{Since } L = \frac{x_1}{\tan \theta_1} + d_{cw} + t_w$$

$$d'_{wd} = d_{wd} - \left( 1 - \frac{\tau_w}{\tau_a} \frac{\cos \theta_1}{\cos \theta_2} \right) * t_w$$

Substitution into the definition for  $Z_a$  from above:

$$Z_a = d_{cw} + d_{wd} - \left( 1 - \frac{\tau_w}{\tau_a} \frac{\cos \theta_1}{\cos \theta_2} \right) * t_w + t_w \text{ and simplifying...}$$

$$Z_a = d_{cw} + d_{wd} + \left( \frac{\tau_w}{\tau_a} \frac{\cos \theta_1}{\cos \theta_2} \right) * t_w \text{ Assuming } \frac{\cos \theta_1}{\cos \theta_2} = 1$$

$$\boxed{Z_a = d_{cw} + d_{wd} + \frac{\tau_w}{\tau_a} * t_w}$$

**True location, start of observable domain ( $Z_{t\min}$ ):**

$$X_{az\min} = (L - Z_{\min}) * \tan \theta_1$$

$$X_{tz\min} = (L_t - Z_{t\min}) * \tan \theta_1$$

Due to the definition of the volume of interest both apb and apf do not change between the apparent and true cases. Because the angle that defines the volume of interest is also the same for both cases, the x-distances defined above must be equal. Equating the two:

$$(L - Z_{\min}) * \tan \theta_1 = (L_t - Z_{t\min}) * \tan \theta_1 \quad \text{Simplifying and rearranging}$$

$$Z_{t\min} = L_t - L + Z_{\min}$$

$$\text{From above: } (L_t - L) = \left(1 - \frac{\tau_w \cos \theta_1}{\tau_a \cos \theta_2}\right) * t_w$$

Substituting:

$$Z_{t\min} = \left(1 - \frac{\tau_w \cos \theta_1}{\tau_a \cos \theta_2}\right) * t_w + Z_{\min} \quad \text{Assuming } \frac{\cos \theta_1}{\cos \theta_2} = 1$$

$$\boxed{Z_{t\min} = Z_{\min} + \left(1 - \frac{\tau_w}{\tau_a}\right) * t_w}$$